Synthesis and characterization of titanium carbon nitride films by High Power Impulse Magnetron Sputtering

Relatore: Dott. Marco Bazzan

Correlatore: Dott. Alessandro Patelli

Laureanda: Silvia Grigoletto

To my grandmothers Antonietta and Amelia.

CONTENTS

INTRODUCTION

The thin film technology is nowadays more and more widely adopted in all industrial fields due to the possibility of improving functionalities and performances on a wide range of substrates, materials and shapes in few nano or micrometers just by combining a careful *microstructural and compositional design* with *advanced deposition techniques*.

The use of thin film technologies not only reduce significantly the cost of production, improve performance or lifetime of most industrial devices but, at the same time, they allow the creation of new devices and technologies. They are now employed in all industrial fields: from photovoltaic cells to electronic and optoelectronic devices, from biomedical applications to external decoration, from lighting to hard protective coating for both industry and aerospace devices, from textiles to glass windows or lenses.

Some industrial fields that implemented the use of coating since the first '80 are the automotive and mechatronic industries. Their use in these fields has focused in corrosion protection, in the increase in surface hardness and adhesive and abrasive wear protection and in lubrication for better chip sliding, minor cutting forces and prevention from heating.

In these application fields, titanium nitrides (TiN) and carbides (TiC) are the most widely used to improve the tribological properties due to their high hardness and excellent wear resistance, the first are preferred where hardness and wear resistance are needed, the latter where lubrication is more important.

In order to improve their properties and allow the choice of the best *microstructural and compositional design* depending on the application, in the past decades, a solid solution between TiC and TiN, namely *TiCN,* has been developed. The TiCN has been discovered to show superior mechanical resistance and thermal stability. Titanium carbon nitrides coatings are formed by a prefect mixing of C and N in an fcc structure, and seem to possess the best properties of the two parent components, such as ductility of TiC and adhesion strength of TiN.

Moreover, the possibility to change the coating architecture, by altering its structure and composition in a controlled manner, enables the optimization of TiCN for tribological applications: in particular, several configurations are available, such as monolayer, multilayer or also graded structure.

The tribological behavior of TiCN has been found to depend upon the substrate, deposition method, thickness of the film and structure features [1]. It is therefore of great technological importance the development of efficient methods to produce titanium carbonitride coatings in real industrial conditions.

Physical Vapor Deposition (PVD) processes are often employed in this context. Among all deposition procedures, Direct Current Magnetron Sputtering (DCMS) employed either in a reactive or non-reactive ambient, is the most adopted for the fabrication of superhard and tough nanocomposite coatings under industrial condition, i.e. with no substrate heating and in high vacuum conditions. Nevertheless, in magnetron sputtering processes the degree of ionization of plasma particle is relatively low resulting in a low total ion flux towards the growing film, even if particular magnetron configuration are adopted in order to enhance ion bombardment to the substrate (e.g. the Closed Field Unbalanced Magnetron Sputtering – CFUBMS configuration).

An *advanced* yet recent development of DCMS *technique* is High Power Impulse Magnetron Sputtering (HiPIMS, or alternatively HPPMS), in which short, energetic pulses are applied to the target, leading to a formation of an ultra-dense plasma in front of the cathode, that provide a high degree of ionization of sputtered material, and consequently enable to control the energy and the

direction of the deposition flux. These characteristics make possible the deposition of dense and smooth coatings also on complex-shaped substrates. Moreover, new parameters are provided to control the deposition process, such as pulse time, repetition frequency, power supplied, etc., thus opening new way for microstructural design and mechanical properties tailoring [2]. To the best of our knowledge, this technique was never applied for the production of TiCN films.

The aim of this study, performed at Veneto Nanotech Labs in collaboration with the Department of Physics and Astronomy of the University of Padova, is to investigate the potentiality of an HiIPIMS reactive process with two gases as a possible technique for the production of TiCN coatings with advanced mechanical and tribological characteristics in industrial conditions with no sample biasing at room temperature. As thoroughly explained in the text, understanding the link between the deposition conditions and the microscopic structure of the deposited films is the key to define the best process conditions to realize coatings with tailored properties. For this reason, a number of different deposition conditions were explored and all the produced samples were characterized from the compositional, structural and mechanical point of view by combining a number of advanced micro − analytical techniques.

In the first chapter of this thesis we will briefly summarize the principal features of plasma deposition process trough sputtering technique, comparing DCMS with HiPIMS. Moreover, we will focus on the modeling of the sputtering process with one or more reactive gases, which will be of great importance for the comprehension of the deposition parameters influencing TiCN coatings.

In chapter two we will summarize the state of the art of TiCN thin film deposited by DCMS. This will be a starting point for the successive discussion of experimental results.

From chapter three to chapter five we will describe the experimental details, the deposition procedure optimization and the analysis carried over TiCN samples. These coatings have been morphologically characterized trough cross sectional SEM, while a detailed microstructural analysis has been performed by X-ray diffraction and micro-Raman spectrometry. The compositional analysis has been performed by Energy Dispersive X-rays Emission (EDS), Electron Probe Micro Analysis (EPMA) and Secondary Ion Mass Spectrometry (SIMS). Mechanical and tribological characterizations were performed with a micro/nano- indenter, in order to measure coating nanohardness and Young's modulus trough Berkovich indentation and the coefficient of friction and failure properties trough Rockwell C scratch test.

The obtained results allow for a comprehension of the effect of the particular deposition condition on the sample characteristics and in turn for the mastering of its final mechanical and tribological properties. A series of sample with excellent mechanical properties, competitive with the state of the art of similar coatings deposited with other techniques were finally obtained.

1. *STATE OF THE ART IN PLASMA ASSISTED PHYSICAL VAPOR DEPOSITION*

Several techniques can be adopted for the deposition of thin films from vapor phase, which exploit either chemical or physical solutions: we speak respectively of Chemical Vapor Deposition (CVD) and Physical Vapor Deposition (PVD).

In this chapter, we will briefly summarize the PVD technique named magnetron sputtering based on plasma assistance for sputtering process: in this situation, atoms or ions condense on the surface of the substrate after being ejected from the target by ion bombardment.

1.1 **DC glow discharge**

We start by defining the plasma as "a quasineutral gas of charged and neutral particles which exhibits collective behavior" [3]. The term "quasineutral" refers to the property of an ideal plasma to possess equal density of positively and negatively charged particles, $n_e \approx n_i \approx n$, so that, on the average, neutrality is maintained. n is called plasma density, and is, in general, sensibly lower than the overall density of neutral particles.

The term "collective behavior", instead, refers to motions that depend not only on local condition, but on the state of the plasma in remote regions as well, because of long-range Coulomb forces that arises during local charge agglomeration or motion.

Glow discharge is the plasma formation region between two electrodes that is employed in PVD deposition chambers to generate the sputtering ions. It must be underlined that the glow discharge is not an ideal plasma, but plasma theory can be adopted to treat in a first approximation the behavior of glow discharge processes.

In (Figure 1.1) it is represented the general architecture of a discharge: plasma is formed between two electrodes to which it is applied a DC or even a RF bias voltage. The filling gas that produces the discharge is commonly an heavy inert noble gas, such as Ar or Xe, that possess a quickly rising ionization cross section for electron energies just above the ionization threshold.

The discharge is composed by several components. We can distinguish:

- the so-called negative glow region, formed by a bright glow that is the result of the excitation and subsequent recombination process of the inert gas filling the chamber;
- the positive column, is the region of the discharge which more nearly resemble a plasma;
- three dark spaces: between the negative glow and the positive columns (Faraday space) and respectively in front of the anode and the cathode. These last regions are called sheaths, and are region of net space charge were an electric field is established.
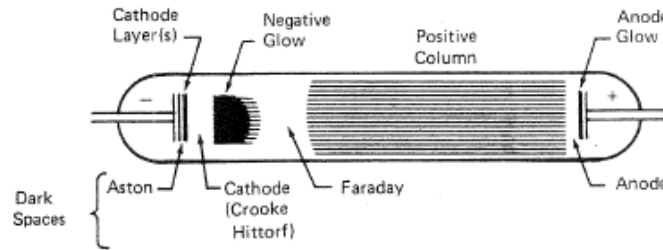
Figure 1.1   Schematic representation of a DC glow discharge in a vacuum tube filled with noble gas [4].

It has been pointed out that, when the two electrodes are brought together, the cathode dark space and negative glow are unaffected, whilst the positive column shrink, and eventually completely disappears if the inter-electrode separation becomes just a few times the cathode dark space thickness [4].

It is interesting to look at the voltage distribution across the glow discharge region (Figure 1.2): first of all the plasma does not take a potential intermediate between those of the electrodes, but it is the most positive body in the discharge. This is due to the higher kinetic energy of light electrons, with respect to heavier slow ions, that can escape from the plasma region leaving a positive charged space behind. Moreover, the electric fields in the system are restricted to sheaths at each of the electrodes, which voltage is such that to repeal electrons and attract positive ions.
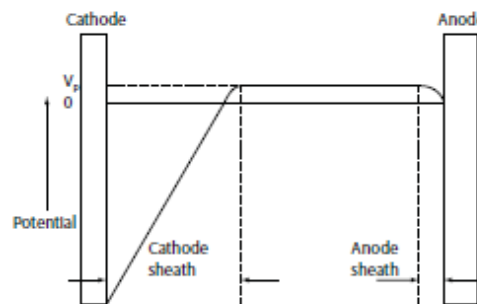
Figure 1.2   Voltage distribution in a DC discharge process [5].

To maintain a steady state discharge there must be sufficient ionization to maintain an equal ion-electron pair generation rate, and there must be sufficient energy input to compensate the loss on the electrodes and on the walls of the system. Thus electrons play a fundamental role in discharge maintenance, because they constitute the major source of ionization: they can be emitted from solid surfaces due to the impact of ions, electrons, neutrals and photons.

The principal source of secondary electrons, e.g. those electrons ejected as a consequence of the collision of one particle with a surface, is the cathode that, in a sputtering process, is constituted by the target. When they are produced, electrons are immediately repelled by the potential difference between the cathode and the plasma, leading to the formation of a positively space-charge sheath in front of the electrode, where an electric field progressively decreasing to zero at the interface between the negative glow and the dark region is established.

The cathode sheath region is divided into three internal parts: a quasi-neutral pre-sheath or transition region, where there exist a low electric field that pre-accelerate ions entering in the sheath (this is called Bohm region); a region of the extent of a few Debye lengths in which the

4

electron density rapidly becomes negligible; and finally a region of space charge region current flow, which is crossed by the fast secondary electrons accelerated towards the glow.

On the other hand, ions are originated primarily in the negative glow region and enter the sheath with a negligible kinetic energy: in the absence of collisions, they would travel the dark space and hit the electrode with an energy equivalent to the sheath voltage.

Similarly to cathode region, anode sheath accelerates secondary electrons into the glow, and at the same time accelerates ions from the glow onto the anode or onto any substrate there. Anode's sheath is thinner than the cathode's one of about an order of magnitude, and this implies that electron density does not go to zero at the anode surface, and that the dark region can be considered essentially collisionless and not a source of ionization.

The glow region is an ionized gas of approximate charge neutrality, which is constantly crossed by accelerated electrons from the sheaths, that act as a source of energy and glow maintenance through ionization processes. This made the discharge a quite anisotropic medium that differ from the classical plasma definition.

We can identify three types of electrons [4]:

   i.   primary electrons from the cathode, which retain practically all the momentum acquired by acceleration across the cathode sheath, and hence are directional;
   ii. secondary electrons, moving in random direction with a Maxwellian distribution around the primary beam energies. They are the products of ionizing collision or fast electrons which have lost much of their energy;
   iii. ultimate electrons, which have become thermalized to the plasma temperature and possesses the highest density ($\sim 10^3$ times the density of the primaries and secondary's [4]).

It was found that fast electrons do not cause enough ionization to sustain the glow, as they would preferentially loss low amount of energy trough collisions. The main source of glow ionization is indeed thermalized electrons, which possess lower ionization cross-section, but because of their low energy, they are trapped inside the glow region. As they are continuously reflected at the electrode's sheaths, the effective path length is increased the necessary to maintain the ion and electron densities by electron impact ionization of ground state argon atoms. Possible minor additional contributions come from ionization of metastable Ar atoms in the glow, and by either electron impact ionization or ion impact ionization in the cathode sheath.

1.2 Principles of sputtering

An ion colliding on a solid target can undergo a series of different processes:

- It can be reflected at the surface and subsequently neutralized by coalescence with an electron;
- It can cause the ejection of fast secondary electrons from the target;
- It can be implanted in the target, if the striking energy is sufficiently high;
- It can cause structural rearrangements of vacancies and interstitials in the near surface of solid material;
- It can cause collisional cascade in the target material, determining the ejection of some atoms or molecules. This ejection process is called sputtering.

Sputtering is a widely applicable and versatile process that can be applied both as an etching- cleaning process, that erode progressively the target's surface, both as a deposition

process of thin film. We will briefly describe the conventional sputtering systems adopted for coating deposition.

The material we wish to sputter will constitute the solid target, which become the cathode of an electrical circuit, and has a high negative voltage V (DC) applied to it (Figure 1.3). The substrate on which the coating will be deposited is placed on an electrically grounded anode a few centimeters away. In the deposition chamber is firstly made an appropriate vacuum level, in order to remove impurities and to exclude any other sources of ionization different from secondary and thermalized electrons coming from the electrodes.
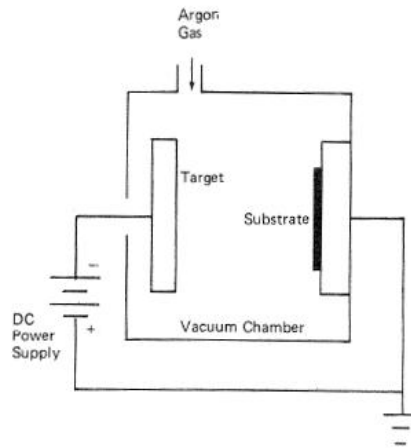

Figure 1.3   Schematic representation of a DC sputtering system [4].

As previously stated, heaviest noble gases are commonly adopted as plasma source mainly because of two characteristics: they are inert, thus they don't react with the target or either with the growing film if they are incorporated in the structure; and they possess a high sputtering yield, S, that is defined as the number of target atoms (or molecules) ejected per incident ion. This quantity depends on the masses of incident ion and target atom, m_i and m_t respectively, and on the energy of the incident ion E that is deposited in a thin layer near the surface, through the relation:

$$S = \frac{3\alpha}{4\pi^2} \frac{4m_i m_t}{(m_i + m_t)^2} \frac{E}{U_0},$$

(1.1)

where U_0 is the surface binding energy of the material being sputtered, and α is ma monotonic increasing function of m_t/m_i which has values of 0,17 for m_t/m_i =0,1 , increasing up to 1,4 to m_t/m_i = 10 [4].

This relation is valid for ion energies up to about 1 keV, because at higher energies S may even decreases as ion implantation becomes dominant.

Two other aspects that influence the deposition process are the pressure in the chamber, and the V-I relationship applied at the electrodes. In the first case, it is found that glow discharge impose a lower pressure limit necessary to the sustenance of ionization collision. On the other hand, pressure couldn't be increased too much otherwise material sputtered form the target would undergo collision with gas atoms on their way to the substrate, leading to a decrease in deposition rate. The operating pressure range for direct current (DC) sputter deposition is usually between 40×10^{-3} and 160×10^{-3} mbar [4].

On the other hand, the target-current voltage is essential to determine the sputtering yield and the emission rate of secondary electrons that maintain the glow discharge.

Equation (1.1) states that the sputtering yield depends linearly on the energy of the incident ions up to several tens of keV. The upper limit to target voltage is determined by the hindrance of X-ray production.

Moreover, it must be noted that a V-I discharge relationship does not mean that the flux of sputtering particles at the cathode is equivalent to I, or that the sputtering particles will all have an energy of V electronvolts: in fact, cathode current is carried by both incident ions and secondary electrons; on the other hand, not all the VI power input goes into the target because of collisional events. It is found that the voltage required to maintain a glow discharge having a current density of $0,1 \div 2,0$ mA/cm^2 is usually in the range of 500-5000 V [4].

As previously stated, sputtering is a rather versatile process adopted in many deposition processes. It allows the deposition on relatively extended surface, and it produces coatings with good uniformity and adhesion properties. On the other hand, the principal drawbacks of simple sputtering systems are a slow deposition rates, a relatively high vacuum range that produces porous films, low secondary electrons production to sustain the discharge and sputtering ions, and target degradation due to the continuous bombardment.

To overcome these limitations, some possible solutions have been developed: (i) RF excitation to produce ionization enhancement, (ii) injecting more electrons in the discharge by using a hot filament as an electron source, or finally (iii) trapping electrons with a magnetic field, in order to increase their mean free path before recombination.

In the next paragraphs we will describe the basic principles of planar magnetron configuration, which was a really breakthrough for industrial coating when was introduced in the 1970s, and is nowadays a widely adopted deposition mechanism.

1.3 Magnetron sputtering

Magnetron sputtering is based on the addition of a magnetic field parallel to the target surface, in order to trap electrons in a gyration motion that increase their ionization effect. The electron path is affected by the simultaneous presence of an electric, *E*, and magnetic, *B*, field that are in general perpendicular (Figure 1.4), thus their equation of motion can be derived from Lorentz equation:

$$\vec{F} = e(\vec{E} + \vec{v} \times \vec{B}),$$ *(1.2)*

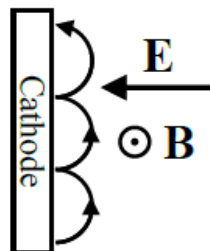where *F* if the force acting on the electron of velocity *v* moving a *E* and *B* fields.

Figure 1.4   Schematic representation of electron movement and gyration in the case of perpendicular electric and magnetic field [6].

In the absence of the electric field, the electron would gyrate around magnetic field lines with a cyclotron frequency and gyration radius:

$$\omega = \frac{eB}{m_e},$$ (1.3)

$$r = \frac{m_e v_{e\perp}}{eB},$$ (1.4)

Where m_e is the electron mass, e its charge and v_e the component of the velocity perpendicular to the field vector $\boldsymbol{B}$. Typically, the electron would gyrate many times around a magnetic field before colliding with other particles.

The simultaneous presence of the electric field of the cathode sheath changes the orbits from circular to cycloidal, leading to a net drift perpendicular to both E and B field vectors (along the guiding center direction), called ExB drift:

$$\vec{v}_{ExB} = \frac{\vec{E} \times \vec{B}}{B^2}.$$ (1.5)

The closed drift of electrons is sometimes referred to as the magnetron motion, and the associated azimuthal electric current is also called the Hall current. For typical operation of a direct current magnetron, the Hall current exceeds the discharge current by roughly an order of magnitude [7].

The typical geometry of a planar magnetron is represented in (Figure 1.5):
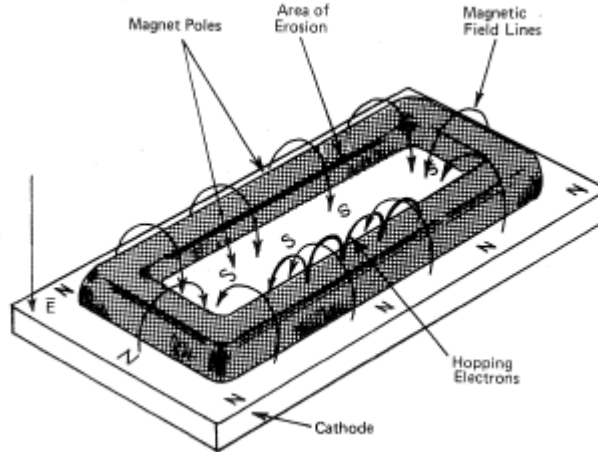
Figure 1.5   Planar magnetron sputtering configuration [4].

It must be noted that both electric field and magnetic field are strongly non uniform, and additional drifts can affect the motion of electrons, such as the $\boldsymbol{B}$x$grad\boldsymbol{B}$ or $grad\boldsymbol{E}$ drifts for non-uniform B, or E respectively [7], making the electron path actually very complex.

Ions are generally not affected by this motion, because their gyration radius usually exceeds the characteristic system length, indeed they are only affected by the accelerating electric field of the sheath, as previously mentioned.

Thanks to this magnetic electron trapping near the target, the loss process of fast electrons going to the anode and to the walls is strongly reduced, determining a parallel diminution of substrate heating by electron bombardment.

Nevertheless, magnetron sputtering presents some drawback: the magnetic field causes an effective concentration of the glow in a localized area (racetrack), determining anisotropic target erosion, which in turn causes deposition rates to vary with the progressive consumption of the cathode. Furthermore, magnetron sputtering is subjected to the frequent phenomenon of

8

arcing, that is a local concentration of part of the discharge current on superficial defects, that cause the ejection of melted droplets of target material that can arrive to deposit on the growing film causing defect incorporation.

Another problem of conventional magnetron systems is that the plasma is confined in a limited region of about 60mm extension in front of the target [8]. Substrate positioned outside this region of high plasma density experience insufficient ion bombardment to modify the microstructure of the growing film, and it is therefore difficult to produce fully dense, high quality coatings on large, complex substrates.

This problem has been overcome by the development of the unbalanced magnetron configuration, and their incorporation in a multiple-magnetron system.

An unbalanced magnetron is designed such as, for example, the magnetic field strength of the outer magnets is greater than inner magnets, such that some field's lines extend farther into the chamber. As a consequence, high ion currents can be transported to the substrate, increasing ion bombardment of the coating structure (Figure 1.6).
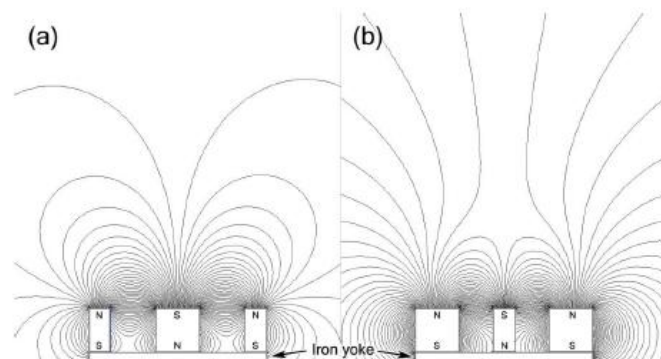
Figure 1.6   Cross section views of planar rectangular (a) balanced, and (b) umbalanced magnetron configurations, form finite element simulation of the magnetic fields [6].

Additional improvement of plasma confinement is achieved by the so-called Close Field Unbalanced Magnetron Sputtering (CFUBMS) configuration, in which two or four magnets of opposite polarity are installed opposed to each other, constituting a closed magnetic field trap between the magnets. This implies that few electrons are lost to the chamber walls and a dense plasma is maintained in the substrate region, leading to high levels of ion bombardment of the growing film.

The multiple-magnetron configuration is nowadays well suited to the deposition of coatings of different stoichiometry, of alloys, and also, trough the difference in sputtering rate between targets, to the deposition of complex structures, such as multilayers or graded films.

The magnetic fields in a conventional magnetron, an unbalanced magnetron and a close field unbalanced magnetron are compared schematically in (Figure 1.7).

Figure 1.7   Schematic representation of magnetic field and plasma confinement in a conventional, unbalanced and close field unbalanced magnetron sputtering [8].

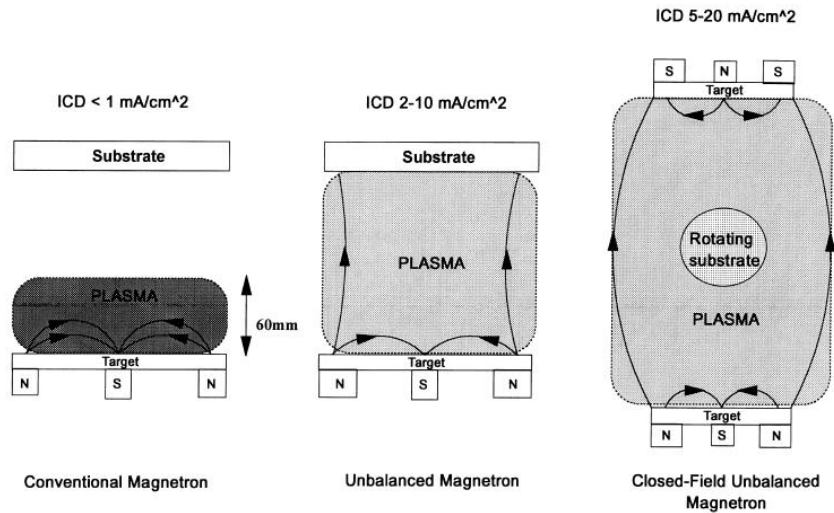Magnetron sputtering configurations are commonly adopted with a DC supply: in DCMS systems the discharge voltage is typically in the order of 300 V to 500 V, resulting in current densities on the target of the order of a few $mAcm^{-2}$. This provides plasma densities in the order of 10^{14}-10^{16} atoms/m^3 [9].

Even though DCMS systems greatly ameliorate the performances of sputtering deposition of thin films, it possesses still some limitations, because the degree of ionization of sputtered material is inferior to 10% [9]. To overcome this problem, bias voltage can be applied to the substrate, in order to increase the average energy of the incident ions: however, high bias voltage may cause the implantation of Ar^+ ions into the film, leading to the generation of lattice defects, deterioration of the quality of the film/substrate interface and poor adhesion [2].

The desire to limit film damage and simultaneously enhance the degree of sputter material ionization, drove many researchers to develop alternative or complementary solutions to DCMS. One of the most popular configurations developed was proposed by Kouznetsov et al [10] in the mid 90s' and it is called High Power Impulse Magnetron Sputtering (HiPIMS or HPPMS). This technique and its working principles will be briefly described in the next paragraph.

1.4 High Power Impulse Magnetron Sputtering

High Power Impulse Magnetron Sputtering (HiPIMS) can be defined as "a pulsed sputtering technique where a very significant fraction of the sputtered atoms becomes ionized" [7]. When Kouznetsov and coworkers [10] first proposed this approach, they demonstrated that the high pulse current applied to a Cu target, resulted in the formation of an ultradense plasma in which the total ion flux was two order of magnitude higher than that of a DCMS plasma, and sputtered material ionization reached ~70%.

Successive measurements reported that electron density in HiPIMS discharges is in the order of 10^{18} m^{-3}, which is much higher than the values of 10^{14}-10^{16} m^{-3} obtained by DCMS [2].

The experimental realization of HiPIMS requires power suppliers different than those used in conventional magnetron sputtering processes, but that can be easily implemented in a preexistent DCMS apparatus.

10

Indeed, a technical definition of HiPIMS can be "a pulsed sputtering where the peak power exceeds the time-averaged power by typically two orders of magnitude" [7]: in practice, the power suppliers must be able to provide the target with pulses of high power density (typically in the range of a few $kWcm^{-2}$), while maintaining the time-averaged target power density on values similar of those during DCMS (i.e. a few Wcm^{-2}). The low average target power density is necessary to avoid cathode overheating and damage of the magnets or even melting of the target.

The basic architecture of an HiPIMS power supplier is represented in (Figure 1.8): a DC generator is used to load the capacitor bank of a pulsing unit, which is connected to the magnetron. The charging voltage of the capacitor ranges typically from several hundred V up to several kV. The stored energy is released in pulses of defined width and frequency using transistors with a switching capability in the μs range, located between the capacitors and the cathode. The pulse width (or pulse-on time) ranges, typically, from 5 to 5000 μs, while the pulse repetition frequency spans from 10 Hz to 10 kHz. In those conditions, peak target current densities may reach values up to several Acm^{-2}, which are considerably higher than DCMS ones [2].
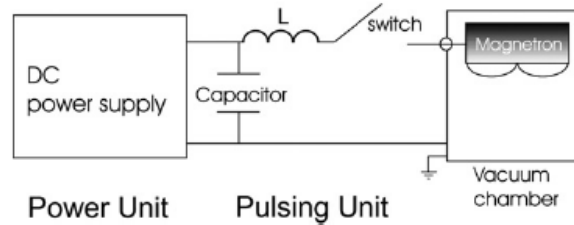
Figure 1.8   Basic architecture of an HiPIMS power supplier [2].

In general, power generators are designed to deliver voltage pulses with a rectangular shape, that is with a constant voltage value during the pulse-on time (Figure 1.9). A general feature observed in the shape of the current-voltage time relation, is a more or less significant delay of the current rise with respect to the application of the voltage pulse (Figure 1.9). This time delay, t_d, is ascribed to the contribution of two main components: a statistical time lag, t_s, for the appearance of the first electrons in the electric field generated between electrodes, and a formative time lag, t_f, corresponding to the time required for the development of the discharge:

$$t_d = t_s + t_f.$$

(1.6)

Figure 1.9   Rectangular shape of the voltage pulse applied to the target by an HiPIMS generator, with superposed the recorded current on target. [2]

As a consequence of the high ion to target current, arcing is far more frequent in HiPIMS than in DCMS, and their effects are more detrimental due to the concentration of all HiPIMS discharge in a small cathodic spot. Therefore, sophisticated electronics must be used in conjunction with HiPIMS power suppliers in order to stop the process for a short time when an arc is detected. Nevertheless, there can be some resid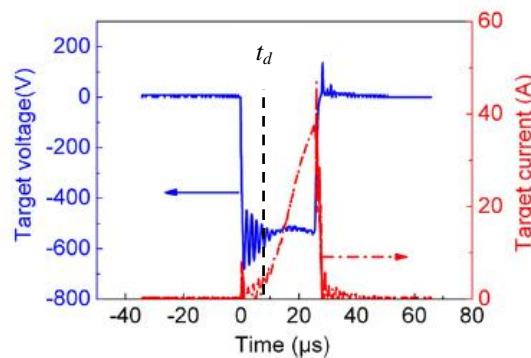ual energy in the discharge circuit, even after arc detection, that leads to the ejection of macroparticles from the target that deteriorates coating quality.

HiPIMS parameters such as pulse on/off time and power supply, strongly affect plasma properties trough the variation of the V-I relationship of the target. For example, by increasing the pulse-off time, both the target voltage and the peak current increase, and the shape of the target current modifies, as depicted in (Figure 1.10).

On the contrary, by keeping constant the average power and increasing the pulse-on time, in has been shown [11] that the discharge can evolve from an Ar-sputtered to a self-sputtered (sputtering by the target metal ion), which causes sensible deposition rate deviation from the typical values of a DCMS process.
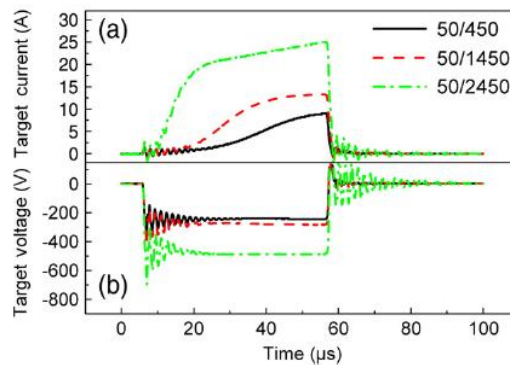
Figure 1.10   Effect of the pulse on/off time configuration on the HiPIMS process [2].

Another element influencing the glow discharge plasma is the peak target current. According to Thornton [12], the target-voltage relation of a magnetron system is a power law:

$$I \propto V^n, \tag{1.7}$$

Where *n* ranges from 5 to 15 in DCMS processes, whereas in HiPIMS it changes from values similar to DCMS at low target voltages, to values close to unity when high voltages are applied (Figure 1.11) [2]. Thus, plasma can change from a DCMS-like to an HiPIMS-like if sufficient current density is supplied to the target.
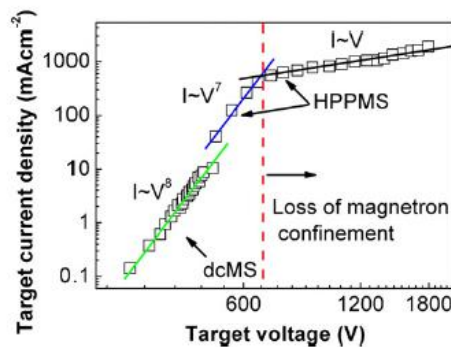
Figure 1.11   Current-voltage curves of a magnetron during operation in DCMS and HiPIMS mode. The change of the slope from 7 to 1 at a voltage value of 650V indicates loss of the electron confinement [2].

12

The effect of different pulse lengths on HiPIMS plasma properties, was investigated by Anders [7], who reported that by using long pulses up to 400μs and a target material with high self-sputtering yield, the discharge was given the time to evolve into a metal discharge phase dominated by self-sputtering of atom targets, which is sufficiently energetic to produce multiple charged particles. Nevertheless, this self-sputtering regime strongly reduce the deposition rate, as the major part of the target ions are trapped in front of the cathode surface to enhance the sputtering process.

The power and the pulse configuration are not the only aspects affecting the plasma discharge. Anders [7] found that the current evolution during the pulse is strongly affected by the secondary electron emission from the target; these two quantities are linked trough the relation:

$$ j_i = \frac{j_{Tav}}{1 + \gamma_{SE}}, \qquad (1.8) $$

Where j_i is the ion target current density, j_{Tav} the average target current density and γ_{SE} is the secondary electron emission yield. This last quantity is dependent on the nature of the target material and of the sputtering ions, as well as on their energy. Two different emission mechanisms can be identified: the so-called potential emission and kinetic-emission of secondary electrons. In the first case, applicable to those ions of impinging energies below 1keV, only those ions possessing sufficiently high ionization potential energy, E_{pot}, are capable to generate secondary electrons, according to the empirical relation [7]:

$$ \gamma_{SE} = 0,032\,(0,78\,E_{pot} - 2\phi), \qquad (1.9) $$

where ϕ is the work function of the target material. For singly charged metal ions (e.g. Ti$^+$, Cr$^+$, Cu$^+$) E_{pot} is generally smaller than 2ϕ [2], which implies that these ions cannot induce potential emission of secondary electrons. If the ions possess energy higher than 1 keV, then kinetic emission take place and multiple charged metal ions are formed. As a result, they can possess enough energy to produce potential emission, thus the plasma can evolve into a sustained self-sputtering regime.

The high flux of sputtered atoms and reflected ions from the target was found to greatly influence the gas in front of the cathode, because of the phenomenon of rarefaction (or "sputtering wind") [13]: as a result of this intense ion flux, gas atoms would undergo many collision, they would be displaced and locally heated, determining a reduction of gas density. This rarefaction was still present in DCMS, but its effects are stronger with HiPIMS due to the higher target current. Rarefaction is a wave-like effect: as soon as gas atoms are pushed away from the cathode, ion current to the target, which is formed by both ions and secondary electron contribution, is reduced. Thus, the effect of rarefaction is less intense and the gas starts to refill the low-density zone in front of the target, starting again the sputtering process.

HiPIMS technique has been proved to provide high density plasma with ionization degrees significantly larger than those in a conventional magnetron sputtering discharge: in particular, ionization fraction reaching up to 30% for Cr, 70% for Cu and 60% for Ti has been reported [14]. Nevertheless, HiPIMS deposition rates are systematically lower than those obtained with simple DCMS at the same average target power [2,5]: the corresponding deposition rate efficiencies (Åmin^{-1}/Wcm^{-2}) range typically from 15-40% of those of DCMS [6].

In general, from simple considerations, a loss of deposition rate should be expected, irrespective of the deposition process used, if performing constant average power (P_{Tav}) deposition processes in which the target voltage is increased, according to the relation:

$$P_{Tav} = I_{Tav} \times V_T = const.\qquad (1.10)$$

HiPIMS adopt higher target potential than those commonly employed in DCMS ($400 \div 2000$ V and ~ 300 V respectively), thus lower ion current to the target, I_{Tav}, implies lower erosion rates. But relative HiPIMS to DCMS deposition rates reported in literature are even lower than those corresponding to this simple consideration [2].

Two main aspects influence this behavior: (i) the interactions of the plasma species with the target and their effect on the target erosion rate, and (ii) the transport of the ionized sputtered species from the target to the substrate.

From a modeling of the mechanism of ionization and re-direction to the target of sputtered ions in a HiPIMS system, it was found that deposition rate decreases as the ionization of the sputtered material and/or the redirection of ionized sputtered species to the target are increased because, evidently, a minor amount of charged particles managed to escape from the target region [15]. This model was further expanded to account for the transport of the ionized and also neutral sputtered species [16], because this aspect plays a significant role in the magnitude of deposition rate. In general, the trajectories of sputtered particles are determined by the velocity angular distribution at the target and by the collisions with gas atoms. The addition of an electric and magnetic field can change the energy and the impinging direction of the charged particles, determining the deposition along off-normal directions.

The mathematical expression derived for the HiPIMS to DCMS deposition ratio, a_D, is a function of the ionization degree of sputtered material (β), the sputtering yield by Ar ions (Y^{Ar^+}) and by self-sputtering (Y^{M^+}), as well as the efficiency of transport for neutral (ξ_n) and ionized sputtered species (ξ_i):

$$a_D = \frac{(1-\beta)\left(1-\gamma+\gamma\frac{\xi_i}{\xi_n}\right)+\beta(1-\sigma)\frac{\xi_i}{\xi_n}}{1+\beta\sigma(Y^{Ar^+}-Y^{M^+})}, \qquad (1.11)$$

σ is the fraction of ionized sputtered species which are confined in the target's vicinity and are redirected to the target for sputtering, whereas γ is the probability ionization for sputtered atoms in the bulk plasma. Equation (1.11) includes both the previously exposed target-plasma interactions and influence of erosion rate, and the effect of transport of ionized sputtered species. Moreover, it predicts an increase of HiPIMS rate when the efficiency of the ion transport (ξ_i) and the ionization of sputtered atoms in bulk plasma (γ) are increased.

Another effect affecting HiPIMS deposition rate is the radial acceleration experienced by charged particles in HiPIMS systems, as a consequence of strong plasma instabilities: Lundin et al. [5] showed that the angular distribution of ionized sputtered material follow an anomalous transport along azimuthal direction, rendering HiPIMS an off-normal deposition technique with respect to DCMS. This implies that a minor amount of sputtered atoms reached a substrate facing the target, but on the contrary can facilitate the deposition on complex-shaped objects positioned also perpendicularly to the target surface [5]. This important feature differentiates HiPMS from the more directional DCMS technique.

1.5 Reactive Magnetron sputtering

The deposition of metal-compound materials require in some cases the adoption of reactive gases as precursors for a specific atomic species incorporation. This method is called reactive sputtering, and it is widely adopted for low temperature deposition of compounds of arbitrary stoichiometry. The addition of a reactive gas into the sputtering atmosphere, leads to target

coverage (chemisorption) and/or implantation of the reactive species in the sub-surface layers. Normally, the sputtering yield of the compound material is substantially lower than the sputtering yield of the elemental target material [17]. This causes the deposition rate to decrease as the content of reactive gas in the chamber is increased.

Reactive sputtering is a strong non linear process, as it was found that the deposition rates changes in a different way as the reactive gas flux Q_{tot} is increased or successively decreased: this is called hysteresis effect, and has been first modeled by Berg and co-workers [18] form observation of optical emission signals of metallic species (Figure 1.12a). In a similar way, the partial pressure of the reactive gas, P, undergoes a hysteresis process (Figure 1.12b): its values remains very low until reaching the upper limiting value of the hysteresis width, where it suddenly rises. A successive diminution of reactive gas supply maintains the partial pressure to relative high value, with respect to the initial increasing sequence. This implies that more gas is consumed for compound formation in the first phase, when the target is progressively poisoned.
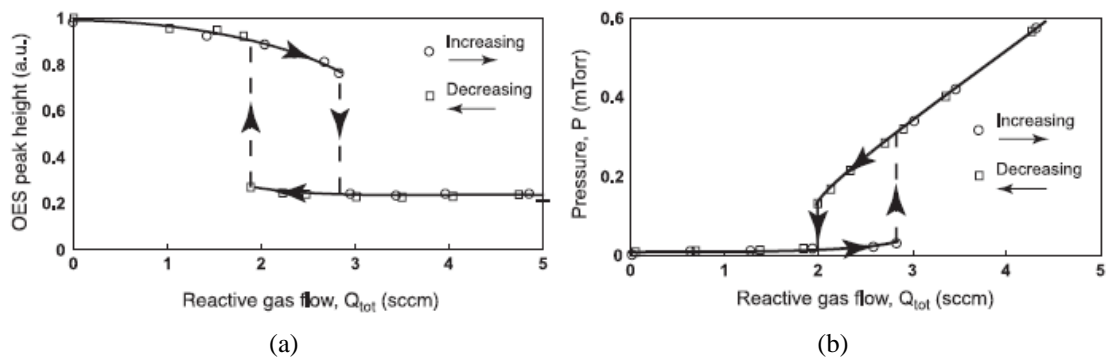

(a)   (b)

Figure 1.12 Experimental curve representing the hysteresis behavior in reactive processes: as a function of the reactive gas flux Q_{tot} are represented (a) the optical emission from sputtered metal atoms that represent the sputter erosion rate, and (b) the partial pressure variation, P, of the reactive gas. [17]

1.5.1 Berg's model for reactive sputtering

A first modeling of reactive sputtering process has been proposed by Berg and coworkers [17-19]. They first assumed a target of area A_t in front of a collecting surface of area A_c. A pump is connected to the vacuum chamber having a constant pumping speed S for the gas involved. The total flow rate of the reactive gas is denoted by Q_{tot}, and the partial pressure P. According to the schematic representations of (Figure 1.13b), a fraction θ_t of the target will be covered by a monolayer of compound molecules, whereas the remaining fraction (1- θ_t) consists of non-reacted target atoms. All sputtered material is assumed to be uniformly collected, and the covered substrate area is denoted by θ_c. It is also assumed that the ratio between the electron and the ion currents does not change during processing, and the sputtering contribution by ionized reactive gas is neglected.
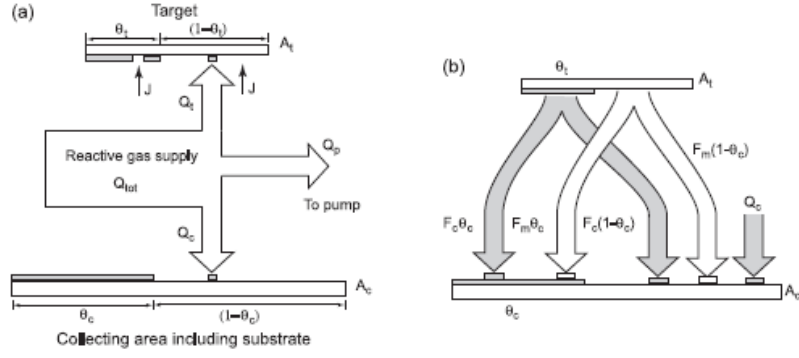
Figure 1.13   Schematic representation of the Berg's model for reactive sputtering. Notation refers to the model developed by Berg [17].

During the process the target will be sputter-eroded, and the elemental compound forming θ_t is eroded in form of molecules. The flux of material arriving to the substrate can be divided in three components: a total number of out-sputtered compound molecules per unit time from the target, F_c, a number of sputtered non-reacted elemental target atoms per unit time, F_m, and a number of neutral reactive molecules per unit time, F:

$$F_c = \frac{J}{q} Y_c \theta_t A_t,$$

(1.12)

$$F_m = \frac{J}{q} Y_m (1-\theta_t) A_t,$$

(1.13)

$$F = \frac{P}{\sqrt{2kT\pi m}},$$

(1.14)

where J is the ion current density, Y_c and Y_m the sputtering yields for compound molecules and target atoms respectively and q is the elementary electronic charge. F derives from gas kinetics: k is the Boltzmann constant, T is the temperature and m the mass of the gas molecule.

Compound formation by reaction between reactive gas and non-reacted target atoms will consume Q_c reactive gas molecules per unit time, according to the relation:

$$Q_c = \alpha F (1-\theta_c) A_c,$$

(1.15)

where α is the probability (sticking coefficient) for a colliding neutral reactive gas molecule to react with a non-reacted atom in the $(1-\theta_c)$ fraction of the collecting area.

The steady state condition for the maintenance of a θ_c fraction of compound material at the substrate is:

$$2Q_c + F_c(1-\theta_c) = \theta_c F_m,$$

(1.16)

which, together with the steady state condition for the target :

$$\frac{J}{q} Y_c \theta_t = \alpha 2F (1-\theta_t).$$

(1.17)

enables the determination of θ_c.

The total sputtering rate R_m of metal atoms from pure target and compound removal can be expressed as:

$$R_m = \frac{J}{q}[Y_m(1-\theta_t)+Y_c\theta_t]A_c.$$

(1.18)

16

Knowing the compound fraction θ_c at A_c enables to derive the expression for the deposition rate D:

$$D = c_1 R_m (1 - \theta_c) + c_2 R_m \theta_c, \qquad (1.19)$$

where c_1 and c_2 are constants accounting for unit conversion.

The reactive gas model can be considered also from the point of view of the relation between partial pressure variation and reactive gas consumption (Figure 1.13a), considering that the total reactive gas supply Q_{tot} is the sum of three contributions:

$$Q_{tot} = Q_t + Q_c + Q_p = \alpha F (1 - \theta_t) A_t + \alpha F (1 - \theta_c) A_c + SP, \qquad (1.20)$$

Where Q_t, Q_c, Q_P are the consumption (number of molecules per unit time) at the target, at the collecting area and at the pumping system respectively.

Combining equation (1.20) to the previous equations makes it possible to find the relation between P and Q_{tot} or P and the erosion rate R. Results of mathematical computation are presented in (Figure 1.14) and are characterized by an S-shaped behavior in the hysteresis region, in which one value of Q_{tot} may be satisfied by three different values of P and D simultaneously.

We can see from (Figure 1.14a) that, when the target is in its metallic state (i.e. from $D = 1$ to point P_4 in the curve), the sputtering rate is high, but the fast increase to a complete target coverage by the reactive compound (poisoned mode, from point P_3), leads to a great diminution of the deposition rate.

The control method used for the injection of the reactive gas in the chamber has a direct influence on the poisoning of the target. For the deposition of stoichiometric films with good properties and relative high deposition rates, it is desirable to operate in the transition region between the elemental and poisoned state of the target [20], but the achieving of a precise control of reactive dynamics is by far a great issue.

Two methods can be adopted:

1. Flow control of the reactive gases, which was the first method adopted, but suffer of large instability when passing from the metallic to the poisoning mode. Typically, an avalanche transition occurs (Figure 1.12) and operating at an intermediate point of the transition region become quite difficult as any small perturbation in the process result in the sudden change of gas partial pressure.

2. Partial pressure control: Berg et al [17] demonstrated that internal transition points can be reached only with a partial pressure control of the reactive gas, which is achieved through a feedback signal recorded trough optical emission spectrometers (OES), mass spectrometer or either cathode voltage.

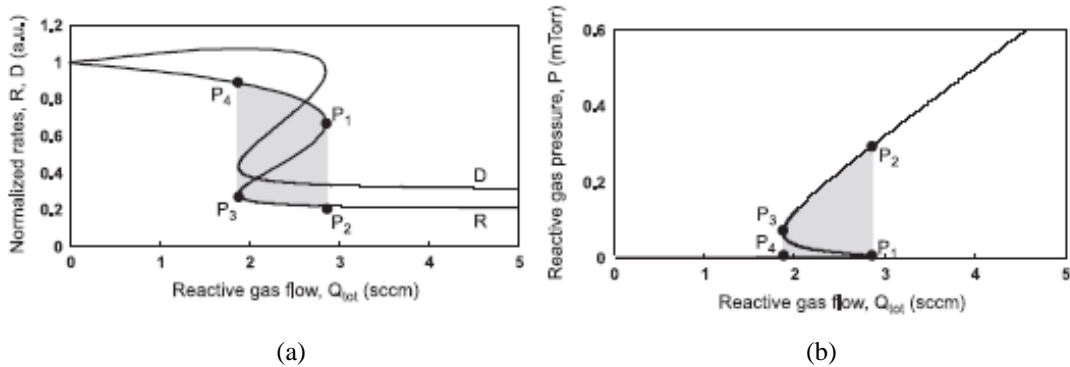(a)   (b)

Figure 1.14   Calculated values of (a) target erosion rate R and deposition rate D, and (b) partial pressure P, in function of the supply rate of the reactive gas from Berg's model [17].

The parameters influencing the hysteresis effect are several. A general rule is that, if the derivative $dQ_{tot}/dP<0$ in some region, the process will exhibit hysteresis [17]. Other deposition parameters affecting hysteresis behavior are:

i. Target material: for materials where $Y_c<<Y_m$, hysteresis is normally more pronounced than if Y_c is close to Y_m;

ii. Nature of the reactive gas: by changing the value of the sticking coefficient α, which may be considered as a materials constant, a variation of the hysteresis width is observed;

iii. System pumping speed, S: by increasing the pumping speed the hysteresis width decrease, until a critical unrealistic high limit for which $dQ_{tot}/dP>0$;

iv. Target to substrate distance: by keeping this parameter small will cause a decrease in the hysteresis width, as the collecting area is reduced;

v. Target-ion current: calculation shows that different ion current levels only produce a magnification of the curves, making it impossible to eliminate the hysteresis region by increasing the target ion current. On the other hand, it can be employed as a control processing parameter, because low values of ion current correspond to a poisoned target, whereas the metallic target mode corresponds to high values of ion current;

vi. Reactive gas supply: if variations of reactive gas supply are allowed with a certain rate r, a new dynamic model is necessary. In this case, Kubart et al. [21] showed that the hysteresis curve will became wider the higher is r.

1.5.2 Two-gas reactive sputtering

In order to sputter deposit ternary compounds, reactive sputtering in the presence of two reactive gases is frequently adopted. The process is more complex, because both reactive gases compete in compound formation at the target as well as in compound consumption and condensation on the substrate.

Baránková et al. [22] first modeled two-gas reactive sputtering with one target using flow control. They investigate the hysteresis process of a system of N_2+O_2 reactive gases in Ar atmosphere, and they found that the degree of compound formation on the receiving surface of the target determines the position of the hysteresis loop in the reactive sputtering processing curve. The presence of a constant supply of one of the reactive gases, and the value it assumes, was found to strongly change the hysteresis behavior of the second gas. In particular, they identified two different processes:

1. when the oxygen flow was kept constant below the critical value for entering the transition region in a Ar/O_2 system, then the features of the hysteresis curve of nitrogen will be those of a simple Ar/N_2 system, only shifted towards lower values of φ_{N2}. The shift will be larger with higher φ_{O2}. The partial pressure of both reactive gases follow the avalanche of the sputtering rate accordingly to the hysteresis behavior (Figure 1.15a).

2. When the oxygen flow is above the value when the Ar/O_2 system enters the hysteresis region, then the hysteresis curve of N_2 will adopt the features of the Ar/O_2 system. Moreover, a trapping effect appears because the system does not return to high-rate metallic sputtering mode when φ_{N2} returns to zero. This phenomenon is evidenced by high level maintenance of O_2 partial pressure even when nitrogen supply in the chamber is reduced to zero (Figure 1.15b).
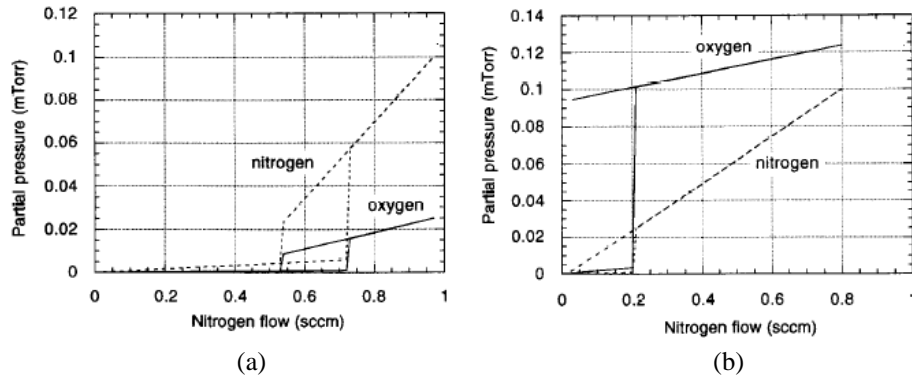
18

Figure 1.15   Calculated curves of partial pressure p_{N2} and p_{O2} vs. nitrogen flow at constant oxygen flow (a) below the hysteresis region and (b) in the poisoned regime of Ar/O$_2$ system. [22]

In order to control the two-gas reactive process, a simple flow control leads to unstable operations, due to the strong influence that the gases exert to each other.

Flow control of one gas with partial pressure control of the other could lead to a situation where one gases traps the target in a poisoned condition, but this effect may be attenuated when using gases with less pronounced hysteresis behavior (e.g. carbon-based gases with respect to oxygen).

The best solution would be the partial pressure control of both reactive gases through two different feedback signals [20], but this configuration is not always implemented in common deposition systems.

1.6   **Reactive sputtering HiPIMS**

Reactive HiPIMS (R-HiPIMS), is widely used in the deposition of oxides, nitrides and oxinitrides compounds. Similarly to reactive DCMS, it is subjected to the hysteresis effect, but its dynamics is far more complex, due to the presence of high peak current densities on the target. In traditional DC reactive sputtering, two mechanisms of compound formation take place [23]: chemisorptions of reactive species at the surface of the target, and ion implantation (direct and recoil), leading to a compound formation within the target surface. The implantation depth of the reactive species was reported to be of the order of 2,5 nm in a Ti target in a Ar/N$_2$ atmosphere [24].

In R-HIPIMS discharge, chemisorptions is expected to take place principally during the pulse-off time, because gas rarefaction during the pulse-on time hinders the activation of reactive species.

On the other hand, when high voltage is applied to the target, ion implantation is expected, together with a simultaneous cleaning process of part of the compound material at the surface.

This feature is very important in HiPIMS processes, because when the chemical affinity between the gas and the metal sputtered target is high, there is the possibility of a longer time for metallic condition recovery. This long lasting poisoning effect may leads ultimately to an artificial suppression of the hysteresis loop if the starting target surface was not perfectly cleaned [24].

Target pulsing parameters, such as frequency, peak voltage and pulse duration may affect the overall shape of the hysteresis loop. Audronis et al. [23] studied the hysteresis behavior of a reactive Ar/O$_2$ system with varying HiPIMS frequencies and constant power supply. Good control of reactive sputtering process was obtained by a modified Plasma Emission Monitoring technique (PEM) for R-HiPIMS [25].

They found that pulse frequency affect in a significant manner the hysteresis behavior. Looking at the hysteresis loop they recorded (Figure 1.16), they recognized five zones:

i. Zone A: the target is essentially in a metal state. When increasing the frequency, the transition point of optical emission drop shift towards higher flux values: this is ascribed to an increasing in duty cycle (i.e. the ratio between the pulse-on time and the cycle time [20]) that produce an enhancement of the sputtering rate.

ii. Zone B: the transition region. Transition to the poisoned regime occurs at nearly the same rate, despite of different frequencies, duty cycles, peak target voltages, etc. The shape of the transition phase may be influenced rather by changes in reactive gas supply [21].

iii. Zone C: the compound state. Different saturation levels of optical emission signal are recorded. This effect is ascribed to an increase in the pulse peak voltage with decreasing frequency, which results in a modified composition of the sputtered flux.

iv. Zone D: inverse of the poisoning transition. In this situation, higher frequencies means high duty cycle and consequently major sputtering rate, thus the depoisoning effect is more rapid.

v. Zone E: final metal state. The attaining of the pure metal state occurs at different rates, indicating the effect of ion implantation oxidation mechanism with varying the target pulse peak voltages.
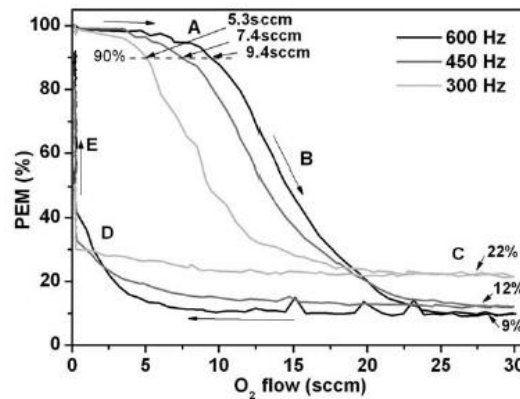

Figure 1.16   Hysteresis loop of R-HiPIMS obtained with a Ti target in a Ar/O$_2$ atmosphere at different HiPIMS frequencies [23].

Deeper understanding of the reactive HiPIMS process comes from the work of Hala et al. [14] on the study of plasma discharge evolution during reactive and non-reactive HiPIMS by time- and space-resolved optical emission spectroscopy.

In (Figure 1.17a,b) is represented the time evolution of the target current respectively in a non-reactive (a) and a reactive Ar/N$_2$ ambient (b), together with the optical emission evolution of different atomic species (target Cr, Ar and N$_2$ in molecular and ionized form). They identified four different phases in the discharge, of which only the first two are observed in a non-reactive ambient:

1. The Ignition phase (I), characterized by bright working gas emission and the development of a dense plasma region close to the target, as a consequence of ionization of working gas atoms and the simultaneous injection of metal sputtered atoms.

20

2. The Metal-dominated high current phase (M), characterized by self-sputtering process with a possible gas-ion sputtering contribution, during which the metal plasma expands outwards from the target.

3. Transient period (T), characterized by the transition to a high-voltage, low-current DCMS-like discharge, where self sputtering is no more the principal sputtering process.

4. Gas-dominated phase (D), characterized by further lower current and low plasma emission intensity, as a consequence of the voltage drop caused by limitations of the power supply.

Moreover, Hala et al. observed that, in reactive sputtering, plasma propagation changes its waveform during the pulse forming a conical and subsequently drop-like appendix extending far into the reactor. On the contrary, non reactive plasma propagates as hemispherical waves [14].

In a reactive ambient, the discharge in the proximity of the target is still dominated by Cr species, whereas the drop-like extension shows predominantly emission of excited N_2.
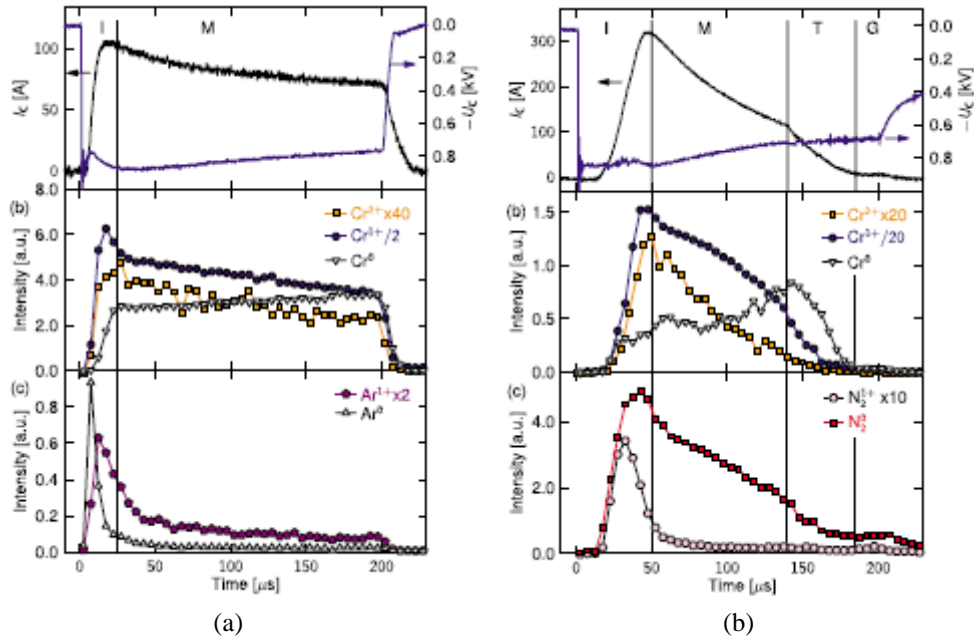

(a)   (b)

Figure 1.17   Time evolution of target current I_c and target negative voltage U_c in a non reactive ambient (a), and in a Ar/N_2 (1:1) atmosphere, together with OES line intensities evolution of target species (Cr) and gaseous species (Ar, N_2)[14].

1.7 Structure zone diagrams for thin film formation

The deposition conditions obviously affect the structure of the sputtered film. In order to describe the evolution of film microstructure by the variation of deposition conditions, Structure Zone Diagrams (SZD) are widely used tools. Their basic assumption is to use as few parameters as possible that can be significant for illustrating thin film evolution.

In order to develop an SZD that is universal and feasible, it should have axes that are directly related to the film growth processes, as opposed to primary parameters, such as target current, voltage, pressure, etc. For this reason, SZD is only a qualitative illustration of the physical reality of film properties resulting from growth processes, even though greatly explicative.

Many SZD exists, accordingly to the different features of deposition technologies.

The last basic model for polycrystalline films grown by PVD technique was proposed by Barna and Adamik [26] as an expansion of a pre-existent subdivision: film growth evolution is expressed as a function of the so-called homologous temperature, T_h, which is defined as the film growth temperature normalized by the melting temperature of the depositing film material (in Kelvin).

$$T_h = \frac{T_s}{T_m}. \qquad (1.21)$$

The SZD is composed of four regions (Figure 1.18):

1. Zone I: $T_h < 0,2$. In this region, due to the limited surface diffusion, the lateral size of the grains is determined by the nucleation density. The structure is principally fibrous, with high degree of pores and defects and random texture.

2. Zone T: $0,2 < T_h < 0,4$. This region is characterized by a competitive growth at the interface between faster and slower growing crystallographic planes, in which adatoms may possess different residence times. The morphology is typically characterized by V-shaped grains. When film thickness increase, fast growing planes prevail giving rise to a columnar dense morphology, smoother surface and strong preferential orientation (texture).

3. Zone II: $0,4 < T_h < 0,5$. In this region, bulk diffusion becomes significant giving rise to a dense columnar microstructure which can extend throughout all the film thickness.

4. Zone III: $T_h > 0,5$. This region is characterized by the formation of equi-axed three-dimensional grains. This high temperature growth mode in globular microstructure is made possible by the periodic interruption of crystal growth and successive renucleation in presence of a low concentration of impurities (<0,5%) [2].
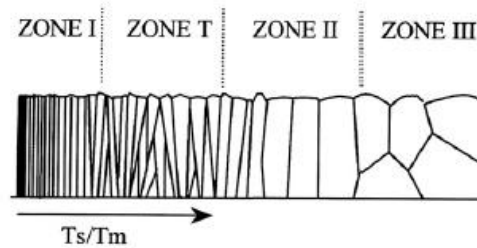

Figure 1.18   Schematic representation of microstructure morphology of PVD sputtered deposited thin film by SZD of Barna and Adamik [26].

This zone model is applicable to thin film deposited by DCMS, but it is no longer valid if HiPIMS is adopted, because of the high peak current and local temperature enhancement during the voltage impulses. This leads to the formulation of several novel structure zone diagrams, but the more general SZD has been proposed by Anders [27]: he developed the pre-existent model, maintaining the division in four zones, but representing the diagram in a three-dimensional axis system, in which it is possible also to include effects of ion etching (Figure 1.19).

The physical quantities reported in the three axes are representative of some features directly linked to the peculiarity of energetic deposition techniques.

The homologous temperature has been replaced by a generalized temperature, T^*, which is the sum between T_h and a potential term, T_{pot}, that account for the local temperature enhancement produced by the potential energy of impinging particles:

22

$$T^* = T_h + T_{pot} = T_h + \frac{E_{pot}}{kN_{moved}}, \qquad (1.22)$$

T_{pot} is the characteristic temperature affecting a heated region where N_{moved} atoms are subjected to rearrangement (k is the Boltzmann constant). E_{pot} is the potential energy of impinging particles, composed of a cohesive energy term, E_c, which describe the heat of sublimation, and a ionization energy term, E_i, reduced by the work function of electron needed for neutralization, ϕ:

$$E_{pot} = E_c + (E_i - \phi). \qquad (1.23)$$

E_c and E_i are between 1 and 9 eV/atom, and 4 and 10 eV/atom respectively, for the case of elementary metal films and singly charged ions; ϕ is about 4 eV for many materials [27].

The second axis is a logarithmic scale of normalized energy, E^*, describing displacement and heating effects caused by the kinetic energy of bombarding particles.

The kinetic energy of positive ions, E_{kin}, is expressed as the sum of the energy they possess in the plasma discharge, E_0, plus the energy they gained being accelerated at the cathode sheath:

$$E_{kin} = E_0 + QeV_{sheath}, \qquad (1.24)$$

Where Q is the ion charge state number, e is the elementary charge and V_{sheath} the voltage drop between plasma and substrate surface. The general discussion also applies to energetic neutrals and negative ions.

Finally, the third axis is the net film thickness, t^*. In the SZD, thickness decrease accounts for progressive densification, whereas negative thickness refers to the ion-etching sputtering mode.

It is interesting to note that, by choosing a logarithmic scale, the kinetic energy also represents the momentum through the relation $\log(mv^2/2) \propto 2\log(mv)$. Momentum is associated with atomic displacements cascades if the kinetic energy exceeds the bulk displacement energy, which is in the 12-40 eV range [27].

Non-penetrating ions may cause surface or bulk diffusion, enabling the rearrangement of atoms in such a way that no defects are incorporated and epitaxial growth is promoted.

On the contrary, penetrating particles may fast diffuse in the structure, and then thermalize in their growing site releasing energy in thermal vibration, that facilitate migration of interstitials inside the grains and adatoms on the surface. The driving force is the gradient of the chemical potential, leading to minimization of volume free energy and surface energy density, with contribution of interface and elastic strain energies, resulting in a preferred orientation growth of the film crystallites.

At high temperature, grains are enlarged because the increase of adatom mobility dominates over the increase in renucleation rate on defects induced by ion bombardment.

Finally, two non-accessible regions exist: one is at very low T^* and high E^*, because it is physically impossible to grow a film adopting elevated energies, but maintaining low surface temperature. The second non-accessible region exists for very low E^*, because ions from the plasma cannot be arbitrary slowed when approaching the surface.
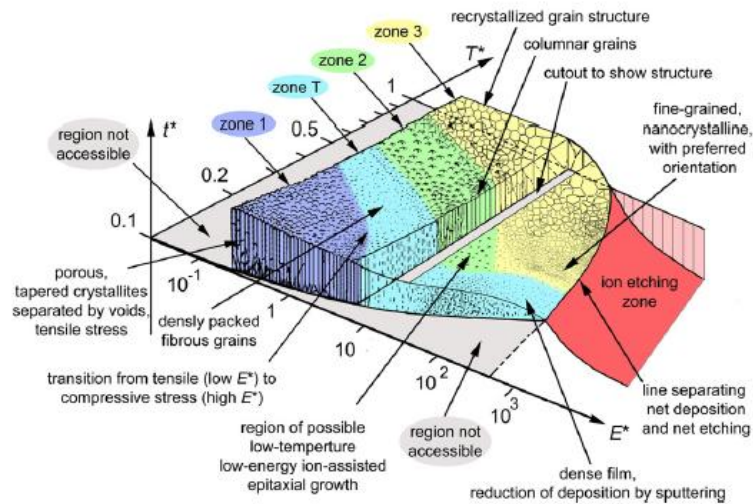
Figure 1.19   Representation of SZD by Anders model [27]. The diagram is applicable to energetic deposition such as HiPIMS.

It is worth noting that this SZD model for energetic deposition with high ion flux does not consider some more general aspects as differences between pure elemental film and compound films, phase separation and nanostructured films, existence of amorphous films at low temperature, etc. Thus it is important to consider SZD as qualitative representation of film microstructure evolution, bearing in mind that also other processes can actually affect the shape and the morphology of the deposited film, and consequently influence mechanical, as well as electrical or tribological properties of the coating.

2. *TiCN THIN FILMS DEPOSITED BY DC MAGNETRON SPUTTERING*

Protective coatings are of great interest for industrial applications to prevent tools deterioration under severe conditions, such as cutting, drilling or milling. Not only must they possess good mechanical properties, such as high hardness and toughness, resistance against oxidation and thermal stability, but also superior tribological properties, in order to prevent delamination or brittle fracture.

Improvements in hard coatings for tribological applications in components and tooling are achieved by surface engineering of a large variety of materials that possess low friction coefficient, still maintaining high hardness and optimal wear resistance.

In the past decades, titanium carbide and titanium nitride films has been extensively studied for their good tribological properties, but further improvements comes from TiCN coatings, which combines the advantages of the high hardness of TiC, and the good ductility and adhesion strength of TiN, achieving better comprehensive mechanical properties than single phase metal carbides or metal nitrides. [1,28,29]

The overall film properties are also affected by the deposition process. In literature, several different methodologies have been applied to TiCN coatings, and each method has its relative advantages considering certain applications. Lackner et al. [30] and Restello et al. [31] synthesized the TiCN films by pulsed laser deposition and magnetron sputtering/PECVD (Plasma Enhanced Chemical Vapor deposition) respectively. Arrando et al. [32] prepared the films using cathodic arc plasma deposition (CAPD), whereas Rie et al. [33] applied the Plasma assisted Chemical Vapor Deposition (CVD) and Metallic Organic Chemical Vapor Deposition (MOCVD).

In order to achieve a precise control of TiCN coating microstructure and chemical composition, it is of great importance the comprehension of the influence of the deposition parameters through a systematic characterization of surface properties.

In this chapter we will describe the general feature of TiCN coatings starting from its structure and possible deposition configurations obtainable with DC Magnetron sputtering (DCMS). Even if extensive studies exists on the effects of this deposition technique on TiCN films, and on the possible configurations adopted to improve its mechanical properties [34-37], no data are available on literature about the effects of deposition of TiCN by High Power Impulse Magnetron Sputtering. Therefore, the main purpose of this research work is to develop a HiPIMS deposition procedure that enables to produce adherent TiCN films in the best stability conditions, and to study how deposition parameters affect the overall coating properties. It will be demonstrated how, trough a simple monitoring of Optical Emission Signal (OES) of Titanium line (Ti$^+$ 499,1 nm) and Hydrogen line (H 656 nm), it can be obtained a deep and precise control over coating stoichiometry, and this finding open the possibility to microstructural and compositional coating design trough predictive parameters manipulation.

Moreover, we will investigate how HiPIMS reactive sputtering affect the overall coating features, comparing the results obtained with DCMS technique from the point of view of possible improvements and application on hard TiCN coatings.

A useful starting point for the comparison of the effects of the two deposition techniques is the existent literature on TiC coatings [38-40]: the deep understanding of microstructural evolution with deposition parameters of TiC phase [41,42] can be taken as a model for the comprehension of TiCN behavior.

In the successive paragraphs, a large variety of characterization techniques will be described as application to TiCN surface engineering.

2.1 General structure and properties

Titanium Carbon Nitride is a resistant ceramic coating with excellent adhesion, abrasion and mechanical properties. It is widely used in industrial tooling as protective coating thanks to its high hardness (3000 Hv –Vickers hardness or up to 37 GPa of nanohardness), thermal stability up to 400°C, and good wear resistance. Moreover, it can be deposited on a broad range of substrates, not only on metallic ones, but also on ceramics and plastics. Thanks to its good biocompatibility and non toxicity, it can be used also for medical surgical devices and food processing equipments.

It is by now accepted that TiCN posses a face centered cubic (fcc) NaCl type structure, belonging to the Fm-3m space group, similar to TiN and TiC structures [43]. More precisely, by virtue of the perfect solubility of TiC and TiN predicted by their combined phase diagram [43, 44], it is possible to describe TiCN formation by a substitution mechanism of C atoms in N sites of a TiN ordered lattice [43] (Figure 2.1). In fact, N is more electronegative and needs less Gibbs free energy to react with Ti compared with C [45], so TiN particles are more likely formed, and C is incorporated in the structure with substitution mechanism.
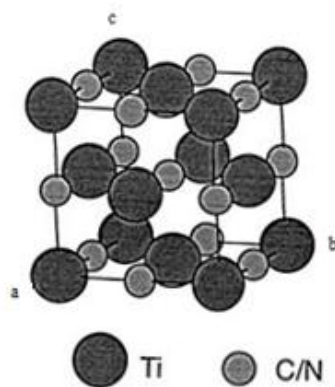

Figure 2.1   Representation of fcc structure of TiCN, in which C and N randomly occupy the (½ ½ ½) sites.[43]

Carbon content has a significant influence on the properties and microstructure of titanium carbonitrides, starting from the strength of atoms bonding that directly affect the value of lattice parameter. Stoichiometric TiN and TiC lattice parameters are respectively 4,2417Å and 4,3247Å, as reported in (Figure 2.2). We can note that TiCN lattice parameter is always comprised between TiN and TiC values, as demonstrated in the case of $TiC_{0.2}N_{0.8}$ and $TiC_{0.7}N_{0.3}$. This is explained if considering that C possesses a greater atomic radius than N, so the substitution with a bigger atom implies higher electronic interaction and thus matrix relaxation, as predicted by Vegard's rule.

It is reported in literature that the lattice parameters measured on TiCN thin films have the tendency to be higher than in bulk materials. This fact is explained by several reasons: differences in thermal expansion coefficient between film and substrate, incorporation of impurities (such as Oxygen) or incorporation of either C and N atoms as a consequence of a non equilibrium deposition process; moreover, this lattice expansion can be attributed to the presence of internal stress, generated by a high density of grains boundaries and structure defects [44].

Lattice parameters vary between 4,2344 Å and 4,2971 Å for bulk $TiC_{0.3}N_{0.7}$, and $TiC_{0.7}N_{0.3}$ respectively, whereas for magnetron sputtered coatings from 4,29 Å to 4,32Å [46].
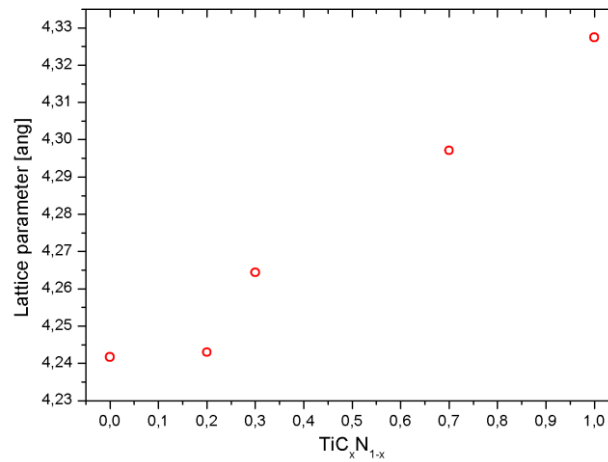

Figure 2.2   Evolution of bulk lattice parameter of TiCxN1-x from TiN to TiC. (From PDF standards #00-038-1420, #01-076-2484, #00-042-1488, #00-042-1489, #00-032-1383, respectively)

2.2 **Structural design and effects of deposition parameters**

Nano- and micro-structural design combined with suitable compositional adjustments (variation of C/N ratio and Ti content), enable the construction of a wide variety of TiCN coatings with tailored characteristics. In particular, four different structures can be obtained varying the deposition parameters:

1. Monolayer structure: is the basic coating configuration, in which the composition is maintained constant throughout all the film thickness.[31, 36, 46]
2. Multilayer structure, made of a succession of TiN/TiCN layers. The overall properties depends on film thickness and periodicity of the multilayers.[35,47,48].
3. Graded structure, in which the composition in continuously varied for all film thickness in order to favor a better adhesion to the substrate [36].
4. Nanocrystalline film embedded in an amorphous a-C matrix. They are a direct evolution of a monolayer structure in which the cristallinity is progressively lost due to the introduction of a large amount of carbon that form the a-C matrix, and that is expected to positively affect the mechanical properties [37,49].

All of these structures possess positive and negative features. It is thus convenient to decide the design of the coating in function of the final application that is required, and on the feasibility of the deposition process control. In the following an overview of the different deposition strategies found in literature will be given, with reference to the effects obtained on the structure and composition of the final TiCN films.

The starting deposition parameters have a key role in the determination of chemical and structural features of the film. It is of common practice to effectuate, prior to deposition, a sputter etching treatment of both the target and the substrate in Ar^+ atmosphere, in order to eliminate possible impurities adsorbed on the surface, and to completely remove poisoning layers on the target which have been deposited in previous treatments. It is indeed of fundamental importance that the solid target is always in a prefect metallic state prior to deposition, in order to make the process perfectly reproducible.

To enhance adhesion to the substrate, a thin Ti layer is first deposited [46], followed sometimes by a second thin TiN layer [31] that can ameliorate wearing performances, preventing delamination.

In this phase, the substrate holder can be heated to a given temperature in order to favor adatom mobility and the formation of a more ordered, compact structure [36,46].

Senna et al. [46,50], focus their attention on the effects that the application of a voltage bias to the substrate has on the chemical composition of TiCN films deposited by magnetron sputtering ion plating technique and a mixture of two reactive gas (N_2 and CH_4). They pointed out that the major effect of applying a bias to the substrate is to decrease carbon and nitrogen incorporation, as a consequence of a resputtering process (Figure 2.3), whereas changing the ratio of reactive gases, CH_4/N_2, lead to the formation of films with different stoichiometry, and in particular over- stoichiometric coatings are produced for CH_4 contents superior of 30 vol%.
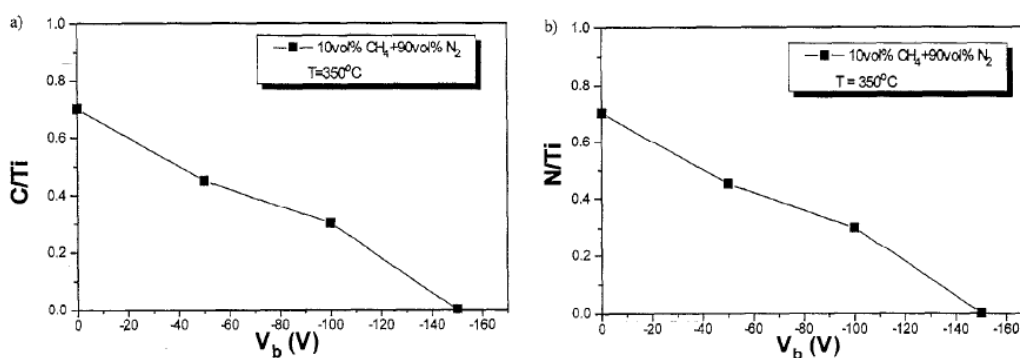

Figure 2.3   Influence of substrate bias on the incorporation of carbon (a) and nitrogen (b) in TiCN coating [46].

The effects of nitrogen flux and of optical emission set point (OE) of Ti atoms, that is a fixed percentage of the intensity of the optical signal coming from an excited gaseous Ti atom sputtered from a perfectly metallic target, have been investigated by Restello et al. [31], who pointed out the dominant role of this last parameter on the control of chemical composition. This technique is based on the monitoring of optical emission signal of Ti^+ line, employing a spectroscope in the visible range. The desired set point is reached through the variation of reactive gas fluxes in the deposition chamber.

The coatings have been deposited by reactive magnetron sputtering ion plating, with four Ti target and a mixture of N_2 and C_2H_2 reactive gases. The sample holder wad biased to 500W RF, leading to a DC self bias between 30 and 60V. By controlling the OE set point and the nitrogen flow, it is possible to choose the composition across different regions in the Ti-C-N ternary diagram (Figure 2.4): the C/N ratio is determined primarily by the nitrogen flow, and only by a limited extent by the OE set point, which, on the contrary, is responsible for the global Ti incorporation in the growing film.

As it can be seen from (Figure 2.4), stoichiometric TiC_xN_{1-x} films, as well as TiC and TiN, can be obtained setting the OE set point to the 60% of the initial intensity value. Decreasing this parameter leads to the formation of over-stoichiometric coatings.

Moreover, studying the composition of the deposited films in function of their position in the chamber and relative to the Ti targets, Restello et al. demonstrate that the deposition process is indeed an hybrid magnetron sputtering/plasma enhanced CVD process. Reactive gases behave differently: N_2 is demonstrated to react with Ti target, and its content is strictly linked to the

28

sputtering process; C_2H_2 on the contrary, is principally deposited from its gaseous phase, and only in a limited extent it reacts with the solid target.
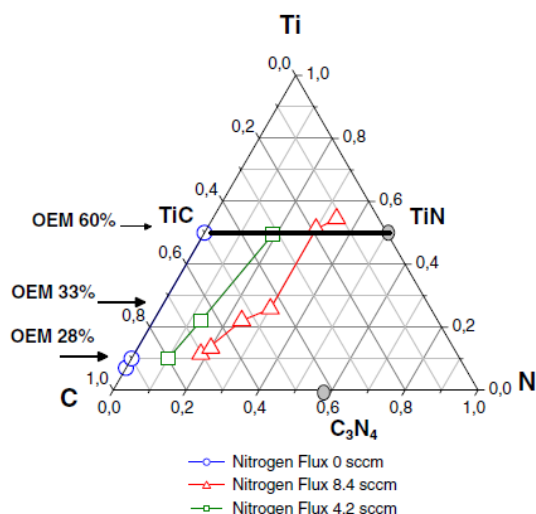

Figure 2.4   Ternary diagram of Ti, C and N contents as a function of optical emission set point and nitrogen flux [31].

Carbon content in the film can be raised by increasing the flux of the reactive gas in the deposition chamber (C_2H_2 or CH_4) [45], or also, if employing solid graphite target, by increasing the current applied [48]: in this last case, the intensity of target current acts directly on the quantity of sputtered material.

Another way of microstructural design is, as mentioned before, the realization of different film structures, in which the particular configuration adopted is sought for an enhancing of some specific aspects, like film adhesion or tribological performances.

Closed field unbalanced magnetron sputter ion plating is an extremely versatile physical vapor deposition technique employed to produce dense, well adherent coatings, and can be easily adjusted for the deposition of a multilayer or graded structure. These can be obtained by the control of reactive gas fluxes, and by the time they are pumped in the deposition chamber [36,47]. In a multilayer configuration some graded transition regions are always obtained, as an abrupt variation of the reactive gas fluxes would worsen adhesion properties.

2.3   Compositional characterization techniques

We have outlined in the previous paragraph how deposition parameters affect the overall composition of the deposited film. We now describe the main techniques adopted for film compositional analysis, and report how they have been exploited to study TiCN film properties.

Chemical and physical characterization of solid state samples is commonly made with the aid of microscopy and spectroscopy techniques. They are both based on the interaction of an external excitation with matter, that can be either visible or X ray photons, or charged electron or ion beams.

When an electron probe is adopted, Rutherford backscattered (RBS) electrons as well as X-ray characteristic radiation can be collected in order to obtain compositional information. Energy dispersive X-ray spectroscopy (EDS) and wavelength dispersive spectroscopy (WDS), are commonly adopted for a straightforward quantitative estimation of the coating's components [45,51].

The chemical composition of the film as well as the nature of the bonding present in the TiCN structure can be studied also by means of X-ray photoelectron spectroscopy (XPS). With this technique, several authors [35,45,47] pointed out in a deposited TiCN film the simultaneous presence of four different molecular structures: primarily Ti(C,N), but also TiN, TiC, and some amorphous carbon with a sp^2- and sp^3- type C-C bonding. This finding is essential for the comprehension of the microstructural evolution in function of the total carbon content in the coating, which will be described more extensively in the next paragraph.

In order to control the distribution of the constituents throughout the film thickness, Yang et al. [36] employed Secondary Ion Mass Spectrometry (SIMS), a powerful, yet destructive, technique that enables a fine depth profile analysis on thin film samples with a high spatial resolution.

SIMS technology has been applied also by some research groups [52-54], to a quantitative depth profiling of hard and wear resistant coatings with composition metal-C:N:O:H:Ar. They modified a pre-existent analysis based on the so-called Relative Sensitivity Factor (RSF) [55] and demonstrate that, for Ti-N-C-O coatings with O concentration up to 43 at%, it is possible to determine the concentration of the different constituents with a deviation from the starting known values (typically Electron Probe Micro Analysis – EPMA values) that doesn't exceed 15%. This approach requires the collection of MCs^+ secondary molecular ions (M stands for the element of interest) from an incident Cs^+ primary ion beam, in order to minimize matrix effects[1]. In fact, the environment and the bonding formed by a specific element directly influence its ionization probability.

The modified linear relationship between signal intensities I and concentrations c (in at.%) is:

$$\frac{I_{MCs^+}}{I_{TiCs^+}} = RSF_{M/Ti} \frac{c_M}{c_{Ti}}$$

(2.1)

where the RSF must be derived from suitable standards of known composition for all the elements of interest.

However, the linear relation in (2.1) is no more valid when O concentration exceeds 43%, because a significant deviation from linearity is observed due to the drastically increase of OCs^+ yield [52].

2.4 Microstructural characterization techniques

In order to achieve a complete understanding of the influence of the deposition method, experimental conditions and set-up characteristics on the thin film structure, a wide range of characterization techniques are currently available. Mostly, they can give information about one general aspect looking from different perspectives, but from a global analysis it is possible to understand the deep connections between structural, mechanical and tribological properties.

---

[1] Matrix effect is the variation of the sputtering yield of a specific element in function of the particular matrix in which it is embedded, and is due to the differences in bond strength between different atoms.

2.4.1 Electron Microscopy

A first straightforward method of investigation of the coating's morphology is microscope imaging using an electron probe, that can be exploited both in reflection mode, with Scanning Electron Microscopy (SEM), or in transmission geometry, with Trasmission Electron Microscopy (TEM), and is based on the collection of secondary electrons or backscattered electron signals.

Several authors observed from SEM images of fractured cross-section, that TiCN samples deposited in a graded or monolayer configuration possess a dense columnar structure, with most of grains extending from the interface to the substrate (Figure 2.5a) [36,44,46]. This ordered structure is found also in a multilayer configuration in the uppermost and thicker TiCN layer or in internal TiN, whereas in the inner TiCN layers, where minor energy stress is stored, a more featureless and smooth structure is preferably formed (Figure 2.5b) [35,47].
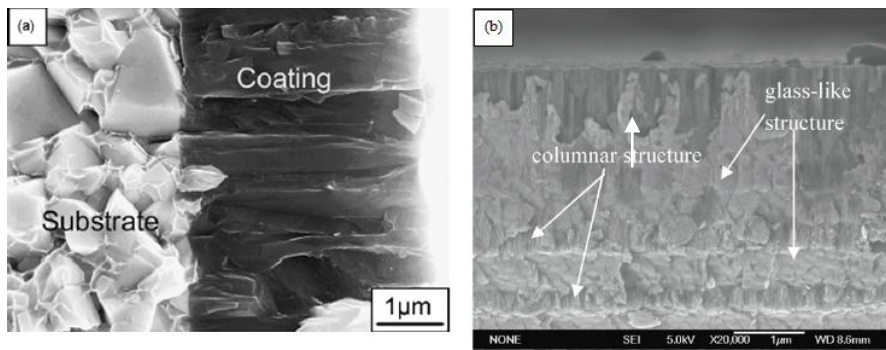

Figure 2.5   Cross-sectional SEM images of (a) homogeneous TiCN coating with a dense columnar structure [36] and (b) multilayer TiN/TiCN coating with both columnar and glass-like structures [35].

Also the deposition method deeply influence the coating's structure: Samulesson et al [38] compared TiC/a-C:H films with the same C/Ti ratio and similar deposition rate, deposited by DCMS and by HIPIMS. From cross sectional SEM images (Figure 2.6) they showed that the coatings deposited by DC magnetron sputtering exhibits a rough surface and a porous, columnar microstructure, whereas the corresponding HiPIMS samples present a smoother surface and a denser structure throughout the film thickness. This is true in general for samples deposited by HiPIMS, due to the high-ion energy bombardment that favors the growth of densely packed atomic planes.
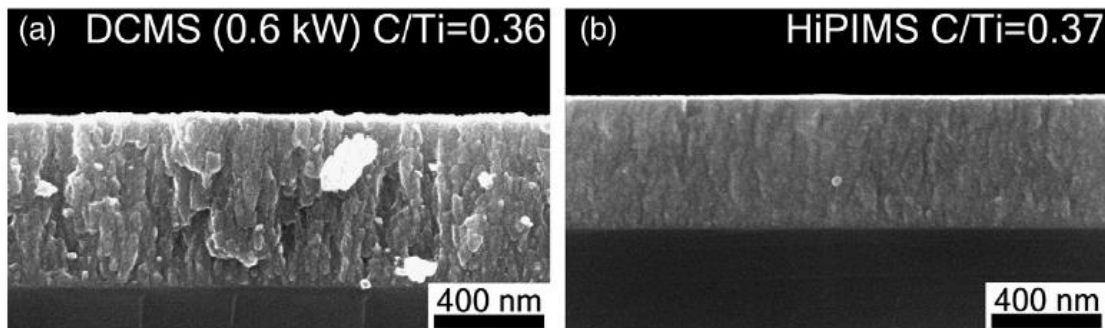

Figure 2.6   SEM cross-sectional images of TiC/a-C:H films with similar C/Ti ratio, deposited with similar deposition rate by (a) DCMS and (b) HiPIMS. [38].

2.4.2 Combined XRD analysis

A powerful method for the characterization of crystalline state is X-ray diffraction (XRD) [56]. All XRD patterns reported in literature confirm that the coatings are primarily polycrystalline and possess a cubic B1-NaCl structure, with the characteristic visible diffraction peaks in the 2θ region from 30° to 80° corresponding to (111), (200), (220) and (311) reflections (Figure 2.6).

As reported in paragraph (2.1) the lattice parameter increases upon C incorporation, which can be obtained, as described in paragraph (2.2), by acting on deposition parameters such as reactive gas fluxes [35] or current on the carbon target [48]. As a consequence, the position of the diffraction peaks is found to shift towards lower diffraction angles with the increasing of the carbon content because of the relation with planar interspacing d_{hkl} established by Bragg's law (2.2):

$$2d_{hkl} \sin \theta = n\lambda, \qquad (2.2)$$

where n is the order of the reflection and λ the irradiation wavelength.

However, as it will be pointed out below, the presence of macroscopic stress may also shift the position of the diffraction peaks. In order to properly determine the lattice parameter, a more complicated analysis is necessary.
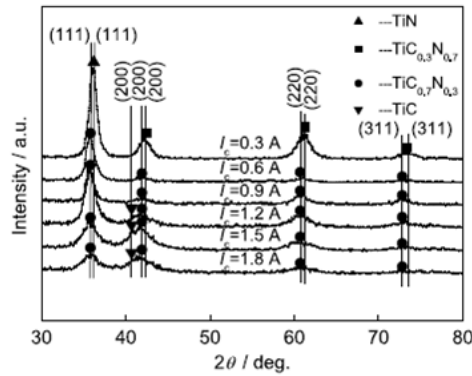

Figure 2.7   XRD diffraction spectrum of TiCN. It is clearly visible the shift towards lower Bragg's angles with increasing C incorporation in the crystalline structure [48]

If the positions of the diffraction peaks give important information about the C content of the coating, line broadening is a reference parameter to calculate mean dimension of diffracting crystallites and internal microstrain. In fact, an ideal diffraction spectrum of a perfect crystalline sample would have a δ-Dirac shape, but the finite size effect of crystallites give rise to the first contribution to line broadening $\Delta(2\theta)$, described by Sherrer's equation:

$$\Delta(2\theta) = \frac{K\lambda}{T \cos \theta} \qquad (2.3)$$

where K is the Sherrer dimensionless constant ($K \approx 0,9$), T the mean crystallite size dimension and $\Delta\theta$ and θ are the angular width and position of a given Bragg peak in a diffractogram. Thus with decreasing the grain size, line broadening would progressively raise.

Many studies on crystallite dimension evolution show a clear dependence on the amount of C content in the coating [31,47,48]: the general interpretation is that the higher the C/N ratio of the growing film, the more the C atoms would decrease the atomic diffusivity on the coating surface during the deposition [48]. Consequently, the columnar structure would gradually disappear, in favor of the appearance of a nanocrystalline phase, with size smaller than 5nm, embedded in an amorphous matrix. This evolution is supported by TEM images [48], as well as

by XPS measurements [35,47], and by the clear diminution of X-ray diffraction peak intensity with decreasing the O.E. set point [31].

No systematic studied has been carried yet on TiCN compounds, and a mathematical model of the evolution of crystal structure is still lacking. Nevertheless, microstructural evolution in carbide-based coatings as a function of increasing total carbon content (Figure 2.8Figure 2.8) can, however, be taken as a model for TiCN compounds, thanks to the high solubility of nitrogen in TiC phases, that makes C and N nearly interchangeable. The evolution trend of different TiC_x phases and grain size with the total carbon concentration are reported in (Figure 2.9a) and (Figure 2.9b). It is clearly visible how, for over-stoichiometric samples, nanocrystals have dimensions below 5nm, and a considerably increase of a-C(:H) phase is recorded. A similar trend is expected also for TiCN coatings.
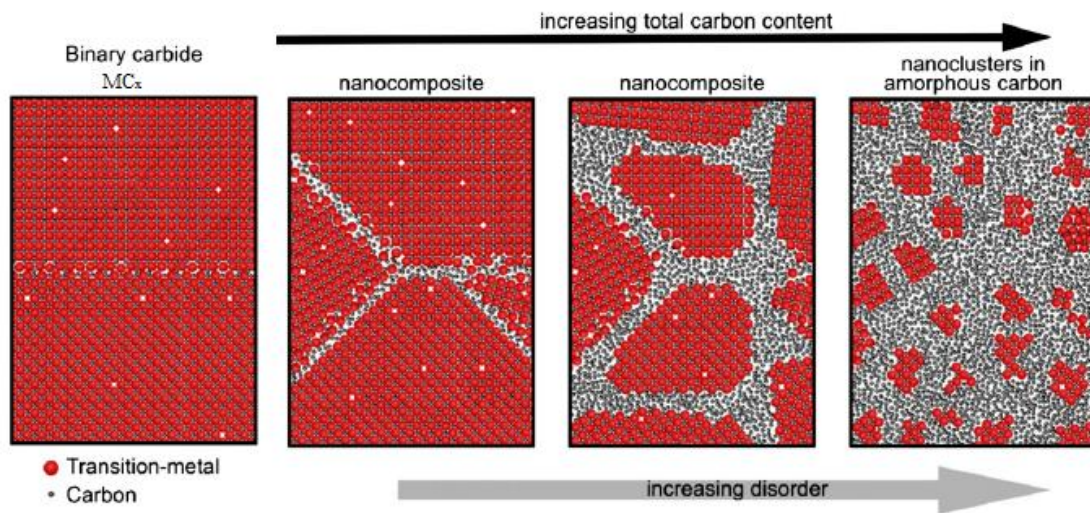

Figure 2.8   Schematic illustration of microstructural evolution in sputter-deposited transition-metal-C coatings with increasing C content [41].
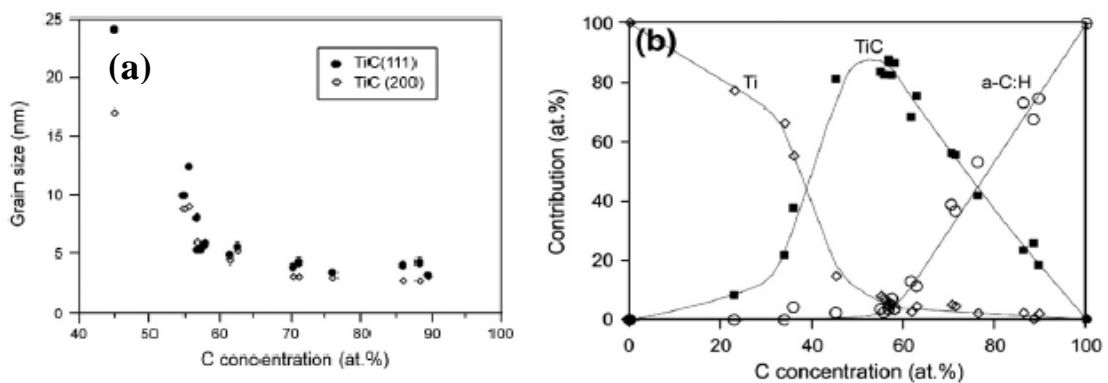
Figure 2.9   Evolution of TiC_x grain size with carbon concentration and (b) relative amount of different phases present in the coating. [41]

As well illustrated in (Figure 2.8Figure 2.8), the grain size of the nc-MC_x crystallites decreases as the total carbon content increases, and this trend can be explained by the agglomeration of C atoms at grains boundaries, which hinders grain growth. At first, the microstructure is still columnar, but it will progressively lose its ordered feature in favor of a nanocrystalline TiC_x phase embedded in an amorphous matrix formed by the C in excess.

The structure of this a-C matrix is strongly influenced by the deposition process and parameters: it has been pointed out [57] that an sp^2-bonded a-C phase is primarily obtained for

non reactive sputtering, while, when using hydrocarbon gases, an amorphous phase with higher H incorporation (a-C:H) and more sp^3 – type bonds is obtained.

Another feature of nanocomposite (nc) systems that will have a significant influence on the properties of the material is the interaction between nanocrystal's surface and the surrounding matrix phase. A model involving charge transfer between the two phases has been proposed by Lewin et al. [42], based on the observations of lattice expansion of nc-TiC$_x$/a-C samples.

From XRD measurements, Lewin et al pointed out a correlation between expansion of TiC$_x$ lattice parameter and the progressive diminution of grain size (open markers in Figure 2.10). They proposed a possible explanation based on an interface charge transfer phenomenon from the carbide phase to the more electronegative carbon matrix. As the grain size decrease, the electron deficiency per Ti atom in the grain increase, and hence gradually weakens the Ti-C bond, leading to an increased atom distance and hence an increased lattice parameter.

The presence of additional interface states has been confirmed by XPS analysis, and theoretical *ab initio* simulations based on the model they proposed well agree with experimental data (filled dots in Figure 2.10).

The authors suggest that this approach can be extended also to other types of nanocomposites, and it would be interesting to verify if it is applicable also to TiCN.
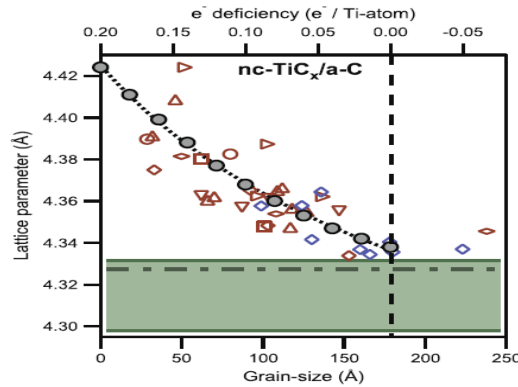

Figure 2.10   Correlation between lattice parameter and grain size observed in nc-TiC$_x$/a-C(:H) nanocomposites coatings. Open markers are experimental data and refer to the bottom axis; filled markers are from ab initio simulations and refer to the top axis. Green area shows expected range of lattice parameter from bulk TiC$_x$. [42].

Besides size effects, also distortion and random variation of the interplanar spacing may affect the diffraction peak widths. In order to properly separate this contribution from size broadening, it is necessary to properly model the dependence of these two contribution on the diffraction conditions and to perform a combined analysis of X – ray spectra in which several diffractograms are analyzed at once.

The elastic strain can be expressed as a function of the position X in the sample of one particular crystalline grain:

$$\varepsilon(X) = \varepsilon^I + \varepsilon^{II}(X) + \varepsilon^{III}(X),\tag{2.4}$$

ε^I is the global macroscopic strain generated by the macrostress σ^I, whereas elastic, thermal or plastic anisotropy are responsible for the second order mesostrain, $\varepsilon^{II}(X)$, which describe the deviation from the global macrostrain value for each given grain. Finally, the third order microstrain, $\varepsilon^{III}(X)$, is the position dependent fluctuation from the average grain's macrostrain, that is dependent on three main parameters: film compactness, crystal size and presence of a second phase.

34

Often, deposited TiCN films are stressed along one or more axis, due to the effect of the substrate or because of the energy released in the deposition process. This stress is responsible for the ε^I term in the expansion (2.4). In the case of isotropic polycrystalline samples, the macrostress can be related by standard elasticity theory to the strain state, which can be experimentally measured trough the so-called $\sin^2\psi$ method. This is in general a tensor relation that describes the variation of the diffraction peak position in function of the tilting angles around one sample's surface axis (the colatitudes angle ψ) or the sample surface normal (the azimuthal ϕ). This method account for the tensorial and directional nature of strain $\varepsilon_{\phi\psi}$, normal and shear stresses, σ_ϕ , τ_ϕ , with the only hypothesis that the stress in direction normal to the sample surface must be zero, $\sigma_{33}= 0$:

$$\varepsilon_{\varphi\psi} = \frac{1}{2} S_2 (\sigma_\varphi \sin^2 \psi + \tau_\phi \sin 2\psi) + S_1 (\sigma_{11} + \sigma_{22}) \qquad (2.5)$$

.

$$\frac{1}{2} S_2 = \frac{(1+\nu)}{E}, \quad and \quad S_1 = -\frac{\nu}{E}$$

E is the elastic Young Modulus and ν the Poisson's ratio of the material. All these quantities will be more precisely defined in the next paragraph, when dealing about mechanical properties.

In the simplest case of uniaxial stress state, when the shear stresses are negligible ($\tau_\phi = 0$) and when in-plane stresses are isotropic ($\sigma = \sigma_{11} = \sigma_{22} = \sigma_\phi$), eq. (2.7) simplifies to:

$$\ln\left(\frac{1}{\sin \vartheta_{hkl}}\right) = \frac{1}{2} S_2 (\sigma \sin^2 \psi) + 2S_1\sigma + \ln\left(\frac{1}{\sin \vartheta_0}\right) \qquad (2.6)$$

where θ_0 is the unstrained position of the sample's diffraction peak under investigation.

In literature, TiCN coatings has been reported to posses compressive macrostress [44], as evidenced in (Figure 2.11) by the diminution in the calculated lattice parameter for each (hkl) reflection the closer is the ψ tilting angle to 90° (i.e. reflecting (hkl) planes perpendicular to sample surface).
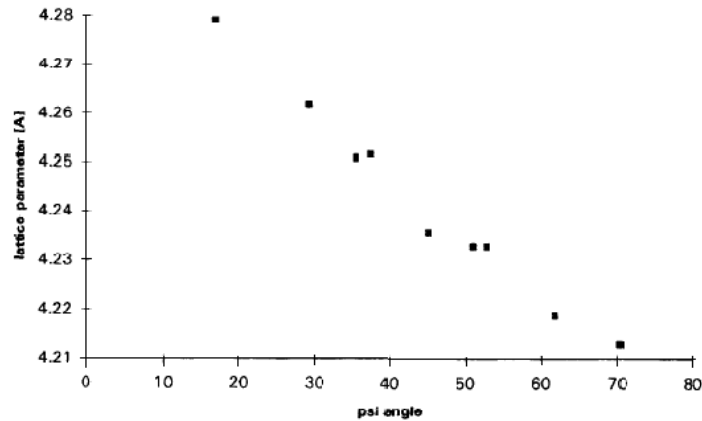
Figure 2.11   Variations of lattice parameters of a particular (hkl) reflection as a function of ψ tilting angle, demonstrating a compressive stress state. TiCN coatings has been magnetron sputtered deposited on stainless steel. [44]

For stoichiometric TiCN coating, with a good crystallinity and bigger, less deformable crystals, microstrain is expected to take very low values, but an increase with C content is observed due to localized strain gradient caused by both substitutionally bonded and interstitially bonded carbon atoms in the TiN lattice [44].

On the other hand, the presence of an amorphous phase is expected to act as a source of deformation of the crystallites, thus producing a higher internal microstrain [58].

One last interesting feature of TiCN coatings derived from XRD analysis is a profound (111) preferred orientation, as reported by several authors [31,36,44,47] independently of the film's structure (monolayer, graded or multilayer).

(111) plane is the most densely packed and exhibits the lowest surface energy, and is thus expected to survive at the expense of fast growing planes. This texture character is strong in crystalline samples, but became less dominant with the loss of nanocolumnar order.

An immediate fingerprint of the presence of texture is given by the intensity of the peaks of the diffraction patterns, which do not match with calculated intensity values. A first, straightforward evaluation of the presence of preferential orientation can be done by comparing the observed intensity values with those expected from a non-textured reference standard. The Texture Coefficient (TC), defined as [45], is a simple measure of the degree of preferential orientation:

$$TC(hkl) = \frac{n\,I_{hkl}/I^0_{hkl}}{\sum_{hkl} I_{hkl}/I^0_{hkl}} \qquad (2.7)$$

where n is the total number of reflection observed, I_{hkl} is the measured peak intensity of a given *(hkl)* Bragg reflection, which is compared with the intensity I^0_{hkl} of a standard sample of the same phase. Any deviation of TC from unity indicates the presence of a more or less pronounced preferential orientation in the coating.

In order to deeply investigate the texture behavior of a crystalline sample, several diffraction measurements in a θ-2θ configuration, and for several (ψ,φ) positions, are needed.

Successively, these spectra must be analyzed by an appropriate software, in which are implemented the basic algorithm of diffraction spectrum modeling, like the Rietveld method, together with a complete texture analysis method [56].

2.4.3   Raman spectroscopy

Since no information on the amorphous component can be obtained from diffraction techniques, alternative techniques are needed. Raman spectroscopy is a valid tool to investigate the nature and features of atomic bonding present in the matrix surrounding nanocomposite phases.

This technique is based on the Raman inelastic scattering of monochromatic light by phonons, and is detectable as a shift in the collected scattered wavelength due to the interaction with the vibrational modes of the lattice and/or molecular bonding.

A necessary condition to observe Raman scattering is that the polarization *P* of the electronic clouds, and conversely the sample susceptibility χ, is somehow changed by a phononic deformation of the crystal lattice:

$$\chi(k) = \chi_0 + \frac{d\chi}{dq}Q(k,q) \qquad (2.8)$$

where Q is the amplitude of a phonon of wave vector q.

The periodic modulation of *P* by the phonon oscillation frequency *ω(q)* thus leads to the emission of a scattered wave with Stokes or Anti-Stokes character: *ω₀±ω(q)*.

In TiCN samples, the amorphous matrix can be formed both by C-C and C-N bonding, but the great amount is considered to be simply of amorphous carbon type. Ferrari et al. [59] point out that a key parameter for the description of a general carbon system is its sp^2 (graphite-like) to sp^3 (diamond-like) bond fraction, as summarized by the ternary phase diagram in (Figure 2.12): they distinguish various degrees of graphitic ordering, that range from microcrystalline to

glassy carbon; a third contribution comes from the presence of hydrogen, which could be included in the structure, during the process of deposition, up to 60 at. %.
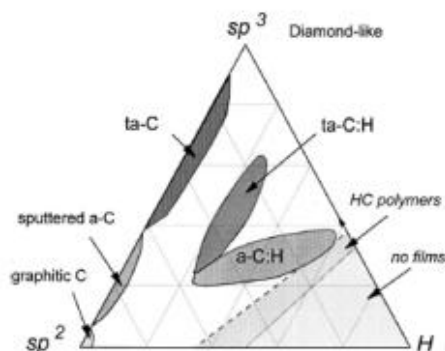

Figure 2.12   Ternary phase diagram of amorphous carbons. The three corners correspond to diamond, graphite and hydrocarbons respectively [59].

The main factors that determine Raman spectrum shape are:

1. Clustering of sp^2 phase
2. Bond disorder
3. Presence of sp^2 in rings or chains
4. sp^2/sp^3 ratio

and will be detailed in the following.

The structural difference between sp^3 and sp^2 sites is that the former are formed only by σ bonds, whereas the latter possesses both σ and π states and could be present in both rings and chains. The scattering from sp^2 sites dominate the Raman spectra of all a-Cs, producing a characteristic double peak trend in the 800-2000 cm^{-1} region.

The first Raman peak is called Graphitic (G) because it is the only mode allowed in a single crystal of graphite. It lies at a frequency of 1580-1600 cm^{-1} and is caused by a bond stretching mode of E_{2g} symmetry of all pairs of sp^2 atoms in both rings or chains (Figure 2.13a).

The introduction of defects in the crystal structure leads to a second Raman mode at ~1360 cm^{-1} called D (Disordered), typical of those sp^2 sites only in rings not in chains, and described as an A_{1g} symmetry breathing mode (Figure 2.13b).

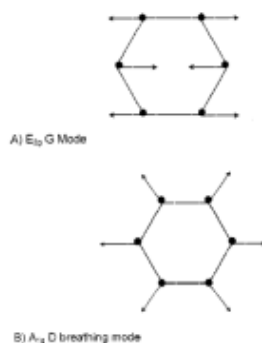*Figure 2.13   Carbon motion in the (A) G and (B) D vibrational mode. [59]*

Ferrari and coworkers. [59] found that, it is possible to classify Raman spectra of all carbon systems in a three stage model of increasing disorder. Moreover, it is applicable also to hydrogenated systems, because it has been found that C-H mode give no detectable contribution to G and D peaks. These three stages, shown in (Figure 2.14), are:

1. From perfect graphite to nanocrystalline graphite
2. From nanocrystalline graphite to a-C
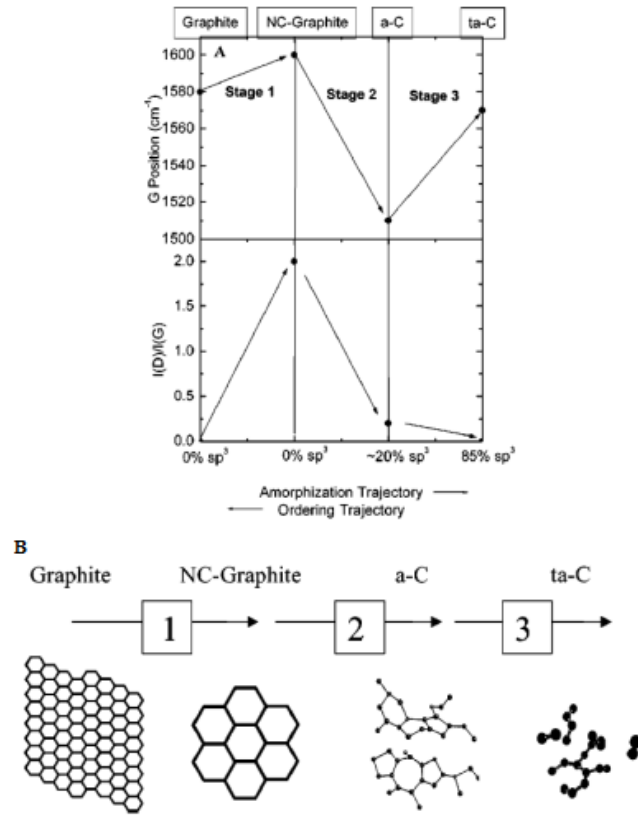3. From a-C to ta-C (tetrahedral amorphous carbon).

Figure 2.14   (A) Schematic representation of the three stage model for carbon systems through the variation of the I(D)/I(G) ratio. (B) shows the variations in sp^2 configuration during the amorphization trajectory [60]

From a study of G and D peaks features it is possible to obtain information on the crystal structure. Tuinstra and Koenig proposed a first relation between the intensity ratio I(D)/I(G) and the in-plane correlation length L_a or cluster diameter:

$$\frac{I(D)}{I(G)} = \frac{c(\lambda)}{L_a},$$

(2.9)

where $c(\lambda=515,5\ nm) \sim 44\text{Å}$ [59]. This relation has been verified up to $L_a \sim 20$ Å. It is worth noting that this crystallite dimension is underestimated in comparison to the ones obtained by a XRD analysis, because Tuinstra - Koenig (TK) equation (2.9) assumes that graphite becomes uniformly nanocrystalline, whereas X-ray diffraction weights more the dispersion in crystallites dimensions.

When the size of a cluster diameter is below 2 nm, the TK equation is no longer valid and must be replaced by a new relation, proposed by Ferrari et al. [59]:

$$\frac{I(D)}{I(G)} = c'(\lambda)L_a^2$$

(2.10)

where $c'(\lambda=514nm) \approx 0{,}0055$. The general trend of (2.9) and (2.10) is summarized in (Figure 2.15).
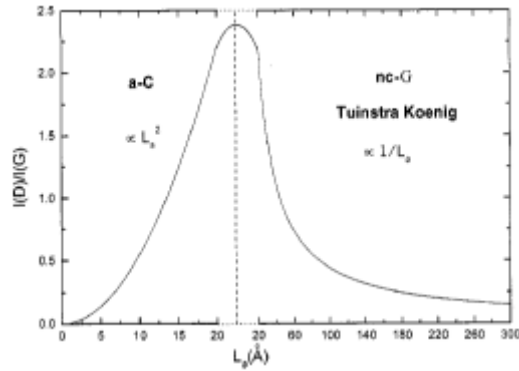
Figure 2.15   Variation of the I(D)/I(G) ratio from Ferrari and TK relation [59].

In the **first amorphization stage,** we attend a progressive reduction of grain size of ordered graphitic layers, still keeping aromatic rings and purely sp^2 bonds. This produces a raising raise in D contribution as the crystallite dimension L_a decrease, following the TK relationship. It is also observed an up-shift of G peak position from 1580 to ~1600 cm^{-1} , but the G mode still remain not dispersive (no peak shift with photon excitation energy) because in this mode it is maintained a perfect order in sp^2 aromatic rings.

Stage 2 is characterized by a progressive decrease of L_a below 2 nm, for which TK equation is no longer valid. The introduction of more defects leads to a distortion of six-fold rings, whereas sp^2 chains are kept intact; $I(D)/I(G) \propto L_a^2 \propto M$ falls gradually to zero with the number *M* of ordered rings.

G peak decrease from 1600 to ~1510 cm^{-1}, at the end of stage two, the structure is almost fully sp^2–bonded a-C consisted of distorted rings, with a maximum concentration of sp^3 bonds up to 20%.

In **stage 3**, the sp^3 content rise from 20% to ~85%, while sp^2 rings gradually transform into olefinic C=C bonds. Being shorter than aromatic sp^2 bonds, they induce G peak shift towards higher vibration frequencies (~1640 cm^{-1}). At the same time D peak almost disappears, leading to *I(D)/I(G)~0.*

The presence of hydrogen in the system slightly change the overall considerations, because visible Raman spectrum is not affected by the presence of C-H modes: the stretching mode lies above 3000 cm^{-1} whereas the ones that lie in the D region are not resonantly enhanced, and so they can be neglected.

C-H modes could become detectable at much higher photon energy, such as in UV Raman spectroscopy.

The main effect of H incorporation in the structure is that H tends to saturate C=C bonds as $\equiv CH_x$ groups, rather than increasing the fraction of C-C bonds. So, in a-C:H system there is a different C-C network compared to a-C of similar sp^3 content and, in general, with increasing the H content there is a reduction of sp^2 cluster size and a parallel enhancement of the band gap.

The Raman spectra of carbon nitrides measured at any excitation energy have a similar form to those of N-free amorphous carbons in the 1000-2000 cm^{-1} region: the chain-like CN molecules have an expected vibrational mode between 1500-1600 cm^{-1}, whereas ring-like molecules between 1300-1600 cm^{-1}, so the behavior in the D-G region of C and N atoms is very similar. Moreover, N tends to promote more clustered sp^2 bonding, inducing a delocalization of

vibrational modes over both C and N sites, which make really hard the determination of the type and quantity of nitrogen bonds from Raman spectra.

The action of this additional element in sputtered carbon nitrides is now to introduce disorder in sp^2 sites through cross-linking between adjacent planes, but still maintaining a low sp^3 fraction. This enhances hardness and elastic recovery of such materials.
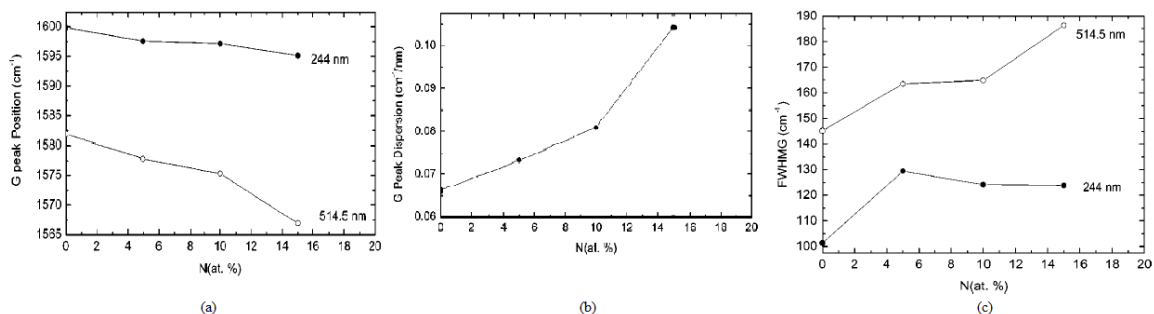

Figure 2.16   Evolution with increasing N content of (a) G peak position, (b) G peak dispersion and (c) G FWHM for a-C:N films.[60]

A measured TiCN Raman spectrum is displayed in (Figure 2.17). The D and G peak are clearly visible, confirming the presence of an amorphous a-C(-N) phase typical of Stage 2, when looking at I(D)/I(G) and G peak position [35,37]. Moreover, four additionally peaks, at 242, 352, 535 and 606 cm^{-1} are evident: this Raman signal is attributed to acoustic and optical vibrational modes of titanium nitrite/carbide respectively that, accordingly also to other studies, should be located between TiC and TiN bands, as reported also by other works [61,62].
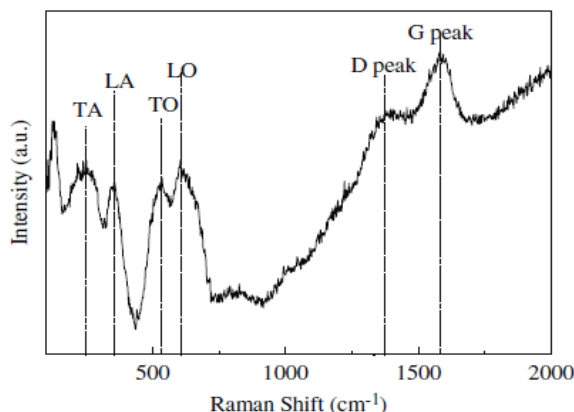
Figure 2.17   Raman spectrum of the TiN/TiCN multilayer film [35].

In general, a three stage model similar to the one of carbon systems can be applied to carbon nitrides, without need of extra peaks due to CN, NN or NH modes [60].

It is possible to classify the bonding in carbon nitrides films in four classes, according to the corresponding equivalence to N-free films, [60], and to represent them in a ternary plot (Figure 2.18):

> 1.   a-C:N. Amorphous carbon films with mainly sp^2 bonds, which are produced by low energy laser deposition, dc, rf sputtering or magnetron sputtering deposition. The introduction of N causes cross-linking between graphitic planes, and can lead to an increase in mechanical hardness and large elastic recovery.
>
> 2.   ta-C:N. Tetrahedral amorphous carbon nitrides in which the sp^3 content remains high at 80-90% up to about 10% N, and then falls rapidly similarly to the evolution of film density. These types of films are deposited by mass selected ion

beams (MSIBD), pulsed laser deposition (PLD), or filtered cathodic vacuum arc (FCVA).

3. a-C:H:N. The properties of this film are very similar to the starting a-C:H film, due to the low N incorporation (maximum content ~20% N). The hardness decreases with N concentration because of the formation of terminating groups such as NH_2 or nitrile are favored. These type of films are usually grown by plasma enhanced chemical vapor deposition (PECVD), using a mixture of hydrocarbon gas, such as methane, acetylene, benzene, and N_2 or NH_3.

4. ta-C:H:N. Tetrahedral amorphous carbon is different from a-C for its higher C-C sp^3 concentration. The introduction of nitrogen up to ~20% concentration, induce clustering of the sp^2 phase without an appreciable sp^3 to sp^2 conversion. With higher N content, sp^3 phase drop, determining softer films, similar to polymeric a-C:H:N.
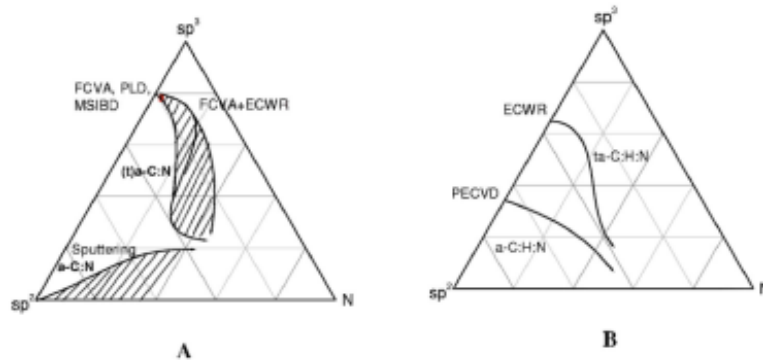
Figure 2.18   Ternary phase diagram of amorphous carbon nitrides compounds without (A) and with (B) hydrogen.[60]

For carbon nitrides systems, a multiwavelength study enables a direct correlation of Raman parameters with the N content, thanks to the different sensibility to sp^2, sp^3 and even sp^1 bonding at different energies.

In particular, a comparison between visible and UV behavior enables a more precise comprehension of the system: (Figure 2.19) shows the trend of G peak position in the amorphization and clustering trajectory for the two different excitation wavelengths.

What is now different for carbon nitrides systems is the trend inversion behavior in Stage 3: G peak position for visible or UV excitation follows two opposite trends during the clustering trajectory, defining a nonuniqueness region with the progressive N incorporation in the structure (the "bow-tie" and triangular shaped regions defined by the dotted and continuous left-pointing arrows in (Figure 2.19)). This is a clear evidence that the addition of nitrogen causes an independent evolution of sp^3 fraction and sp^2 clustering

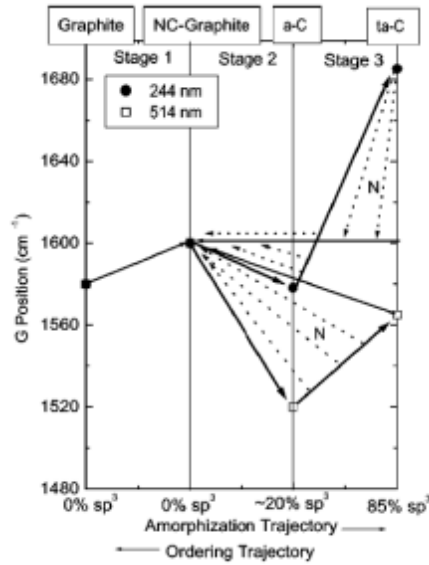*Figure 2.19   Three stage model for carbon nitrides systems for UV and visible light. Dotted arrows represent the hysteresis effect in the ordering trajectory. Their different shape determine the nonuniqueness character of stage 2 and 3 for different wavelengths [60].*

For carbon nitride samples, G width and G peak dispersion are key parameters to relate bonding properties with N concentration, but their evolution with N concentration is different for highly sp^3 samples, such as ta-C or ta-C:H, and for sp^2-rich sputtered systems, like a-C:N and a-C:N:H. A general rule can be that, for any carbon content, a reduction in G peak dispersion always means ordering and vice versa an increase of G peak dispersion always means disordering.

In the case of highly sp^3 samples, both G FWHM and G dispersion decrease with increasing N content, indicating that, for Stage3 samples, nitrogen induces a progressive ordering of the sp^2 sites in an aromatic configuration and, in general, worsen mechanical properties softening the structure.

For Stage2 a-C:N samples, G peak move downwards with N content both for 514 and 244 nm excitation wavelength (Figure 2.16a), indicating that there is no trend inversion. But still a multi wavelenght study enables to characterize the system, because G dispersion and FWHM rise with increasing nitrogen incorporation (Figure 2.16b and Figure 2.16c).

2.5 **Mechanical characterization techniques**

The nature of chemical bonds of the material under study and the structural disposition of the atoms in an ordered, nanocrystalline or amorphous state, strongly determine macroscopic coating's properties. As depicted in (Figure 2.20), a variety of hard materials can be used in nanocomposite coating design, and continue efforts are made in the research and technological development of appropriate materials that satisfy the greatest combination of good mechanical properties.

Figure 2.20   Hard materials for nanocomposite coatings in the bond triangle and changes in properties with the change in chemical bonding [63].

All these characteristics can be quantified trough loading and deformation tests, which measure the response of the material to the external action of an applied force: the deformation induced can be either elastic or plastic, according as its effect is reversible or not.

Stress and strain are two quantities that define the mechanical behavior of the tested structure, in particular, the stress is defined as the ratio between the force and the surface on which it is applied and, depending on the orientation of the load, two stresses can be distinguished:

normal stress:
$$\sigma = \frac{F_\perp}{A},$$
(2.11)

and shear stress:
$$\tau = \frac{F_{//}}{A}.$$
(2.12)

On the other hand, the deformations induced in the material as a consequence of the action of an applied force are called strains and can cause changes in both length and angles, as it is visible in (Figure 2.21). Also in this case, two different types of strain are detectable:

normal strain:
$$\varepsilon = \frac{\Delta l}{l_0},$$
(2.13)

and shear strain:
$$tg\,\gamma = \frac{\Delta x}{y}.$$
(2.14)

(a) Normal load   (b) Shear load

Figure 2.21   Schematic representation of the deformations induced by (a) normal stress and (b) shear stress [64].

Normal strain and stress are related by Hooke's law , which is a tensor relation that describes the elastic response of the material in low load regimes:

$$\sigma = E\varepsilon,$$
(2.15)

where the proportionality coefficient E is called Young modulus, and represent the capability of the material to oppose to elastic deformation.

43

When a plain is strained of ε in a given direction, an opposite perpendicular strain, called transversal strain ε_{trans}, will develop as a consequence of the tendency of the material to maintain a constant volume. It will always be of opposite sign to the strain applied, and the coefficient of proportionality is called Poisson's ratio v:

$$\varepsilon_{trans} = -v\varepsilon. \qquad (2.16)$$

Thus the elastic response of the material modifies to account for this stiffness enhancement induced by the sideway stress and Young Modulus must be replaced by the effective Young Modulus:

$$E^* = \frac{E}{(1-v^2)}. \qquad (2.17)$$

The elastic response of a material is measured also trough the elastic recovery parameter W_e, that measure the amount of elastically recovered volume after the loading displacement, and is defined as:

$$W_e = \frac{h_{max} - h_r}{h_{max}}, \qquad (2.18)$$

where h_{max} and h_r are the maximum and residual of plastic displacement.

On the other hand, the ability of a material to deform plastically before fracture is called ductility. Materials with low ductility are called brittle. Energy is required for plastic deformation, which is partially stored in the material, but mostly dissipated as heat. The specific plastic energy, the energy required during plastic deformation per unit volume, corresponds to the area beneath the stress-strain curve (Figure 2.22). The ability of a material to absorb the energy during deformation up to its fracture is called toughness.

With increasing loading, plastic deformation (also called yielding) gradually starts, but it is not possible to determine the exact point when yielding sets in. The yield strength R_p is defined as the stress level at which plastic deformation starts to occur, and the corresponding applied force is called yield load L_y.
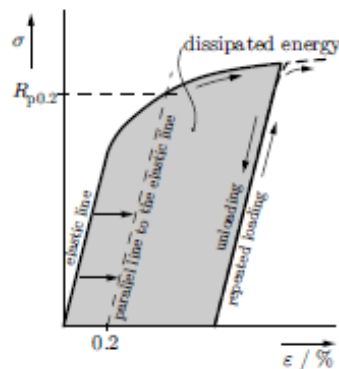

Figure 2.22   Example of a loading-unloading curve: the slope of the loading curve is the Elastic Modulus, the area correspond to the dissipated energy. The position of yield strength R_p is also reported. [64]

Hardness, *H*, is defined as the resistance of a material to indentation. Depending on the type of test adopted to measure such quantity, and to the specific indenter shape, we speak of hardness in the Mhos scale, micro-hardness or nanohardness. Indentation tests are the most common hardness tests, for they are rather easy to perform. A hard indenter with a certain geometry is pressed into the test specimen, and the surface of the indentation or the indentation depth are measured and related to the force required.

The capability of a polycrystalline sample to deform plastically depends upon dislocations movement, and a practical way to enhance mechanical resistance is to minimize their possibility of displacement though the sample.

Grain boundaries are recognized to be a good obstacle for dislocation movements, because they constitute a discontinuity in the preferential sliding planes of such type of defects. Moreover, with a decrease in grain size, the multiplication and mobility of the dislocations are hindered, and the hardness of materials increases according to the Hall-Petch relationship:

$$H(d) = H_0 + K d^{-1/2}, \qquad (2.19)$$

where H_0 and K are constants typical of a given material. This effect reach a maximum for grain size of tens of nm (Figure 2.23), but a further decrease over 10 nm worsens strength properties due to grain boundary sliding. One cause of this phenomenon is attributed to the presence of large amounts of defects at grain boundaries, which allow fast diffusion of atoms and vacancies under stress [63].
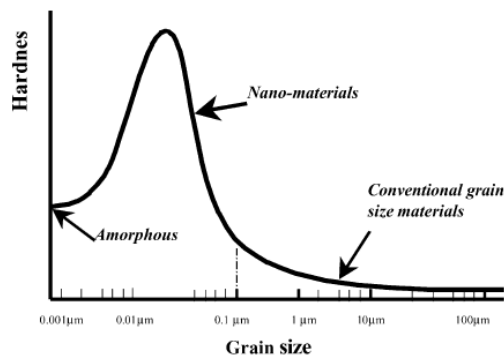

Figure 2.23   Evolution of hardness with crystal dimension [63]

The best hardness performances are obtained when all grains of the hard phase are oriented in the same direction and the size of these grains has an optimum value ranging from approximately 10 to 30 nm [65].

Another type of microstructural design is the exploitation of the mixing process, based on the addition of one or several elements to a base. Alloys are in general harder than pure elements because the combination of two or more nanocrystalline phases provides complex boundaries to accommodate coherent strain.

In recent years, superhard nanocomposites based on the combination of various transition metal-nitrides have been reported [63]. Among them, titanium carbon nitrides has been considered, as previously stated, good candidates as protective coatings, thanks to their greater chemical stability (i.e. good miscibility and chemical affinity of C and N atoms), good wear resistance and superior hardness with respect to TiN or TiC films recorded at room temperature (28 GPa and 36 GPa respectively [48]).

Both Zhang and coworkers [48], and Restello et al. [31], found the best mechanical performances for polycrystalline TiCN, with values of nanohardness ranging from $H \approx$ 30 - 45 GPa, and Young's Modulus between $E^* \approx$ 250 -360 GPa. In particular, Zhang et al. found the maximum values for a $TiC_{0.7}N_{0.3}$ phase with nanocolumnar structure. Successively, when the fine columnar structure disappears and the microstructure transformed into a mixture of nanocrystalline and amorphous phase, a new hardness diminution is observed.

Restello et al, on the other side, find that the best mechanical performances are reached at 60% of optical emission set point, and decrease monotonically with the diminution of this parameter, independently on the nitrogen content (Figure 2.24).
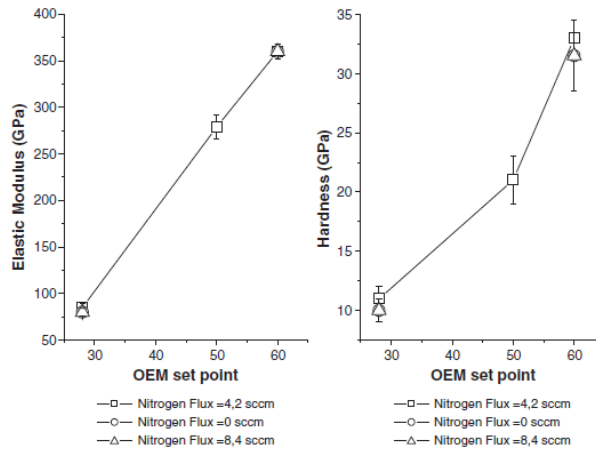
Figure 2.24   Nanohardness and Young's Modulus for TiCN samples as a function of OE set point and nitrogen flow rate [31].

Another way to obtain good mechanical performances is to embed nanocrystalline phase in an amorphous phase matrix. In this design, the size, volume percentage and distribution of the nanocrystals need to be optimized in order to obtain a compromise between superhardness and toughness. If the distance between two nanocrystals is too large, this will easily cause a crack to propagate in the matrix, while if they are too close apart, there will be interaction between atomic planes in adjacent grains. The optimal distance should be within a few nanometers [63]. The presence of amorphous phase on the boundaries helps to release strain, to deflect and terminate nanocracks, thus improving coating toughness.

Martinez and coworkers reported of a self-lubricant TiCN nanocomposite coating in a-C phase with nanohardness and elastic modulus around 20 GPa and 220 GPa respectively [49].

The resistance of a film to the formation and propagation of cracks must be attributed not only to its microstructure, but also to the mechanical properties of the substrate on which it is deposited, and on the presence of residual stress σ generated in the film during its growth. It has been proved that a sufficient low compressive macrostress prevent the formation of cracks [66].

Furthermore, it is generally known that the ability of a film to resist mechanical degradation and failure is improved by a high H/E and H^3/E^{*2} ratio. Generally, the dependence of $H(E^*)$ can be approximated with a straight line, and a general rule for good resistance against elastic strain to failure, based on the empirical data of nitrides and carbides (Figure 2.25a), is $H>0,1E^*$ [66].

The resistance of the film to plastic deformation is indeed represented by the quantity H^3/E^{*2}, which is directly proportional to the failure load [67].

This ratio is in general the most important value to describe film toughness, and it must be maximized in order to improve the film elastic recovery W_e. Also in this case, $H^3/E^{*2} > 0,1$ ensures good mechanical performances (Figure 2.25b) [66].
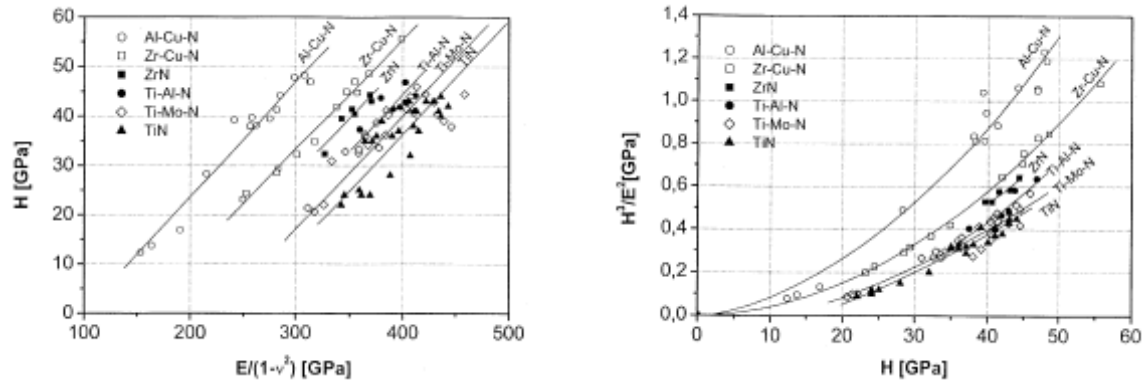
46

Figure 2.25   Relation between (a) H vs. E, and (b) H³/E*² vs. H, for selected hard nanocomposites and binary nitride films deposited by magnetron sputtering under different depsition contidions [65].*

Resistance to yielding at blunt contacts can be represented in a property map (Figure 2.26) constructed upon specific material property groups that characterize normal load resistance [67]. This map can be used to make comparative assessments of a wide range of engineering materials. TiCN coatings are expected to place in the upper right part of this panel, confirming their excellent mechanical properties.
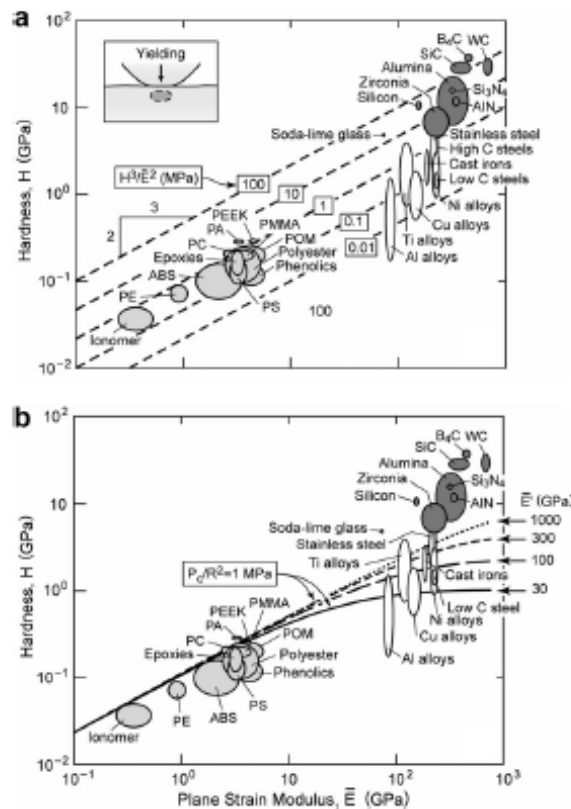

Figure 2.26   Property maps for resistance to yielding at blunt contacts for (a) rigid and (b) elastic abrasives.[67]

In parallel with nanoindentation measurements, which provide information on material's hardness and elastic modulus, scratch test are commonly used to measure their tribological properties. In this test, a tip of several materials (Steel, Si_3N_4, diamond) is drawn across the coated surface under and increasing load, until some defined failure occurs at a load termed critical load L_c. Many different failures are observed, which include coating detachment, trough-

47

thickness cracking and plastic deformation, or cracking in the coating or substrate: these failures modes are easily characterized in terms of the hardness of both substrate and coating (Figure 2.27) [68,69].
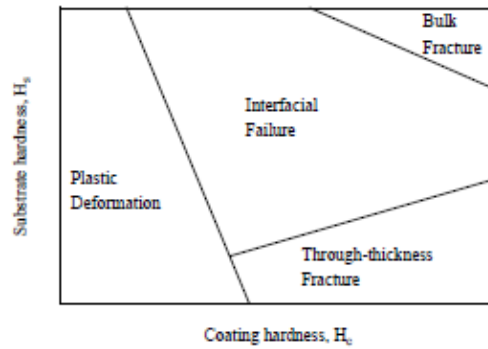

Figure 2.27   Schematic showing the various scratch test failure modes which dominate as a function of coating and substrate hardness (H_c and H_s respectively)[69].

Two quantities are important to describe the tribological character of a thin film coating: the wear rate (k) and the coefficient of friction (CoF).

The first quantity represents the adhesion to a specific substrate, and is defined through the equation:

$$k = \frac{V}{F\,s}, \qquad (2.20)$$

where V is the wear volume, F the normal load and s the sliding distance.

The wear rate of nanocomposite coatings significantly decreases with increase its hardness and especially with increasing the H/E ratio: for example, ceramic materials are brittle although they possess high hardness.

The coefficient of friction (μ) is the consequence of the simultaneous presence of a normal, P, and a tangential (or frictional) load, Q:

$$\mu = \frac{Q}{P}. \qquad (2.21)$$

Those quantities strictly depend on the material of the sliding indenter, and on the specific substrate on which the coating is deposited, and must be always specified when reporting experimental results.

Restello and co workers [31] reported that an appropriate nitrogen incorporation in the TiCN coating leads to a greater critical load for both the onset of fracture and for the total delamination.

Moreover, the presence of an a-C matrix can ameliorate friction performances of TiCN thanks to the formation of a self-lubricant transfer layer, when performing the abrasion test [35,37,47]. The built-up of such transfer layer on the surface of the indenting tip permits an easy shear within the interfacial materials and protects the counterpart against wear [70], lowering the friction coefficient. Furthermore, a distinction must be made between hydrogenated (a-C:H) and H free (a-C) amorphous carbons: it has been demonstrated that, under contact, their surface undergoes a phase transition with the local formation of aromatic structures (for a-C:H) or graphite (for a-C). These phases are characterized by low shear strengths, which will cause the formation of wear debris [70].

48

3. *EXPERIMENTAL DETAILS*

3.1 **The deposition chamber**

The industrial PVD deposition chamber present at VenetoNanotech Labs and adopted in this research work has dimensions of 700x700x800 mm^3 and is equipped with four planar magnetron in a Closed Field Unbalanced Magnetron Sputtering (CFUBMS) configuration (Figure 3.1).
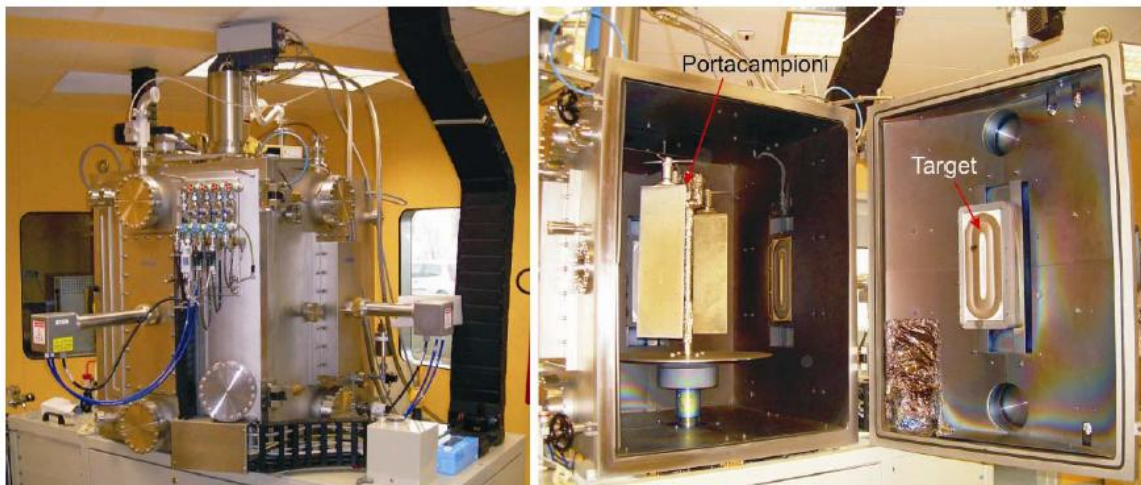

Figure 3.1   Deposition chamber present at VenetoNanotech Labs.

The four magnetrons (model AJA-ST XL series) have dimensions 4,9″x12″ and are positioned on the four internal sides of the deposition chamber. Two cathodes facing each other can be fed with DC sources with maximum power 3kW, whereas the other two are equipped with 3kW pulsed DC sources of maximum frequency 250kHz.

An High Power Impulse generator, with an operating power up to 10kW and tunable frequency up to 500 Hz, can be connectet to every cathode.

In order to prevent target heating during the high energy bombarding process, and to avoid gas desorption from the walls of the chamber, two water cooling systems with nominal flow rate of 4 L/min are implemented in the structure.

The vacuum system is composed of two stages: a rotative pump (model Alcatel pascal Series), with pumping speed of 60 m^3/h, is first adopted to reach a vacuum level of 5 10^{-2} mbar; successively, a cryogenic pump enables to reach a higher vacuum levels of 10^{-7} mbar, that consitute the base pressure of deposition process.

The substrate holder is a vertical, rotating device that, for our experimentation, was placed at a fixed position of 10cm of mean distance from the facing target. The rotational speed as well as the fine angular positioning of the vertical panel is controlled from an external software. The holder can be supplied simultaneously with an RF generator of maximum working power of 2kW, and with a DC generator of 3kW power, that are used primarily during the cleaning procedure before deposition. This biasing cannot be applied when HiPIMS generator is used, because it was found that, especially RF bias, interferes with the electronic of impulse-shape control.

The fluxes of the gases in the deposition chamber are controlled by gas flowmeters, opportunely regulated in an external control panel (PLC).

From the PLC it is possible also to control all the deposition procedures, from the pumping and venting systems, to the activation of flowmeter valves, the vacuum pumps and the cooling system.

An optical fiber connected to an external multichannel spectrometer (Avantes, 0,07 nm resolution), is mounted in the chamber in proximity of the target surface, enabling real time spectroscopic signal monitoring (OES) during the deposition proces. The optical emission spectra can be stored for a successive analisys.

3.2 **Study of nitrogen reactive gas properties**

In order to understand the mechanism leading to the formation of titanium carbon nitride materials with relevant mechanical characteristics, it is necessary to investigate plasma parameters and phenomena which occur in the plasma phase. The reactions occurring in the plasma as well as the concentrations of active species play a key role in the deposition and formation mechanism of thin film layers.

The optical emission spectroscopy (OES) is a suitable, non destructive technique based on the analysis of emission spectra of various elements constituting the plasma discharge. An optical fiber, in our apparatus collocated close to the cathode's surface, collects the emission light of the several ionization, excitation and dissociation processes occurring in the glow discharge, and this signal can be directly adopted to control the plasma processes and to investigate the relative amount of active gas species present in the deposition chamber [71,72].

Previous research works by Restello and co workers [31] demonstrated that the DC magnetron sputtering of TiCN compounds with two reactive gases (N_2 and C_2H_2) is indeed an hybrid PVD sputtering-CVD deposition process, in which nitrogen reacts with the Ti target, which is in turn subjected to sputtering by Ar ions, and C is directly deposited from the plasma.

In order to investigate nitrogen behavior in the reactive HiPIMS deposition process, and to verify its tendency to react with the solid target, spectroscopic signals from different reactive atmospheres and with two cathodes configurations (C and Ti solid targets) were analyzed.

HiPIMS deposition parameters have been varied keeping constant the peak current on target, but changing alternatively the nitrogen flux or the duty cycle, which is defined as the ratio between the pulse-on time and the total cycle time [20]. The different configurations employed are listed in Table 3-1 and Table 3-2.

Target	ν [Hz]	τ [μs]	duty cycle [%]	N_2 [sccm]	P [kW]	I peak [A]
		60	3	0	1,6	
		60	3	4	1,6	
C	500	60	3	10	1,6	250
		60	3	15	1,6	
		70	3,5	15	2	
		50	2,5	15	1,4	
		100	3	15	1,8	
C	300	70	2,1	15	1,3	250
		50	1,5	15	1	

Table 3-1: HiPIMS deposition parameters and nitrogen fluxes for carbon target.

Target	ν [Hz]	τ [μs]	duty cycle [%]	N2 [sccm]	P [kW]	I peak [A]
Ti	500	60	3	0	2	
		60	3	2	2	200
		60	3	5	2	
Ti	300	60	1,8	0	1	
		60	1,8	3	1	200
		60	1,8	6	1	

Table 3-2: HiPIMS deposition parameters and nitrogen fluxes for titanium target.

Previous works [71,72] on optical emission spectroscopy of $Ar-N_2$ and $Ar-N_2-C_2H_2$ plasma discharges, reveal the presence of N_2, N_2^+, CN and Ar species, together with C, H, CH and NH species in case of a nitrogen-acetylene plasma systems (Figure 3.2).
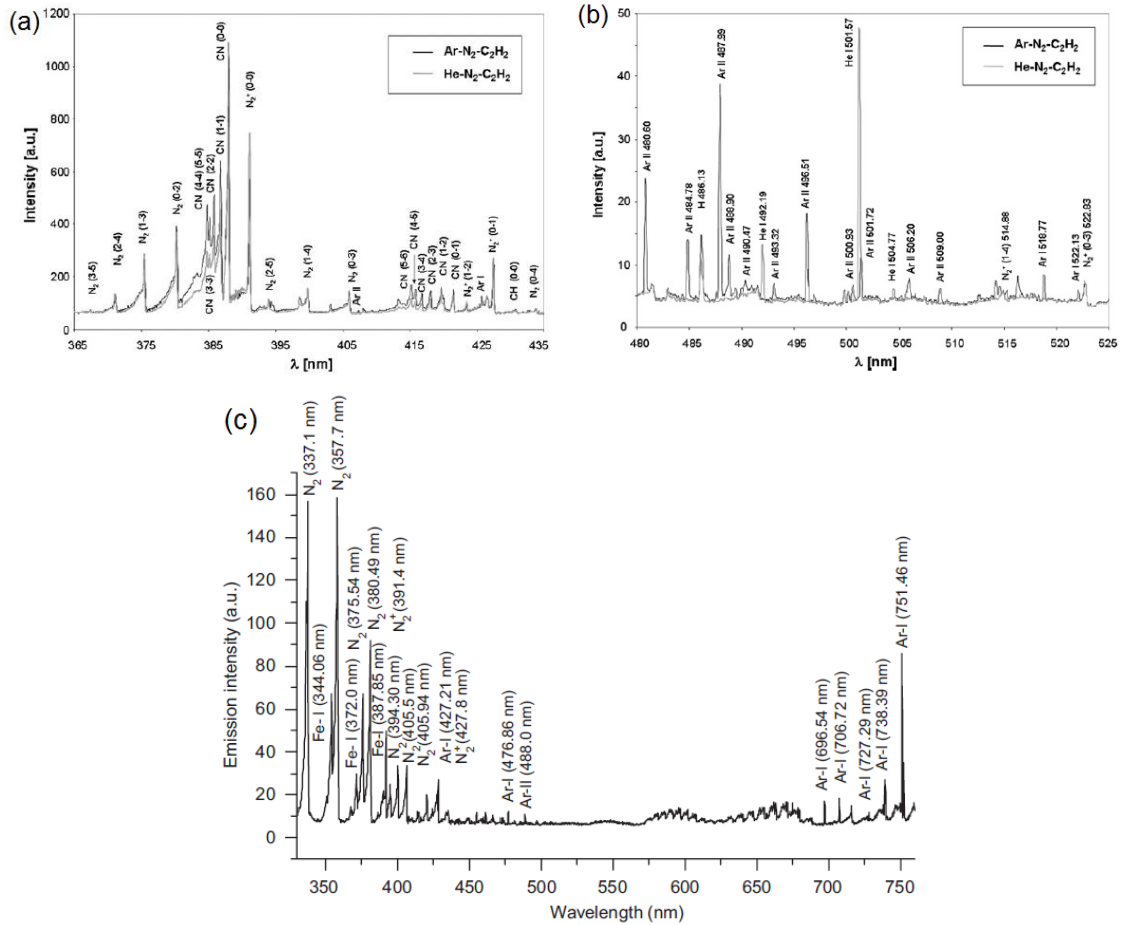
Figure 3.2   Emission spectra of $Ar-N_2-C_2H_2$, (a) and (b) [71], and of $Ar-N_2$ mixtures, (c) [72].

The emission spectra of C target at HiPIMS parameters of 500Hz frequency, 60 μs time of pulse and 1,6 kW power has been compared at different nitrogen fluxes.

In the range of wavelength 345-395 nm are clearly visible the vibrational states of N_2 molecule, together with N_2^+ state at 391,44 nm and the CN bands in the region 378-388 nm (Figure 3.3 a,b). The intensity of these optical signals is enhanced with increasing the nitrogen flux, and the presence of such vibrational states is a clear evidence of nitrogen tendency to remain preferably in molecular form and gaseous phase with a carbon target. Besides, it is not possible to determine whether the CN molecules are formed in solid state, through the reaction of nitrogen with the solid C target, or if they are formed as a consequence of recombination

processes in gas phase. Nevertheless, CN molecules are more probably originated from sputtering of complex compounds formed on the cathode.
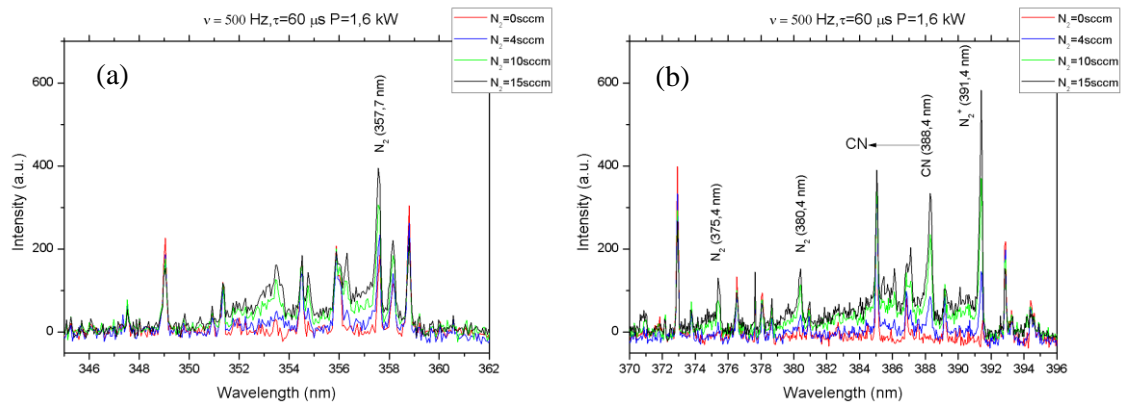

Figure 3.3   Emission spectra of Ar-N$_2$ with C target and HiPIMS parameters v=500Hz, τ=60 μs, power=1,6 kW in the range (a) 345-362 nm and (b) 370-396 nm.

A comparison with Ti target and similar HiPIMS parameters (v=500 Hz, τ=60μs, P=2kW) reveal a completely different scenario: optical emission spectra are dominated by Ti and Ti$^+$ lines (Figure 3.4), with intensities that decrease significantly with increasing nitrogen content. This is the evidence of the poisoning effect of the target and of the subsequent diminution of Ti sputtering yield as a consequence of the formation of TiN compounds on the cathode's surface.

N$_2$ signal is still present, as it is visible in (Figure 3.5), but its signal is higher than that collected with C target (superposed green line) only at high nitrogen fluxes (blue line, corresponding to N$_2$=5 sccm).
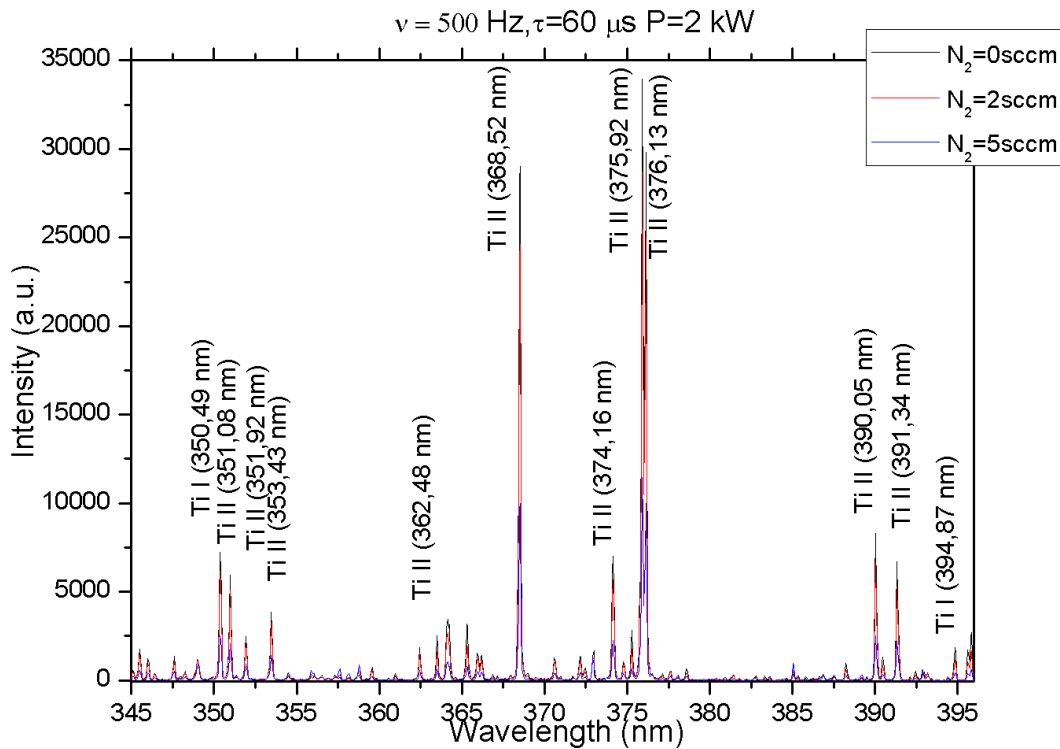

Figure 3.4   Emission spectra of Ar-N$_2$ with Ti target and HiPIMS parameters v=500Hz, τ=60 μs, power=2 kW in the range 345-396 nm.

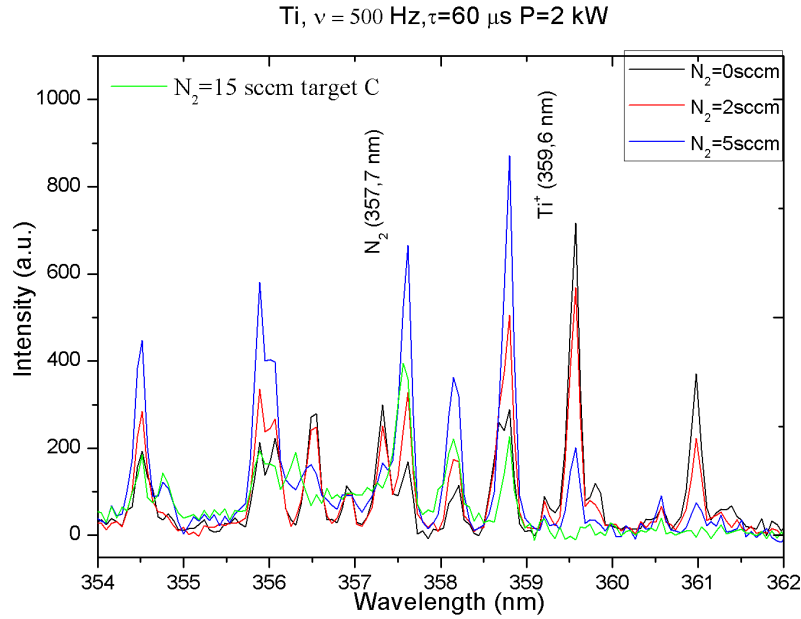*Figure 3.5 Zoom fo emission spectra of Ar-N₂ with Ti target and HiPIMS parameters v=500Hz, τ=60 μs, power=2 kW in the range 354-362 nm with superposed the signal obtain with C target in the same HiPIMS conditions (green line).*

When comparing signals obtained using C or Ti target, it is always necessary to consider the signal at higher nitrogen flow for carbon, because otherwise N excitation will be too low to be compared with signals from Ti, that appear always much more energetic. This is a first hint of the different origin of N and N^+ in the two configurations: our thesis is that Ti possesses greater affinity with N compared to C, thus N is more likely bonded to the Ti solid target. The signal of atomic or ionized nitrogen is consequently more energetic if produced by a sputtering process than by simply collision in gaseous phase.

Spectra obtained with the two C and Ti targets and varying HiPIMS deposition parameters has been compared. As can be clearly seen from (Figure 3.6a,b), intensity signals recorded at lower HiPIMS frequencies result much less intense, as a consequence of the difference in sputtering power during a single pulse. The sputtering yield can be changed by varying the duty cycle raising HiPIMS frequency ν, or pulse duration τ.

In particular, at equal HiPIMS frequency of 300Hz, the duty cycle at τ =70μs with C target is higher than with Ti target at τ =60μs (Table 3-1 and Table 3-2), whereas it will be always lower than the corresponding configuration at ν = 500 Hz.

In spite of this intensity difference caused by sputtering yield variations, in both cases N^+ signals relative to Ti target are more energetic than those belonging to C target (Figure 3.6a,b).
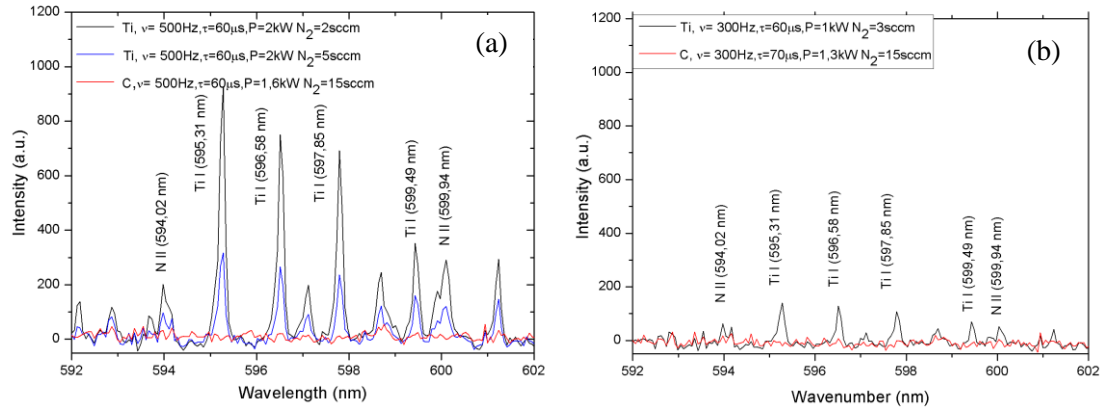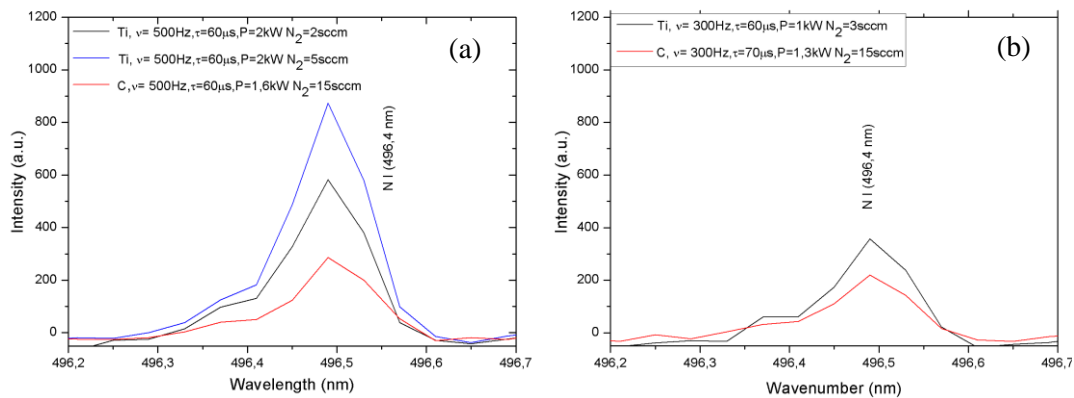
Figure 3.6   Emission spectra of different Ti and N⁺ lines in an Ar-N₂ plasma mixture at 15sccm nitrogen flux, C target (red line), and at 2sccm nitrogen flux, and 5sccm nitrogen flux with Ti target (blue and black line respectively) at (a)500Hz and (b) 300Hz HiPIMS frequency.

In order to prove the different behavior of nitrogen when changing from C to Ti target, it is necessary to investigate other N and N⁺ signals. In (Figure 3.7a-f) are reported several excitation lines, for both 500 Hz (left) and 300 Hz (right) HiPIMS frequencies. All recorded signals show a net intensity decrease when lowering the nitrogen flow when adopting Ti target, but still these signals are far more pronounced with respect to those obtained with C target.

This finding supports the hypothesis of the different nature of plasma atmospheres when changing the material constituting the solid cathode. Despite only configurations with Ti and C targets have been investigated, we can assess that an important parameter in reactive plasma deposition is the affinity between the injected gases and the target because of the possibility to form solid state bonds. In this case, sputtered atoms gain more energy if compared to atoms formed trough collision in gaseous phase, as evidenced in (Figure 3.7) for the case of nitrogen atoms. Even if our investigation doesn't concern the entire plasma extension in the chamber, because optical signals are collected in a restricted area in front of the cathode, we can suppose that ionized sputtered atoms can collide on the growing surface with superior average energy than ionized atoms from gas phase. In the latter case, ions would hit the growing film with an energy equivalent to the substrate sheath voltage, because they are supposed to arrive at the interface between the glow and the sheath with relatively low kinetic energy. On the contrary, in the former case we suppose that ionized sputtered ions can cross the glow discharge region holding, on the average, sufficiently high kinetic energy, despite some collision events may occur. This confers additional energy to the ions striking on the surface of the growing film, leading to a superior rearrangement power and to the formation of denser coatings.
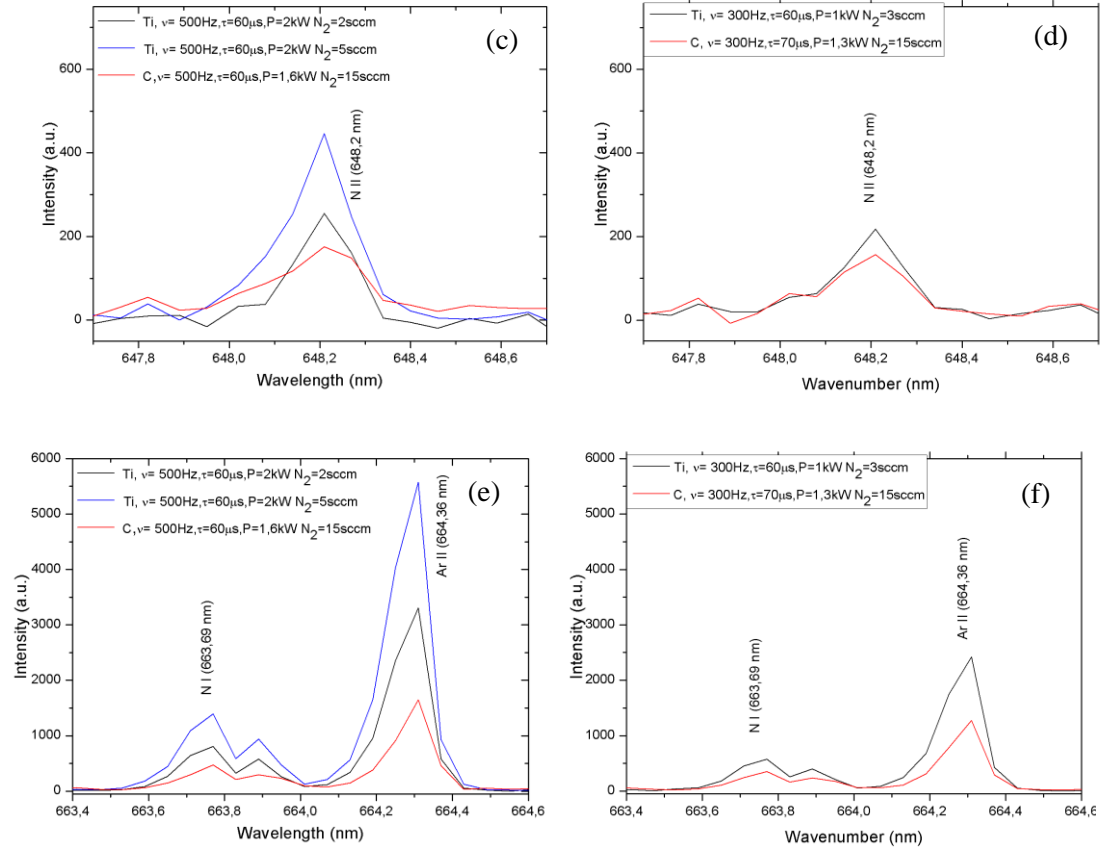
Figure 3.7   Emission spectra of different N and N⁺ lines in an Ar-N₂ plasma mixture at 15sccm nitrogen flux, C target (red line), and at 2sccm nitrogen flux, and 5sccm nitrogen flux with Ti target (blue and black line respectively) at (a)500Hz and (b) 300Hz HiPIMS frequency.

3.3 **Standardization of the deposition procedure**

As we have just outlined before, to the best of our knowledge HiPIMS technique has never been applied to the deposition of titanium carbon nitrides films, thus a first research aimed to find the best deposition parameters and the most efficient procedure has been carried out.

Reactive sputtering process can generally be controlled by partial pressure or by Optical Emission Monitoring (OEM), that is a feedback method in which the piezoelectric valve that control reactive gas flux is capable of modify its opening in order to maintain a certain value of optical emission intensity of target atoms, thus a certain partial pressure of the reactive gas in the chamber.

Nevertheless, a system of two reactive gases is more complex than a single-gas one, because of the phenomenon of trapping discussed in the first chapter [22]. Moreover, the control with a single OEM line is not suitable because both gases affect the target voltage, and thus its optical emission, hindering the determination of which of the two is responsible for the observed change in the signal [20].

Thus, in order to control stoichiometry, we tried to optimize one method that exploit nitrogen's hysteresis curve, since acetylene is poorly affected by this phenomenon.

The hysteresis method

This method is based on the determination of the appropriate values of reactive gas fluxes that has to be adopted if a desired TiC_xN_{1-x} stoichiometry will be deposited. To overcome the

problem of partial pressure control of both reactive gases in the chamber, that is not supported by our deposition apparatus, a correlation with gases pressures and their relative variation in a plasma-off regime has been supposed to be valid. That is, combined partial pressure variation of both reactive gases as a consequence of fluxes variation is supposed to follow a similar linear relationship with and without plasma.

Thus, with argon pumped at a constant flux of Ar = 60sccm in the deposition chamber, but with no plasma activity, the evolution of pressure with increasing filling reactive gas has been recorded separately for nitrogen and acetylene gas. The two linear evolution are reported in (Figure 3.8a,b).
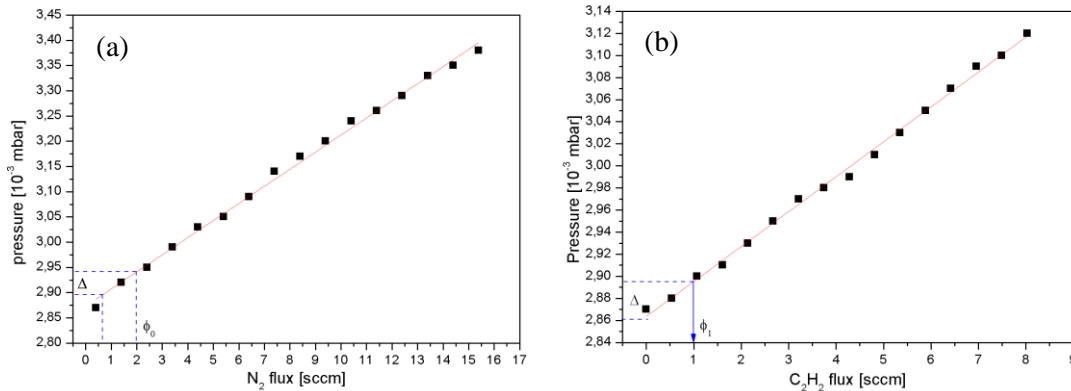

Figure 3.8   Linear evolution of chamber pressure with increasing the flux of (a) nitrogen and (b) acetylene, at a constant argon flux of 60sccm.

Then, HiPIMS generator has been switched on, and two hysteresis curves for nitrogen reactive gas has been recorded at different values of duty cycle and power applied. As a reference of the state of Ti target poisoning, the intensity of Ti optical emission line at 499,1 nm has been recorded.

It has been pointed out that the configuration with lower frequency leads to a more instable condition, with a fast transition in the poisoned regime. Evidently, the cathode isn't supplied with enough energy to enable a sufficient target cleaning during the pulse on time, thus the HiPIMS parameters that has been set are:

$$\text{frequency } \nu = 500 \text{ Hz, impulse time } \tau = 60 \text{ μs, power P} = 2\text{kW.}$$

Nitrogen hysteresis curve is reported in (Figure 3.9), and positioning at 60% OE of Ti metallic we determined the mean flux value ϕ_0 to obtain a stoichiometric TiN compound, as reported by Restello and coworkers (Figure 2.4) [31].
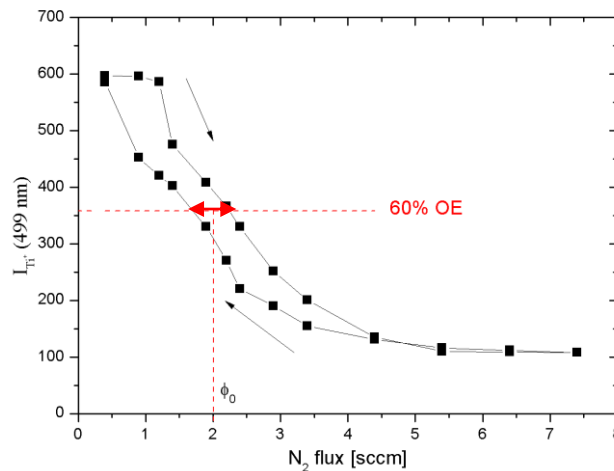

Figure 3.9   Nitrogen hysteresis curve.

Successively, an expected diminution in partial pressure of N_2 was associated to a definite nitrogen incorporation in the final compound with stoichiometry TiC_xN_{1-x}: namely, if $\phi_0 = 2$ sccm of N_2 were expected to produce a prefect TiN phase, for the production of a $TiC_{0.7}N_{0.3}$ coating we take the 30% of ϕ_0 and we associated the relative pressure diminution Δ for nitrogen to a Δ pressure increase for acetylene, as a consequence of its introduction in the deposition chamber (Figure 3.8a,b). This value determines the C_2H_2 flux (ϕ_1) that will be introduced during the deposition.

At this point, it is necessary to determine the new hysteresis curve of nitrogen in an atmosphere of argon and acetylene (Figure 3.10). Being poisoned from the presence of C_2H_2 in the chamber, Ti target will present lower starting intensity from its metallic state, and imposing the 60% OE level on the new starting optical emission value, we determined the final nitrogen flux (ϕ_2) to obtain stoichiometric TiC_xN_{1-x} conditions. If the injected acetylene flux is changed, an appropriate hysteresis curve must be measured in order to consider the effects of a different reactive gas content.

We reported as an example in (Figure 3.10) the new N_2 hysteresis curve with $\phi_1= 1,0$ sccm. In these conditions, we take $\phi_2 = 2,2$ sccm.
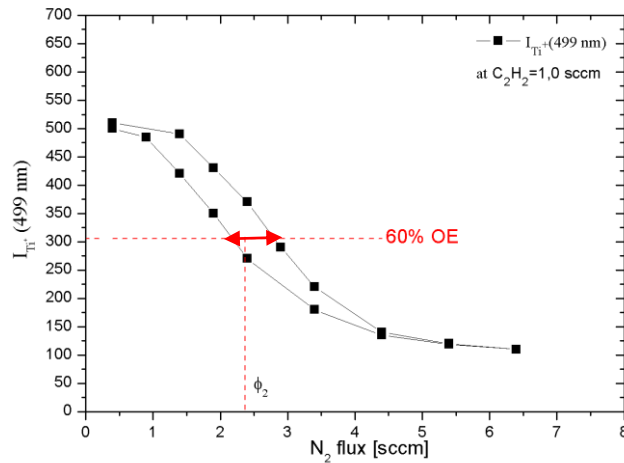

Figure 3.10   Nitrogen hysteresis curve with $C_2H_2=1,0$ sccm filling the chamber.

As expected, we can note clearly a downshift toward lower values of optical emission intensity as a consequence of the acetylene contribution to target poisoning. Moreover, the hysteresis curve seems to be shifted towards higher nitrogen values, and this behavior is not foreseen by theoretical modeling of a two reactive gas system. We supposed that this phenomenon could be ascribed to a reaction between N_2 and C_2H_2, or their byproducts after dissociation, in gaseous or solid phase, probably as CN molecules. Interaction in gaseous phase between reactive gases is not included in the theoretical model, but if it is true, we would observe also CN optical signal in the spectroscopic monitoring: because a little percent of N will form bound with gaseous C, more nitrogen must be effectively introduced in the deposition chamber to poison the Ti target.

Successively, to test HiPIMS pulse parameters, some hysteresis curves in a two reactive gas atmosphere has been recorded, varying the pulse duration and frequency (300 Hz 60 μs, and 250 Hz 120 μs respectively) but maintaining the same peak current on the target. In all cases the process was unstable and ultimately produced a sudden switch off of HiPIMS generator as a consequence of continuous variations in cathode voltage and power, incremented by a strong arcing occurrence. We thus decided to maintain the HiPIMS parameters adopted for the first measurements, namely impulse time $\tau = 60$ μs, frequency $\nu = 500$ Hz and power P = 2kW.

The first set of samples has been deposited both on monocrystalline Si [001] and on mirror polished steel substrate. Multiple depositions were possible thanks to the presence of a rotating substrate holder.

The decided stoichiometry was $TiC_{0,7}N_{0,3}$ because of its superior mechanical and tribological properties reported in literature [28,48]. Sputtered target was pure titanium (99,9999%) and N_2 and C_2H_2 fluxes has been set trough the hysteresis method described above. The deposition parameters are listed in Table 3-3.

Prior to deposition, samples were sputter etched with a RF biased glow discharge in Ar atmosphere for 60 minutes. Successively, Ti target has been polished in HiPIMS regime, at P=2kW, τ = 60 μs, ν = 500 Hz for 10 minutes, and then a thin Ti interlayer was deposited in these conditions in order to ameliorate adhesion properties.

No intentional heating or bias was applied to the substrate during the deposition.

At first, C_2H_2 was injected in the chamber in order to deposit the thin ($\approx$100 nm) TiC layer at 60% O.E.; successively, N_2 was gradually introduced and a real time monitoring of the OE emission line of Ti (499,1 nm) was adopted in order to maintain the desired OE level. This time-dependent optical emission monitoring is different from the computerized method adopting the piezoelectric valve for flux control, described previously: in this case, the relative flow of reactive gases is changed manually in order to maintain at a constant value of the optical emission line of Ti. This method has been adopted by other researchers [31], and it has been proved to be reliable.

Sample	C_2H_2 [sccm]	N_2 [sccm]	Base pressure [mbar]	Deposition time [min]
TiCN0,6a	0,6	2,5	$2,2 \times 10^{-6}$	60
TiCN0,8a	0,8	2,4	$2,2 \times 10^{-6}$	60
TiCN1a	1,0	1,9	$2,2 \times 10^{-6}$	60
TiCN1b	1,0	2,2	$4,0 \times 10^{-6}$	60
TiCN1,2b	1,2	2,4	$4,0 \times 10^{-6}$	60
TiCN1,4b	1,4	2,0	$4,0 \times 10^{-6}$	60
TiCN1,2d	1,2	2,4	$3,6 \times 10^{-6}$	150
TiCN1,4d	1,4	2,1	$3,6 \times 10^{-6}$	120

Table 3-3: Deposition parameters for the first set of samples deposited both on Si [001] and on steel substrates. Different letters refers to different days of deposition.

From the analysis of this first set of samples, some problematic were evident:

1. Relevant problems of adhesion of the film on both the substrates: most of them were partially delaminated, and eventually completely fractured, in the case of thicker TiCN film on Si substrates. This was ascribed to the formation of high compressive stress, evidenced also by a characteristics delamination in fragments of circular shape, as can clearly be seen from microscope images (Figure 3.11a,b taken with Leica microscope). A second cause of delamination was attributed to a poisoning effect in the multiple deposition process: independently of the reactive gas fluxes, the first sample was always the one that present the best adherence properties, whereas the second and third were often delaminated.
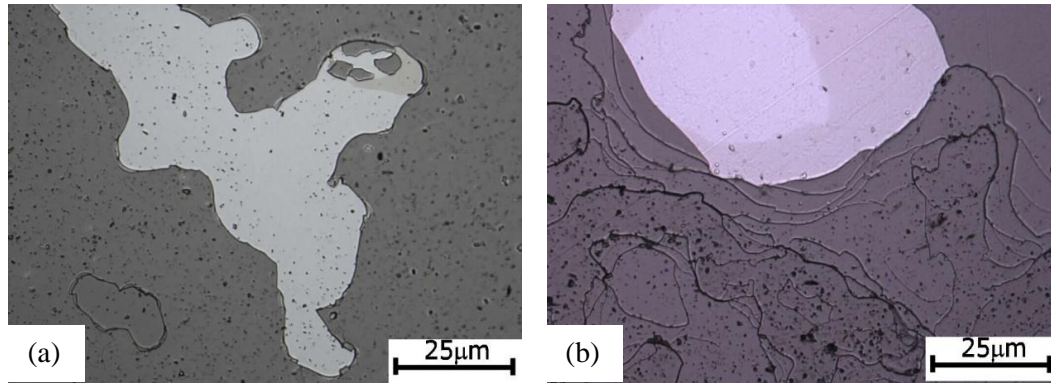
Figure 3.11   Microscope images at 500x magnification of (a) TiCN1,2b on Si substrate and (b) TiCN1,4d on steel substrate.

2. Stoichiometry was not the one expected: EDS measurements reveal a poor incorporation of titanium (comprised between $28 \div 42$ at %) that produce the formation of understoichiometric compounds which composition range from nearly TiN to $Ti_{0.45}C_{0.21}N_{0.34}$. This is probably a consequence of the complex reactive gas behavior in glow discharge with respect to their interaction in a non-plasma state. The hysteresis method appears to be too simplified to correctly predict the relation between the changes in partial pressure of reactive gases and the expected fluxes, but the values obtained could be a starting point for a successive optimization of deposition condition in order to achieve the desired stoichiometric elemental incorporation.

To overcome these problems some important changes has been adopted: primarily, multiple deposition has been abandoned, in order to avoid poisoning effects coming from adsorption of reactive gases on the substrates that are not subject to deposition.

Secondly, to ameliorate adhesion, the interlayer structure has been changed from Ti+TiC to Ti+TiN, as also reported in some literature works [31,47]. This implies that it is no more possible to adopt hysteresis method for flux determination, because a fixed acetylene flux was primarily introduced in the chamber to deposit the TiC phase. Only in a second step nitrogen was introduced, and its poisoning behavior was calibrated on the pre-existence of the second reactive gas in the chamber.

We thus decided to completely control the deposition method through the constant time monitoring of a series of optical active lines of the species that are present in the plasma, and that we associated to compositional information on the relative abundances of the elements in the growing film.

As previously mentioned it is possible to monitor C/Ti ratio and the amount of Ti incorporation in the structure varying the OE set point of Ti (499,1 nm). Some other emission lines that we recorded are H(656,3 nm) and N(663,7 nm) in order to relate their evolution to the content of C/Ti and C/N respectively.

A set of samples on both Si and steel substrates has been deposited with HiPIMS at OE set point of 60%, 40% and 25%, in order to reproduce a set of coatings of similar composition of those obtained by Restello and coworkers [31] (Figure 2.4) by RF biased DCMS, which possess good mechanical and tribological properties. We have thus the possibility to investigate the effects of the new deposition technique on microstructural and mechanical properties with a good comparative reference.

Prior to deposition, all substrates were cleaned with sputter etching in Ar atmosphere (Ar = 60 sccm), with RF pulsed power of 700W and DC bias voltage of -300V applied to the substrate for 60 minutes.

Ti target was cleaned for 10 minutes in HiPIMS regime, to restore its metallic state prior to every deposition. HiPIMS impulse parameters, adopted also for the successive Ti interlayer and coating deposition, are listed in Table 3-4:

Frequency v [Hz]	Pulse time [μs]	Power [kW]	Voltage [kV]
500	60	2	0,58

Table 3-4: HiPIMS deposition parameters.

Deposition parameters and thickness of the second set of samples are listed in Table 3-5. The thickness of the film was measured with a stylus profilometer (α-Stepper IQ, KLA Tecnor) with a step height repeatability of 7,5Å (1σ) or 0,1%, tip with a radius of 2μm and a conic angle of 40°. Measures were repeated over the whole sample's longitudinal dimension and successively mediated.

Sample	OE set point	C_2H_2 flux [sccm]	N_2 flux [sccm]	Thickness [nm]	Base pressure [mbar]
TiCNf	60%	2,1	1,6	1138 ± 9	$3,7 \times 10^{-6}$
TiCNg	60%	1,6	1,8	2057 ± 18	$3,0 \times 10^{-6}$
TiCNh	40%	1,6	2,3	2006 ± 20	$2,9 \times 10^{-6}$
TiCNi	25%	1,7	3,4	1589 ± 20	$3,1 \times 10^{-6}$

Table 3-5: Process parameters and thickness for coatings obtained with HiPIMS at different optical emission conditions.

Two different samples at 60% OE were repeated with different C/N ratio. The transition from the stoichiometric TiN configuration to the desired value of OE has been obtained varying the nitrogen flux, and successively introducing acetylene gas in the chamber in order to maintain constant the optical emission level. Acetylene was increased with respect to previous values to allow major C incorporation.

It is evident from (Figure 3.12) that the evolution of OE emission line for Ti (499,1 nm) is subject to a drift process that leads to a progressive enhancement of titanium signal. As a consequence, reactive gas fluxes have been stepwise changed during the deposition, leading to the production of a relatively graded coating structure.

Moreover, the deposition process was fairly unstable, with frequent arc on the target surface and variation in supplied target power. This produce a rough surface with droplets and impurities, as is clearly visible from microscope images in (Figure 3.13), but all the coatings appeared now perfectly adherent to the substrate, indicating that TiN interlayer was a correct solution to prevent the problem of delamination. The drops are caused by the phenomenon of arcing, a typical disadvantage of reactive magnetron sputtering process: during reactive MS of TiC phase with hydrocarbon gases, the growth of less conductive amorphous-carbon islands has been reported [40]. The local potential increase due to the presence of such poorly conductive islands leads to unipolar arc discharges, and to the ejection of droplets of materials from the target that worsen the quality of the growing coating. Modern HiPIMS power suppliers are equipped with arc detection and suppression mechanism (a short interruption of the process when an arc is detected). However, the brief period of an arc existence before its suppression may be detrimental to the coating quality [7].

Even if deposition time is similar for samples TiCNg, TiCNh and TiCNi (Figure 3.12), coatings thickness decrease monotonically with increasing nitrogen flux injected (Table 3-5), as a consequence of the lower sputtering yield of TiN compound with respect to metallic Ti, which was formed on the surface of the target.

Coatings are all of red-purple color and compositional analysis, carried out with EDS apparatus (Bruker X-flash SSD technology), revealed still an abundance of nitrogen incorporation, that was not in accordance with the desired stoichiometry. Compositional values are reported in a triplot diagram (Figure 3.14).
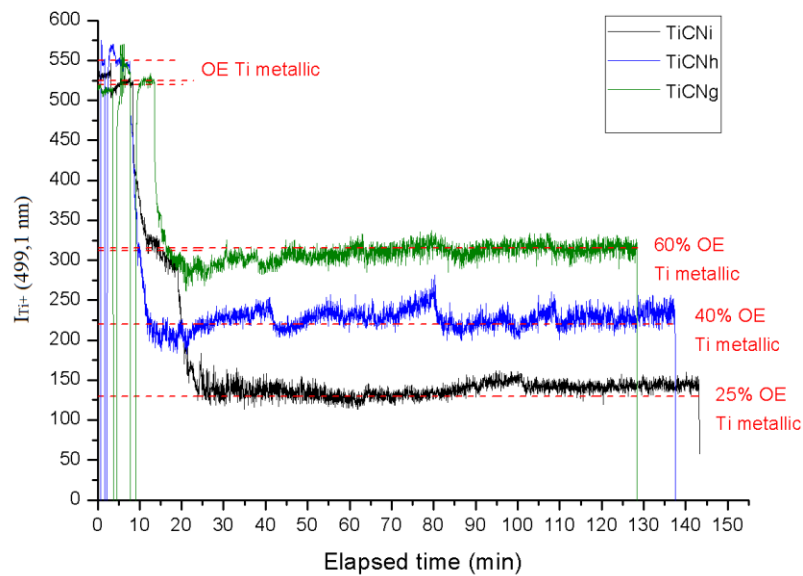
Figure 3.12   Evolution of OE emission line of Ti$^+$ (499,1 nm) with deposition time.
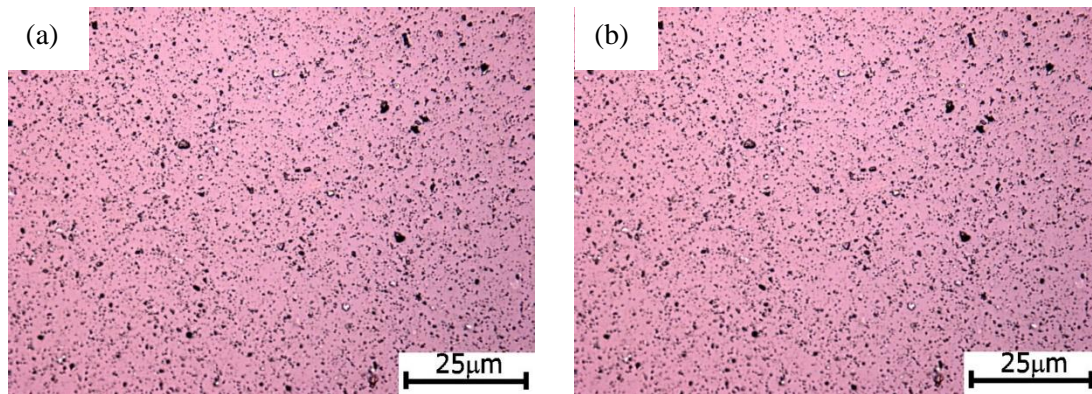

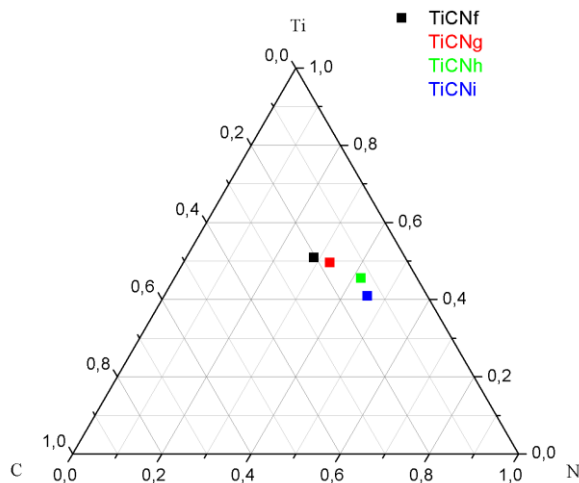*Figure 3.13   Microscope images of (a) TiCNg and (b) TiCNh surface with magnification 500x.*

Figure 3.14   Triplot with C,N,Ti concentration of samples TiCNf, TiCNg, TiCNh, TiCNi from EDS measurements, represented without error component.

It is evident from (Figure 3.14) that, also for HiPIMS technique, the optical emission method is suitable to control the global Ti content, and that variations in N_2 flux affect more the compositional character of the coatings than C_2H_2, especially if it is adopted to control the OE set point level.

It was thus necessary to realize a new set of samples with the appropriate stoichiometry and with a less pronounced graded structure. We focused on the optimization of samples at 60% OE.

Deposition parameters are listed in Table 3-6; HiPIMS parameters remained the ones reported in Table 3-4, and the same substrate etching procedure and target cleaning method of the precedent samples has been applied to the new ones.

Sample	OE set point	C_2H_2 flux [sccm]	N_2 flux [sccm]	Thickness [nm]	Base pressure [mbar]
TiCNm	60%	2,4	1,5	2090 ± 19	$2,8 \times 10^{-6}$
TiCNn	60%	2,7	1,3	1796 ± 6	$4,6 \times 10^{-6}$
TiCNo	60%	2,5	1,3	1241 ± 8	$2,9 \times 10^{-6}$

Table 3-6: Process parameters and thickness for coatings obtained with HiPIMS at different acetylene fluxes.

In this case, the transition from the TiN to the TiCN structure has been carried out enhancing preferentially C_2H_2 flux and maintaining N_2 flux to low values.

Optical emission signal was still affected by a slow drift process that forces a step variation of acetylene during all the deposition. In order to avoid this configuration, for sample TiCNo the screen was placed in front of the target during the transition procedure from the interlayer to the TiCN coating. Once obtained the stabilization of optical emission line and reactive gas fluxes, the substrate was turned in front of the target, and a single TiCN layer was deposited. Nevertheless, this sample failed by fracture due to the high stress developed at the interface with the interlayer.

Sample surface appeared grayish, and the chemical composition measured by EDS technique confirmed the increase of C incorporation to a stoichiometry of $TiC_{0.5}N_{0.5}$ for TiCNn sample.

In order to obtain a TiCN monolayer, a faster variation of reactive gas fluxes is needed to minimize the duration of the transition phase.

A new set of samples has been deposited reducing this transition time and maintaining HiPIMS parameters to the values reported in Table 3-4. Prior to deposition, the sputter etching

62

in RF biased regime and the cleaning target procedure described previously has been applied to all the samples.

The interlayer structure was standardize as follows: a thin Ti interlayer of 100nm was deposited in 5 minutes in HiPIMS mode; successively, N_2 was introduced in the deposition chamber in order to reach 60% OE of Ti (499,1nm) line, and TiN interlayer of about 200nm thickness was deposited in 10 minutes. Finally, nitrogen flux was lowered to the minimum value supported by flowmeters valves, and acetylene flux was progressively introduced and varied continuously, in order to maintain the stability of titanium's optical signal. The achievement of stable deposition parameters was obtained in 15 minutes: after that time a good monolayer TiCN structure has been deposited, and it was found that the overall process suffer less of instabilities and drift effects.

Deposition parameters are listed in Table 3-7 together with deposition rates of the TiCN layer (interlayer contribution has been subtracted).

Sample	OE set point	C_2H_2 flux [sccm]	N_2 flux [sccm]	Thickness [nm]	Deposition rate [nm/min]	Base pressure [mbar]
TiCNp	60%	2,7	0,7	1653 ± 14	$18,0 \pm 0,2$	$4,6 \times 10^{-6}$
TiCNq	40%	4,2	0,7	1710 ± 8	$18,5 \pm 0,1$	$4,3 \times 10^{-6}$
TiCNr	27%	6,3	0,7	2034 ± 14	$23,1 \pm 0,2$	$4,0 \times 10^{-6}$
TiCNs	60%	2,3	1,4	1569 ± 14	$18,1 \pm 0,2$	$3,9 \times 10^{-6}$

Table 3-7: Process parameters,thickness and deposition rate for coatings obtained with HiPIMS at different OE set point.

Sample TiCNs has been deposited with higher nitrogen content, with respect to the other coatings, in order to investigate the role of N incorporation on microstructural and mechanical properties in stoichiometric compounds.

The evolution of optical emission signal is reported in (Figure 3.15) from which it is visible the major stability of this new deposition method during all the process time. All samples were perfectly adherent to both the Si and the steel substrates, but at the surface are still visible some droplets caused by arcing (Figure 3.16a,b).
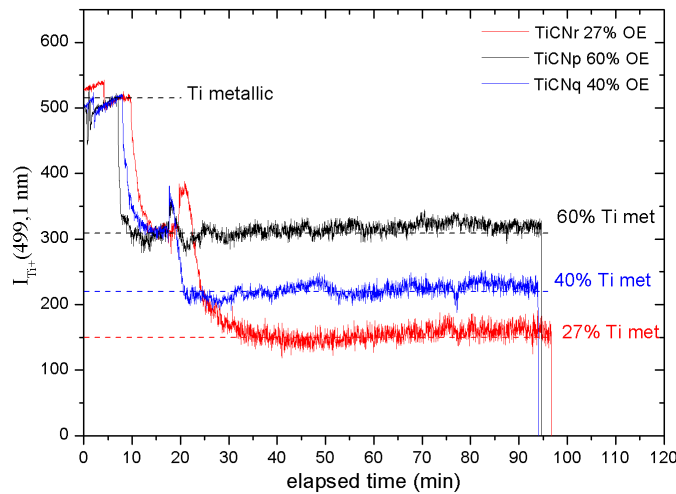

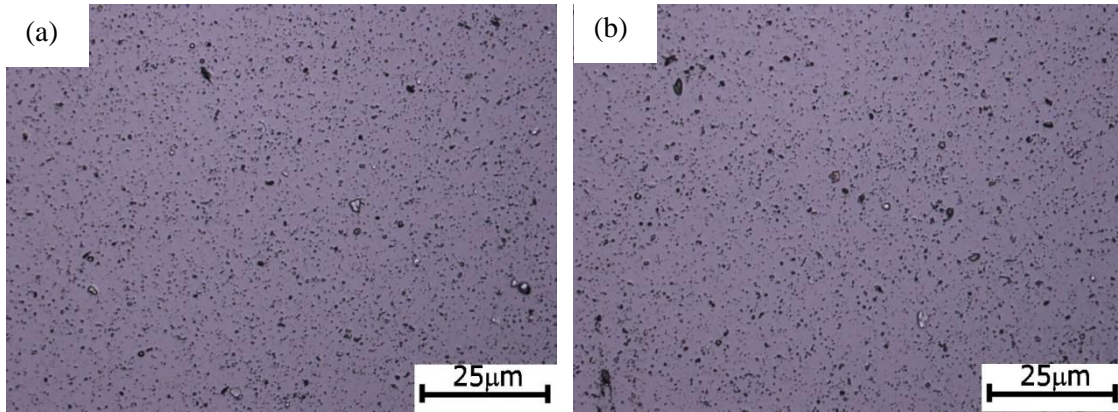*Figure 3.15 Optical emission signal of Ti$^+$ (499,1nm) line for samples TiCnp, TiCNq, TiCNr.*

Figure 3.16   Microscope images of (a) TiCNq and (b) TiCNr surface with magnification 500x.

This last set of samples has been characterized from a compositional, microstructural and mechanical point of view, and results will be presented in the next chapters.

In order to compare TiCN properties and general features with the titanium carbide and titanium nitride compounds, a set of samples of TiN and TiC has been deposited in addition by HiPIMS. Process parameters are listed in Table 3-8 and Table 3-9 respectively.

Frequency ν [Hz]	Pulse time [μs]	Power [kW]	Voltage [kV]
500	60	2	0,58
Sample	Base pressure [mbar]	N_2 flux [sccm]	Thickness [nm]
TiN	$2,6x10^{-6}$	2,5	791 ± 6

Table 3-8:   Process parameters, and thickness for TiN coating obtained with HiPIMS in stoeichiometric OE set point conditions.

Frequency ν [Hz]	Pulse time [μs]	Power [kW]	Voltage [kV]
300	150	2	0,48
Sample	Base pressure [mbar]	C_2H_2 flux [sccm]	Thickness [nm]
TiC4	$2,3x10^{-6}$	4	1800
TiC6	$2,3x10^{-6}$	6	1400
TiC10	$2,3x10^{-6}$	10	1500

Table 3-9:   Process parameters, and thickness for TiC coatinsg obtained with HiPIMS with different acetylene fluxes.

All samples possess a thin Ti interlayer to ameliorate adhesion to the Si [001] substrate.

Samples TiC has been deposited with HiPIMS parameters that are different from the TiCN ones, because they refer to a previous research work. Nevertheless, they were suitable to the comparison of microstructural and mechanical properties with TiCN compounds.

3.3.1   OES analysis

A first hint of reactive gas behavior in the glow discharge, and consequently their relative influence on film composition, is given by optical emission spectroscopy: the basic premise of this technique is that the emission intensity of particular wavelength from an excited state is proportional to the concentration of species in that excited state [72].

From an analysis of the emission spectra it is clearly visible an increasing intensity trend in C^+ (426,7 nm) and in H^+ (656,2 nm) lines with raising the acetylene flux injected in the

deposition chamber (Figure 3.17 and Table 3-7). Hydrogen is first produced by electron impact from the cracking of the C-H bond in the acetylene (H-C≡C-H) molecule: in fact C-H possess lower bond energy (5,8 eV) than C≡C (10 eV). Successively, C_2H radical may be dissociated in CH molecule as a result of impact with argon ions [71].

On the other side, the evolution trend of CH (431,4 nm) molecular line (Figure 3.18a) demonstrates that, at equal nitrogen flux, the sample with lower acetylene flux (TiCNp) is mainly dissociated in CH molecules, whereas in samples deposited with higher C_2H_2 values (TiCNq, TiCNr,), a grater fraction of C_2H_2 molecules completely dissociate, as a consequence of the more frequent collisions with heavier Ar ions.

Sample TiCNs possess the lowest amount of acetylene flux, and it is thus expected to show the minor C, H, and CH intensity values.

CN (388,4 nm) line is also visible (Figure 3.18b), with the same evolution trend of CH emission line and with similar intensities. The observation of CN signals demonstrates that the two reactive gases react not only in solid phase on the surface of the target, but also in gaseous state, thus complicating the mathematical model for the comprehension of dynamic of reactive species in a glow discharge. This finding account for the shift towards higher flux values of nitrogen's hysteresis curve (Figure 3.10) observed during the optimization of deposition process.

Finally, the decreasing trend of Ti (499,1 nm) line is a clear evidence of the progressive target poisoning from carbon atoms coming from the dissociation process of acetylene molecules, that are in constant competition with nitrogen atoms on the cathode's surface (Figure 3.19)
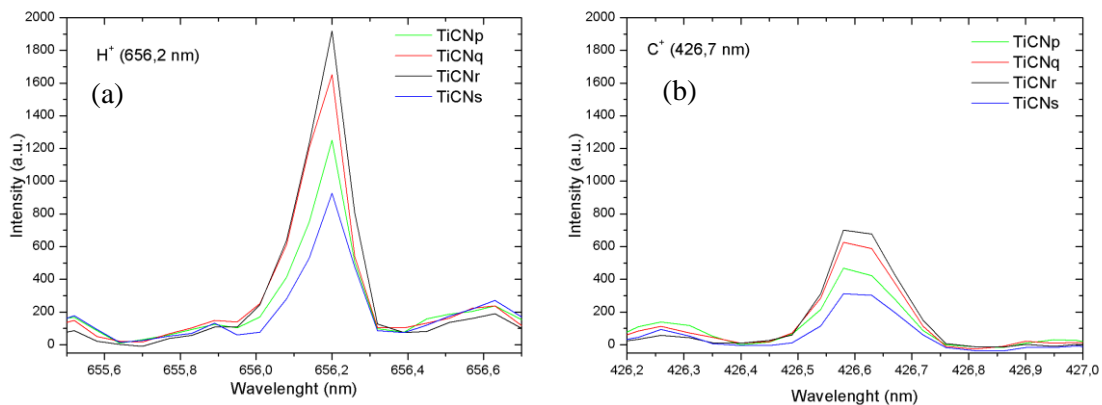

Figure 3.17   Emission spectra of (a) H^+ (656,2 nm) and (b) C^+ (426,7 nm) lines of samples TiCNp, TiCNq, TiCNr and TiCNs.
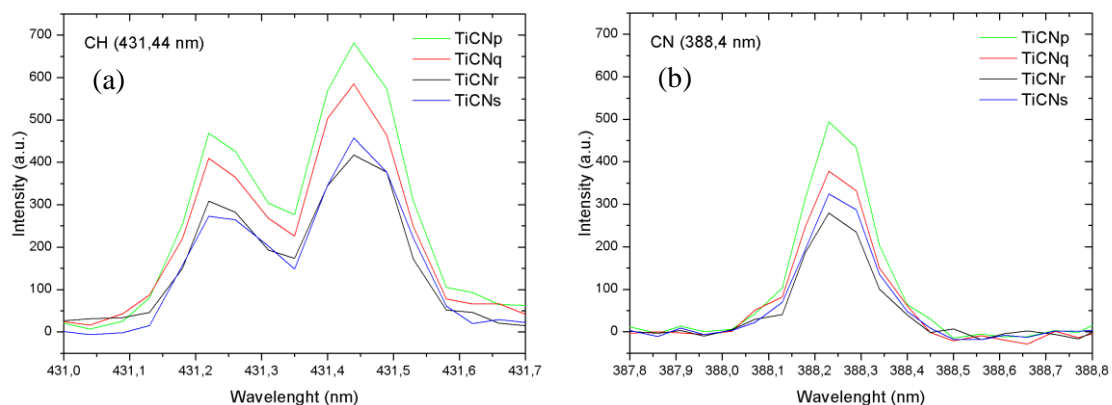

Figure 3.18   Emission spectra of (a) CH (431,44 nm) and (b) CN (388,4 nm) lines of samples TiCNp, TiCNq, TiCNr and TiCNs.
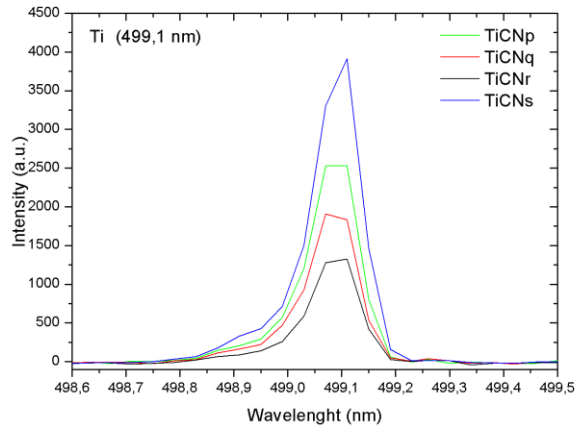
Figure 3.19   Emission spectra of Ti (499,1 nm) line of samples TiCNp, TiCNq, TiCNr and TiCNs.

4. *MICROSTRUCTURAL CHARACTERIZATION*

4.1 **Morphological analysis**

A scanning electron microscope (SEM, VEGA TS 5130 LM, Tescan, W filament) was employed to observe the morphology of the coating cross-sections. The accelerating potential of the electron beam was set to 30 kV, and both secondary electrons (SE) and backscattered electrons (BSE) were recorded.

We will report and discuss separately SEM images relative to the set of TiCN coatings (Figure 4.1a-d), and successively those of TiC (Figure 4.2a-c) and TiN (Figure 4.3) samples.

Morphological structure evolution of titanium carbon nitrides coatings can be regarded in function of the total carbon content: in accordance with literature findings, and as explained in paragraph 2.2, with increasing C incorporation, coating's structure evolves from a dense fine nano-columnar to a glassy disordered phase. This last configuration is visible in sample TiCNq and TiCNr (Figure 4.1b,c respectively), whereas BSE images of stoichiometric samples TiCNp and TiCNs (Figure 4.1a,d respectively) reveal the ordered, compact columnar structure.

The interlayer formed by a thin Ti+TiN is always visible as a brighter horizontal line in BSE images, as a consequence of the different chemical composition that induce a variation in backscattering electrons' yield.

Moreover, SEM images confirm the denser structure typical of HiPIMS deposited coatings, displayed in (Figure 2.6), as a consequence of the greater ion bombardment to which is subjected the growing film with respect to DCMS deposition technique, which instead presents a more open structure with a higher fraction of intercolumnar voids (Figure 2.5a). The relative surface mobility of Ti, C and N atoms is the most important parameter governing the columnar growth of these nanostructured coatings.

As reported by several papers, [41,44,48], an increasing amount of C atoms impinging on the film's surface are expected to decrease the atomic diffusivity during the deposition, whether they come from a solid graphite target or from the dissociation of the reactive gas. As a consequence, the agglomeration of C atoms at grain boundaries hinder crystalline grain growth, causing the suppression of the columnar structure, and the transition to a nanocrystalline phase embedded in an amorphous matrix.
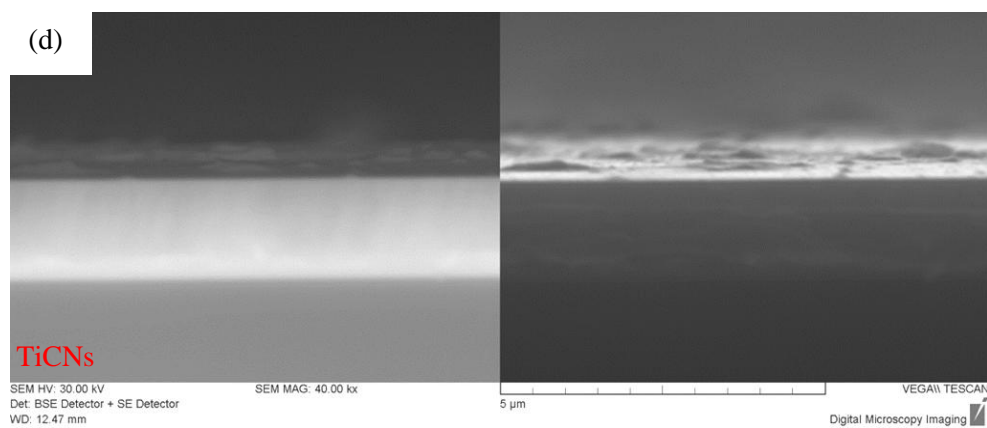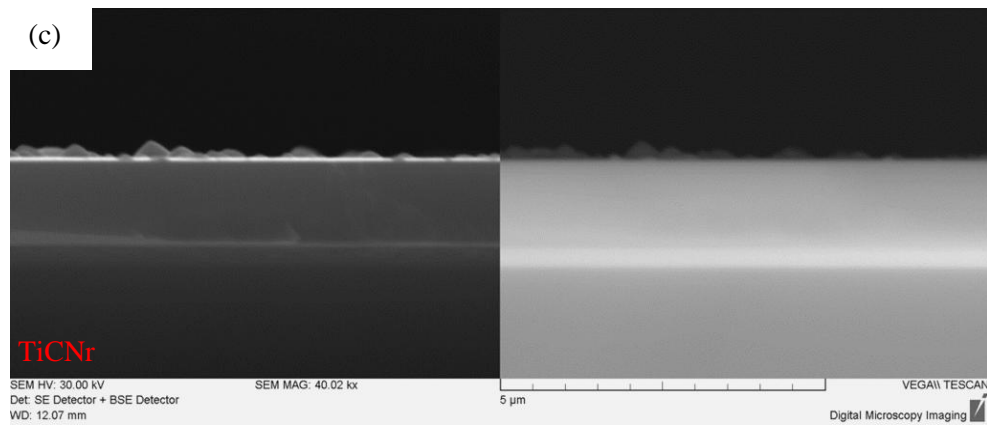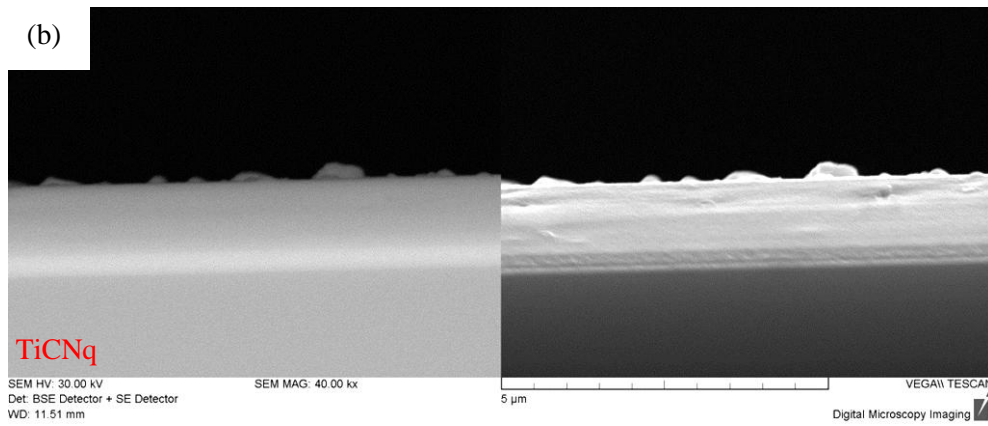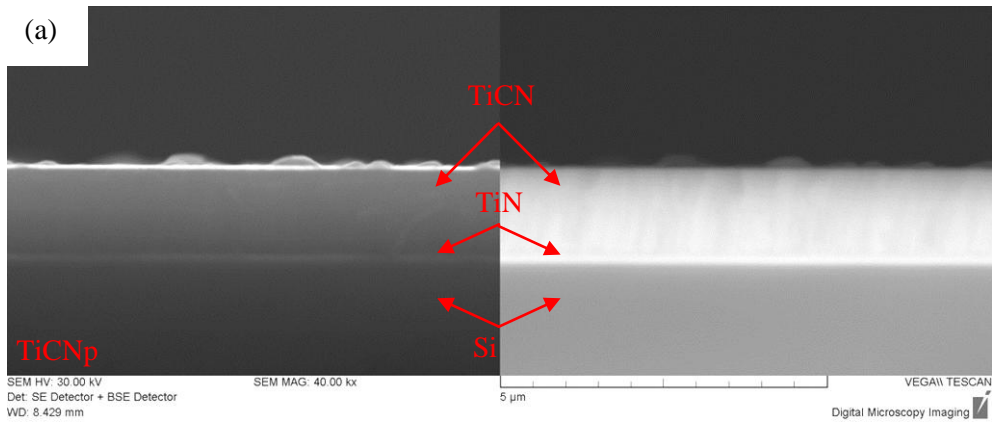
Figure 4.1 SEM cross-sectional images of samples (a) TiCNp, (b) TiCNq, (c) TiCNr and (d) TiCNs. The brighter image refers to BSE detector, wereas the darker one to the SE image.

A compact and featureless structure is visible in all TiC coatings (Figure 4.2a-c), suggesting the formation of a highly amorphous phase, as a consequence of the great amount of carbon incorporation (Table 3-7). Sample TiN (Figure 4.3), on the other hand, possesses a dense nanocolumnar structure, as expected from a stoichiometric coating composition.
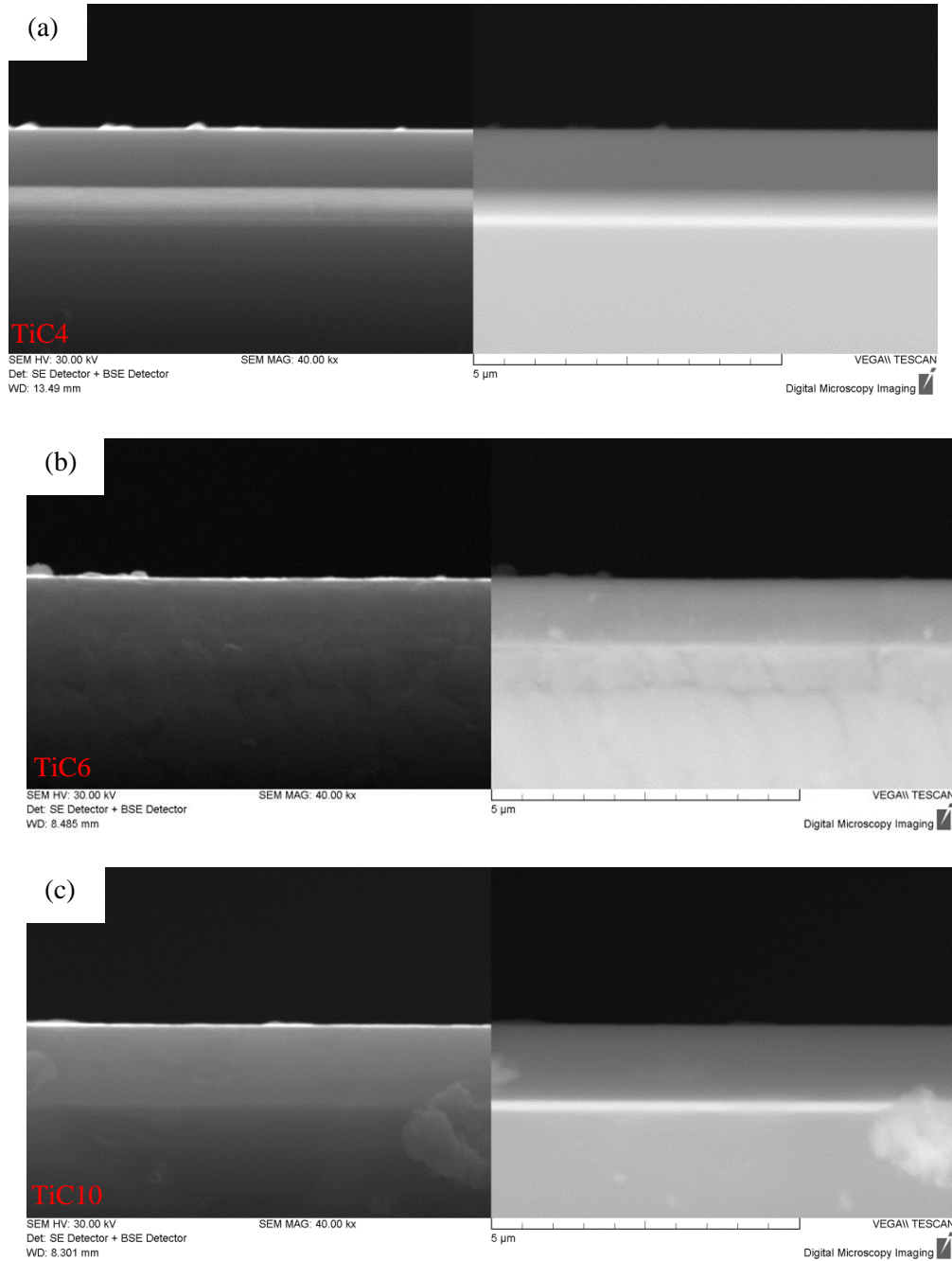

Figure 4.2   Cross-sectional SEM images of samples (a) TiC4, (b) TiC6 and (c) TiC10.
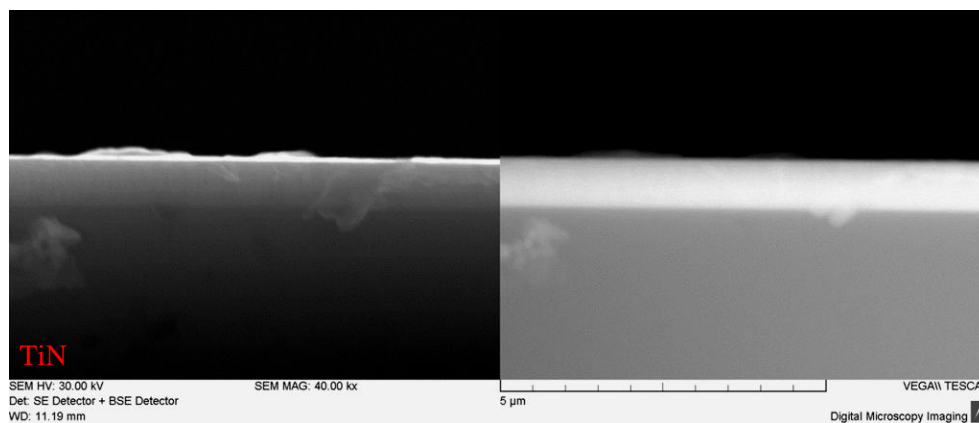
Figure 4.3   Cross-sectional SEM image of TiN sample.

4.2   **Compositional analysis**

We have just outlined how a good choice of the composition of TiC_xN_{1-x} films can greatly improve its mechanical and tribological properties. Optimal performances have been obtained with $TiC_{0.7}N_{0.3}$ [47], and with $TiC_{0.6}N_{0.4}$ [31] coating stoichiometry. In both cases, a high concentration of C seems to be the key parameter to obtain a combination of high hardness value and low friction coefficient.

Samples TiCNp, TiCNq, TiCNr and TiCNs has been deposited with a similar concentration to the set obtained through DC Magnetron Sputtering and RF bias by Restello and co-workers, in order to compare the two deposition techniques from the point of view of the effects of increasing carbon incorporation in the microstructural and mechanical properties.

4.2.1   **EDS and EPMA analysis**

Sample's composition has been measured by Energy Dispersive X-ray Spectroscopy (EDS) integrated in SEM apparatus at Veneto Nanotech labs. The energy of the electron beam was 7 keV, which is sufficient to collect the contribution of the heavier Ti species, as evidenced form the spectra of (Figure 4.4). Nevertheless, EDS is not well suited for the detection of lightest elements, due to the relative low spectral resolution in the low energy region, where there is a strong peak overlap that hinders a precise quantitative evaluation of relative elemental abundances (Figure 4.4).

The compositional information obtained from this technique is thus subjected to a great error contribution. If possible, more accurate quantitative analysis are needed, like Rutherford Backscattering (RBS), quantitative SIMS evaluation or EPMA analysis implemented with Wavelength Dispersive Spectroscopy (WDS) spectrometers.

EPMA and WDS techniques possess intrinsically higher spectral resolution and enhanced quantitative potential than EDS, enabling a better estimation of the atomic concentration of lighter element. Nevertheless, they were not easily accessible for the present research work: only TiC samples (Table 3-9) has been measured with this technique, thanks to a previous collaboration with a research group from Sevilla (ES).

Chemical composition of samples under study (Table 3-7, Table 3-8 and Table 3-9) obtained by EDS and by EPMA are reported in (Table 4-1), and are represented in a triplot diagram in (Figure 4.5). Oxygen has been included in the compositional evaluation to account for possible residual atmospheric gas contamination. Errors for EDS analysis has been evaluated as 20% over the total C and N content, and as 15% over Ti amount, whereas EPMA chemical compositions are subjected only to 10% indetermination.
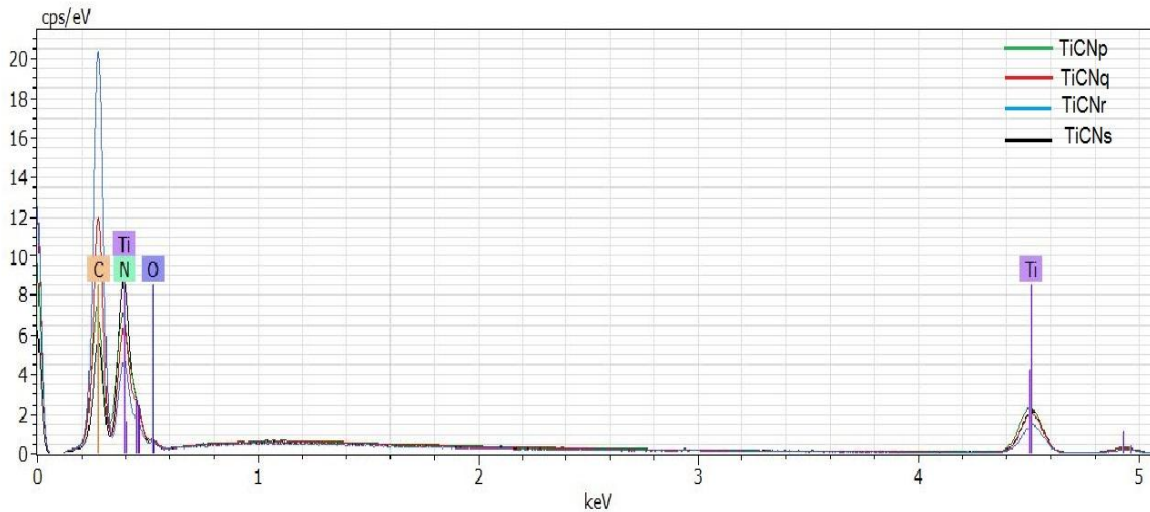
Figure 4.4   EDS spectra of samples of Table 3-7, obtained with an electron beam of 7 keV energy

Sample	Ti [at%]	C [at%]	N [at%]	O [at%]
TiCNp	50,7±7,6	31,4±6,3	17,5±3,5	0,3±0,1
TiCNq	40,4±6,1	42,3±8,5	16,1±3,2	1,3±0,2
TiCNr	24,8±3,7	60,6±12,1	13,5±2,7	1,1±0,2
TiCNs	48,5±7,3	22,5±4,5	28,7±5,7	0,4±0,1
TiN	45,4±6,8	3,5±0,7	49,3±9,9	1,8±0,3
TiC4	32,3±3,2	61,7±6,2	0	6,1±0,6
TiC6	11,5±1,2	86,4±8,6	0	2,1±0,2
TiC10	6,0±0,6	91,7±9,2	0	2,3±0,2

Table 4-1:   Chemical composition of samples under study obtained by EDS and EPMA analysis.
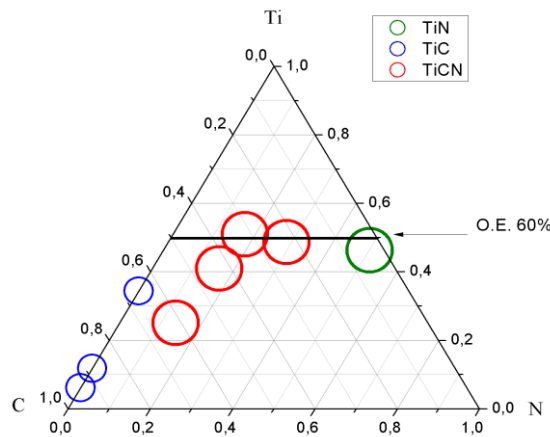

Figure 4.5   Triplot representation of sample's chemical composition. Circle radius represents the error contribition from EDS compositional measurement.

It was shown in the previous chapter how deposition parameters deeply influence coating characteristics, and in particular how a good control of the quantity and of the rate of introduction of reactive gas flows strongly act on its adherence properties.

In this research work, HiPIMS deposition process has been optimized to guarantee a good stability by choosing the appropriate power supply and impulse characteristics, as explained in the previous chapter. Nevertheless, it was not the only aim pursued: the most important finding is that, trough OES spectroscopy monitoring, we managed to reach a perfect control of the film

stoichiometry, and to predict the contribution of relative reactive gas flow on the global elemental incorporation. Indeed, we found that Ti and C content in the HiPIMS process can be related respectively to Ti 499nm emission line and H(656nm)/Ti(499nm) emission lines ratio (Figure 4.6), whereas the N/Ti ratio is determined primarily by the nitrogen flow.

In the previous paragraph, we analyzed the OE spectra recorded during deposition, and we found that, when increasing the acetylene flux, a higher fraction of C_2H_2 completely dissociates in gas phase (Figure 3.17b): the consequence, as demonstrated by compositional measurements, is that a major amount of C is incorporated in the coating structure; meanwhile, a higher number of H free atoms progressively fill the deposition chamber. Bearing in mind that OE set point of Ti line determines the amount of Ti incorporated in the structure, and that the poisoning action of nitrogen strongly influence the relative amount of Ti that, once sputtered, is free to react with C on the growing film surface, it is clear how the ratio between H and Ti emission line can be considered a key parameter to control C incorporation at constant value of nitrogen supply.

A prefect linear relation between H(656 nm)/Ti(499 nm) and both C concentration and C/Ti ratio has been found in those samples deposited with the same N_2 flux (Figure 4.6a,b). This finding demonstrates how constant time monitoring of emission lines is a powerful and simple tool to control film composition, and consequently film's mechanical properties. The predictive properties of gas flow monitoring open interesting possibilities in coating design, that is nowadays of fundamental importance in industrial protective superhard coating production.
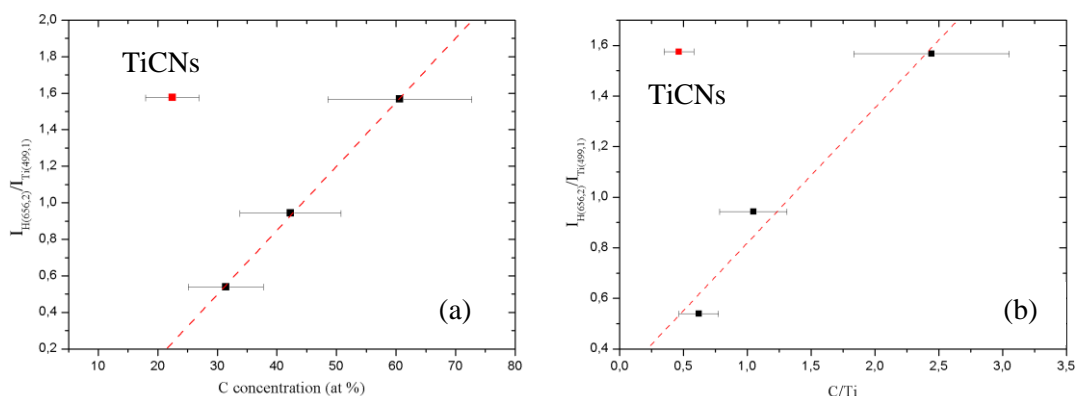

Figure 4.6   Evolution of H(656nm)/Ti(499nm) emission lines ratio as recorded trough OE monitoring as a function of (a) total C concentration and (b) C/Ti ratio.

4.2.2   SIMS quantitative depth profile

SIMS experiments were carried out at Department of Physics and Astronomy "Galileo Galilei" in Padova, using a CAMECA IMF-4f ion instrument. A Cs^+ primary ion beam of 5,5 keV impact energy was employed. The beam current was 149 nA, and the beam was rastered across an area of 200×200 μm (raster size). Positive secondary ions were accepted from a circular area of 30 μm diameter (field aperture). The mass resolution was about m/Δm≈300.

The recorded elements are Ti, N, C and O, all in the form of neutral atoms bounded to a positive cesium atom, MCs^+, as required by the RSF quantitative depth profile method summarized in paragraph 2.3. Oxygen level has been measured to account for some residual contamination from the atmosphere: residual O can be adsorbed on deposition chamber walls and plasma formation causes its subsequent desorption, favoring O capture by Si substrate during the deposition process.

All the intensity signals are expressed as a function of depth, after a calibration process that assumes a constant sputtering rate over all the raster thickness. SIMS profiles are reported in (Figure 4.7a-h), and from the distribution of the chemical components throughout the sample

72

thickness it is possible to confirm that all the deposited coatings posses a homogeneous monolayer structure; moreover, the interlayer Ti+TiN region and the transition to the Si substrate are clearly distinguishable.
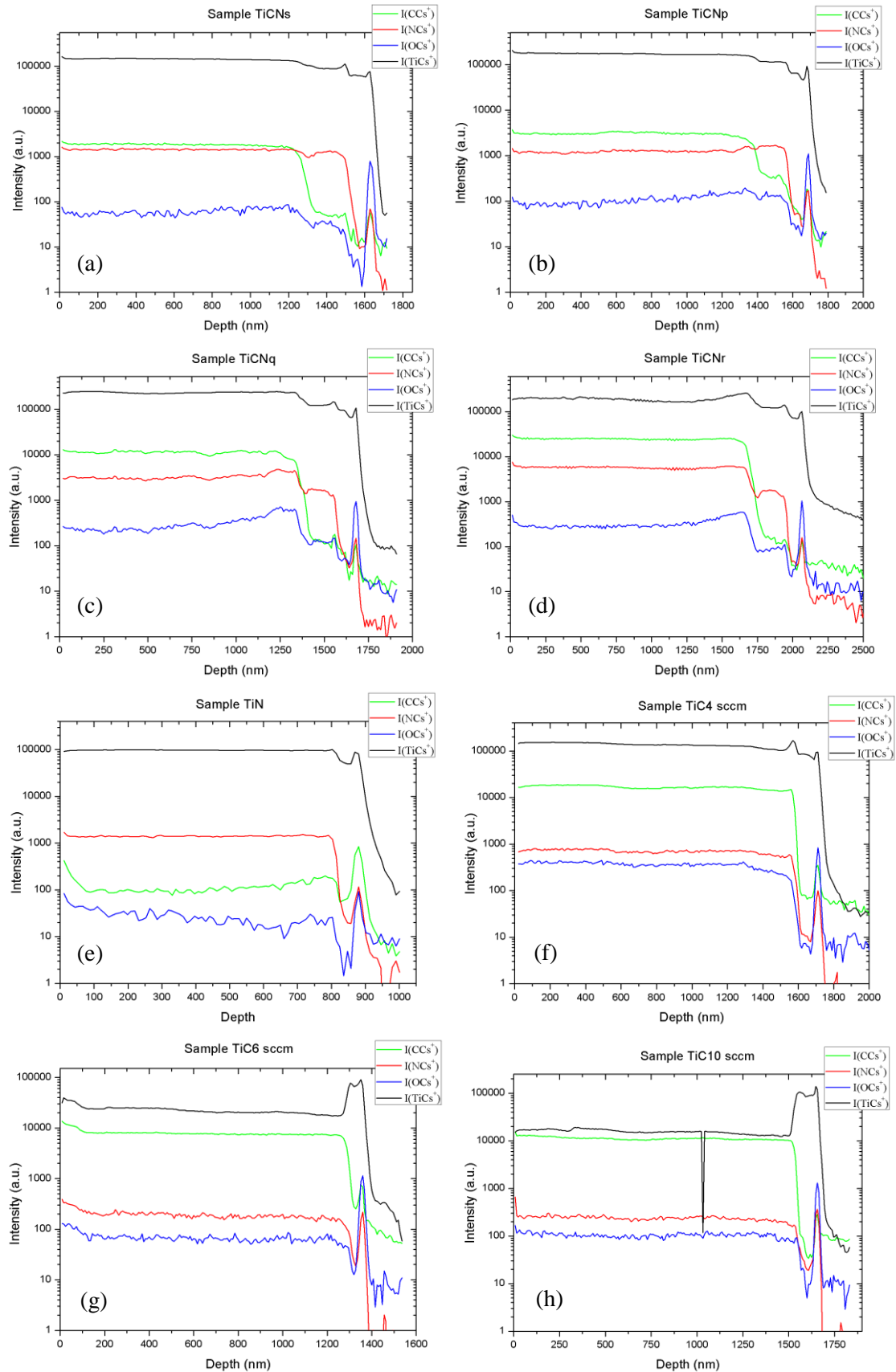

Figure 4.7   SIMS depth profile of MCs⁺ ions of TiCN (a-d), TiN (e) and TiC (f-h) coatings.

From SIMS profiles (Figure 4.7a-h), it is visible that, throughout all the samples' thickness, oxygen counts are very low, except at the interlayer-substrate surface where they exhibit a sensible enhancement, especially in TiC samples. It is thus possible that some unwanted TiO_2 compound is formed in the first interlayer atomic planes, thanks to the high affinity of these two elements. Moreover, N signal is visible also in TiC samples, with NCs^+ counts of the order of magnitude of OCs^+, demonstrating the possibility of a low N contamination during the deposition process of titanium carbides.

It is now presented the calibration procedure for the estimation of carbon and nitrogen content: for this purpose, TiC and TiN samples have been adopted as reference of known composition to construct the calibration lines. A fourth TiC sample deposited with C_2H_2 flux of 3,5sccm has also been measured (not shown).

CARBON

To construct the Carbon calibration line using the RSF method, the intensity ratio of the four TiC samples has been taken as a reference because their composition is known with a good accuracy from EPMA measurements.

The relative intensity $I(CCs^+)/I(TiCs^+)$ is an average over all the depth profile, and the medium values are listed in Table 4-2:

Sample	$I(CCs^+)/I(TiCs^+)$
TiCNp	0,0179
TiCNq	0,0179
TiCNr	0,1325
TiCNs	0,0128
TiN	0,0011
TiC3,5	0,0618
TiC4	0,1226
TiC6	0,3567
TiC10	0,7200

Table 4-2: Intensity ratio of CCs^+ over $TiCs^+$ counts of all the samples under investigation

The intensity ratio for the TiC samples is plotted in (Figure 4.8) as a function of concentration ratio c_C/c_{Ti} : note that the wide variability range of this last quantity enables the computation of a reliable calibration line and the extraction of the relative sensitivity factor needed for the quantitative compositional procedure (equation (2.1)).
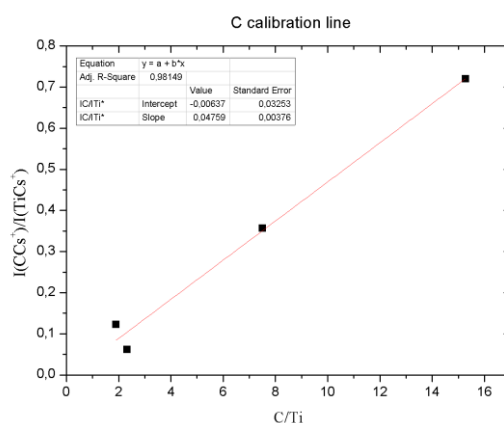

Figure 4.8 Linear fit of intensity ratio of SIMS signal over C/Ti concentration for TiC samples.

The results of the linear fit are:

$$RSF_C = 0,047 \pm 0,004 \quad b = -0,006 \pm 0,032,$$

where the intercept, b, is compatible with zero as expected.

In (Figure 4.9), relative intensity ratio $I(CCs^+)/I(TiCs^+)$ measured for TiCN and TiN samples is plotted against c_C/c_{Ti} concentration ratio obtained with EDS values (blue squares). These experimental points are superimposed to the SIMS calibration fitting previously calculated.
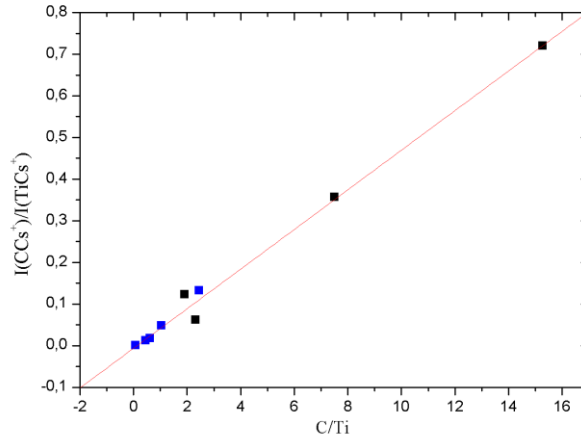

Figure 4.9   Relative intensity ratio $I(CCs^+)/I(TiCs^+)$ against concentration ratio C/Ti for TiCN and TiN samples, superimposed to the calibration line.

The linear relationship between SIMS and EDS data is greatly verified. If composition ratio c_C/c_{Ti}, as derived from quantitative SIMS depth profile, is compared with the reference data based on EDS analysis, deviations do not exceed 20%, except in the case of TiN sample, where a sensible overestimation of C quantity is observed (Table 4-3). This demonstrates the intrinsic limits of this technique to achieve reliable quantifications in case of very low elemental concentration.

Finally, if Ti concentration as extracted from EDS measurements is supposed to be correct, it is possible to evaluate C concentration in the film with the SIMS quantitative depth profile analysis data, that must be successively normalized to the total Ti and N global amount.

Sample	C/Ti from EDS	C/Ti from SIMS
TiCNp	0,62	0,51
TiCNq	1,05	1,15
TiCNr	2,45	2,92
TiCNs	0,46	0,40
TiN	0,08	0,16

Table 4-3: Compositional ratio C/Ti as obtained from EDS measurements and SIMS analysis

NITROGEN:

To evaluate nitrogen content a good standard reference of known composition is indeed lacking, because no EPMA measurements are available on TiN sample. Thus, a simultaneous calibration over all the investigated samples will be more correct.

The relative intensities ratio $I(NCs^+)/I(TiCs^+)$ are listed in Table 4-4, and are presented in function of concentration ratio N/Ti in (Figure 4.10):

Sample	$I(NCs^+)/I(TiCs^+)$
TiCNp	0,0071
TiCNq	0,0137
TiCNr	0,0306
TiCNs	0,0100
TiN	0,0144
TiC3,5	0,0039
TiC4	0,0052
TiC6	0,0086
TiC10	0,0153

Table 4-4: Intensity ratio of NCs^+ over $TiCs^+$ counts of all the samples under investigation.
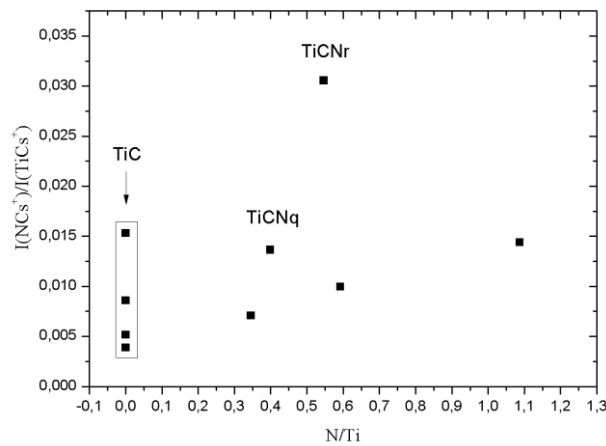

Figure 4.10   Relative intensity ratio $I(NCs^+)/I(TiCs^+)$ against concentration ratio N/Ti for TiC, TiCN and TiN samples.

It is clearly visible from (Figure 4.10), that the linearity between SIMS intensity signals and compositional values is not respected, making impossible the application of RSF linear interpolation method (equation (2.1)), and thus nitrogen quantification.

The great discrepancy between relative intensity ratios of different samples is ascribed primarily to their different degree of cristallinity, even if it is not well understood why this effect is not visible also for carbon estimation.

As reported in literature [73], a remarkable decrease in sputtering yield of single and polycrystalline metals in focused ion beam technology is observed as a consequence of channeling: this phenomenon occurs when the ion beam is directed in parallel to a low-index crystallographic axis or plane, leading the formation of a real channel for the incoming ion, that can travel large distances into the material before making collisions and releasing its energy. Thus, due to channeling, a large number of ions do not contribute to the material removal and sputtering yield is reduced.

On the other hand, sputtering yields of amorphous targets may be similar or even higher than the corresponding single metal or metal-carbide polycrystals, as reported by Sigmund and references therein [74].

The degree of crystallinity of samples under study was evidenced by SEM cross-sectional images in paragraph 4.1: we remind that samples TiCNp, TiCNs and TiN appear polycrystalline, whereas TiCNq, TiCNr and TiC coatings have a remarkable amount of amorphous phase, due to the increase of carbon incorporation in film structure.

From (Figure 4.10) and Table 4-4 it is evident a decreasing trend in the relative intensity ratio with the transition from an amorphous phase to a more ordered and crystallized structure, both for TiC (black vertical box on the right) and TiCN samples.

The hypothesis of channeling may not apply to the samples under study because, even if a diminution in sputtering yield of NCs^+ is observed according to the crystalline degree of the coating, this trend is not observed for the other elements. As a consequence, the anomalous behavior of nitrogen may be attributed to a specific dependence of nitrogen sputtering yield to the crystal degree of the samples, but further investigation are needed to confirm this hypothesis.

This observation highlight the importance of crystal degree in ion beam technology, and demonstrate that RSF method for quantitative SIMS analysis is only applicable within samples of similar crystal structure.

In order to improve the evaluation of coating's chemical composition, also RBS measurements were performed at National laboratories of Legnaro, Padova. However, no results were available because the ion probe wasn't sufficiently energetic to penetrate the whole TiCN coatings' thickness, thus enabling the quantification procedure.

Because all alternative compositional analysis has failed with titanium carbon nitride coatings under study, we will consider therein the chemical compositions obtained with EDS measurements (Table 4-1).

4.3 Structural analysis

Microstructural design is the most widely used technique chosen for the production of coatings with superior mechanical and tribological properties. It is thus necessary to well understand the structure of the TiCN films under study, and to relate their global properties to the deposition parameters.

4.3.1 Raman spectroscopy

In order to investigate the properties of amorphous phase present in titanium carbon nitride coatings, Raman spectroscopy was performed at LaNN laboratories, a Veneto Nanotech laboratory in Padova, using a Melles Griot argon laser with excitation wavelength 514,5 nm. This system is coupled to a confocal microscope, so that the excitation beam can probe the sample surface with three dimensional spatial resolution. The backscattered light is collected by the same focusing objective and filtered in order to remove the excitation wavelength. The remaining signal is analyzed by a spectrometer and a CCD sensor.

This is called a confocal configuration, and its advantage is that only the near surface of the sample is correctly focused, enabling a high depth selectivity that can completely exclude noise signals from the substrate.

Moreover, particular care has been taken in the focusing process of the laser on the film surface, in order to minimize background interference.

Measurements were carried with two power regimes: once observed that in the higher energy regime Raman spectra were not distorted by local heating effects, with respect to low power supply, we decided to analyze these signals, thanks to their better visibility and lower ground noise.

<u>TiCN SAMPLES</u>:

A superposition of the recorded spectra for TiCN coatings is reported in (Figure 4.11), from which it can be noticed that Raman spectrum of a-C and a-CN phase is hardly visible in the typical region 800-2000 cm^{-1} for samples TiCNp and TiCNs. Instead, D and G peaks have been recorded for samples TiCNq and TiCNr, which were expected to possess an amorphous phase after the morphological analysis presented in paragraph 4.1.
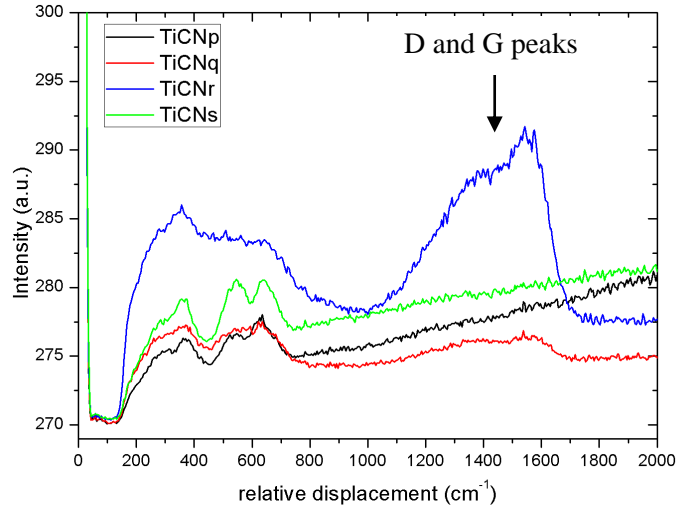

Figure 4.11   Raman spectra of TiCN samples obtained at maximum excitation beam power.

On the contrary, an interesting peak broadening evolution is clearly visible in regions 200-350 and 500-700 cm^{-1}, and this signal is attributed to acoustic and optical vibrational modes of titanium nitrite/carbide respectively, as reported also in literature [35,61].

The progressive broadening of these phononic peaks evidenced in (Figure 4.12a), is a clear demonstration of a progressive loss of crystal order in the TiCN structure with increasing the C incorporation (i.e. form sample TiCNs to sample TiCNr). At the same time, the signal from D and G Raman peak progressively appears, indicating the growth of an amorphous C-C or C-N structure (Figure 4.12b).
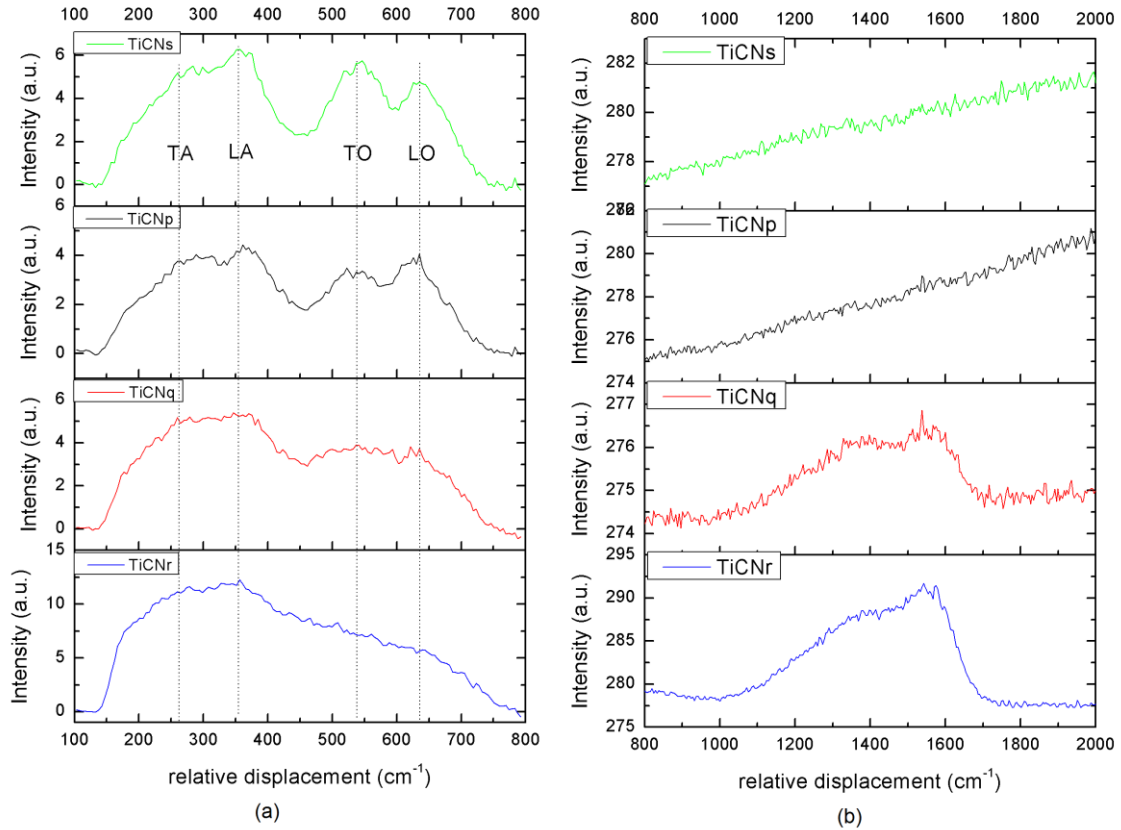
Figure 4.12   Raman spectra of samples TiCN renormalized with a straight line subtraction in regions (a) 100-800 cm^{-1} and (b) 800-2000 cm^{-1}.

After a renormalization procedure realized with a straight background line subtraction, G and D peaks were fitted with two Gaussian curves, in order to extract their peak position, as well as peaks FWHM. The fitted curves are presented in (Figure 4.13) for samples TiCNq and TiCNr respectively, and interpolation results are presented in (Table 4-5).

Evolution of G position towards higher displacement values with increasing carbon content is compatible with a stage 2 material with sp^3 fraction less than 20%, in accordance with the three-stage model proposed by Ferrari and coworkers [60] for carbon nitrides systems (Figure 2.19).

The dimension of Raman active clusters has been evaluated through equation (2.10), because in stage 2 the TK equation (2.9) is no longer valid [59].
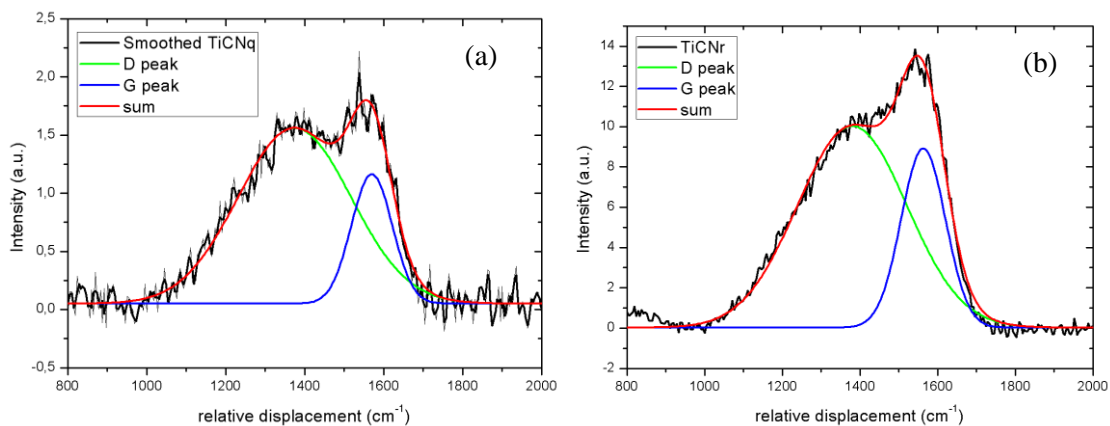

Figure 4.13   Raman spectra of (a) TiCNq and (b) TiCNr coating in region 800-2000 cm^{-1}. D and G peak are fitted with two Gaussian curves.

79

Sample	I(D)/I(G)	G position [cm^{-1}]	G FWHM [cm^{-1}]	L$_a$ [Å]
TiCNq	1,35	1570	103,3	15,7
TiCNr	1,12	1563	114,3	14,3

Table 4-5: Results of fitting procedure of D and G peak with two Gaussian curves and successive elaboration.

From this Raman analysis it is possible to identify a general evolution of the coating's structure with the C and N concentrations, in accordance with the model proposed by Ferrari et al [60]. In samples deposited at 60% OE, namely TiCNp and TiCNs, the phonon's mode spectrum typical of an ordered crystal lattice is predominant, whereas D and G peaks are not recorded, supporting the hypothesis that C atoms are linked in a TiCN lattice rather than form C-C bonds in an amorphous phase.

Meanwhile, in samples with decreasing OE set point (i.e. TiCNq and TiCNr) Raman Disordered and Graphtic peaks are well visible, while the phonon mode region become progressively broader and less pronounced (Figure 4.12).

From the analysis of I(D)/I(G) ratio it is possible to infer that the crystalline structure suffers a progressive amorphization with increasing C/N ratio, but it is not possible to relate the sp^3 concentration with a specific value of sp^2 bonds, due to the non linearity between these two quantities in carbon-nitrides materials [60]. Not even it is possible to determine whether the major contribution in amorphous phase comes from C-N or simply C-C bonds, because more specific analysis with different excitation wavelength is needed.

We recognize that TiCN coatings behaves as stage two systems, and are classifiable as a-C:H:N films because they have been deposited with a reactive sputtering technique with hydrocarbon gas (Figure 2.18), and are thus expected to present a hardness enhancement with increasing nitrogen concentration, as foreseen by literature studies [60,75].

TiC SAMPLES:

Raman analysis have been performed also on TiC samples, as a consequence of their high amount of C content, which is expected to produce the formation of an amorphous matrix.

Also in this case, spectra obtained with maximum power supply to the laser probe have been analyzed, after ensuring that this will not cause damage or amorphization of the coatings.

The recorded spectra are represented in (Figure 4.14) and fitting results are reported in (Figure 4.15 and Table 4-6). With carbon systems, it is not always clear if the I(D)/I(G) ratio should be the ratio of the peak heights or peak areas. The difference is not so important for disordered graphite, as the peak widths are similar, but this is not so for amorphous carbons. In that case, the broadening of the D peak is correlated to a distribution of clusters with different orders and dimensions, and thus the information about the less distorted aromatic rings is in the intensity maximum and not in the width, which depends on the disorder. Ring orders other than six tend to decrease the peak height and increase its width [59]. In this work we refer to I(D)/I(G) as the ratio of peak heights.
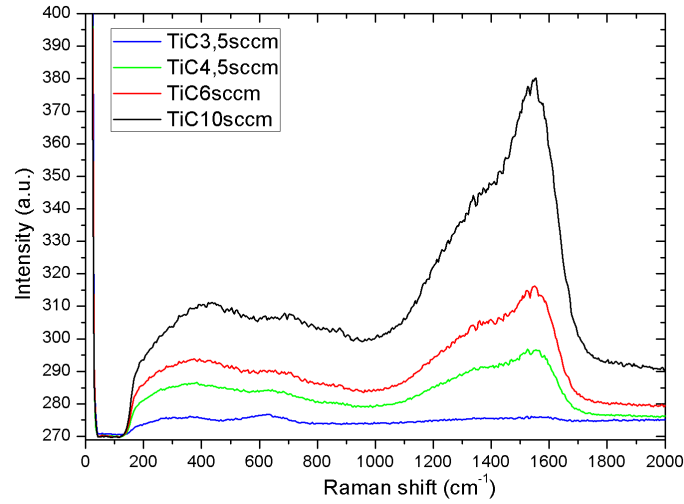
Figure 4.14   Raman spectra of TiC samples obtained at maximum power of the exciting beam.
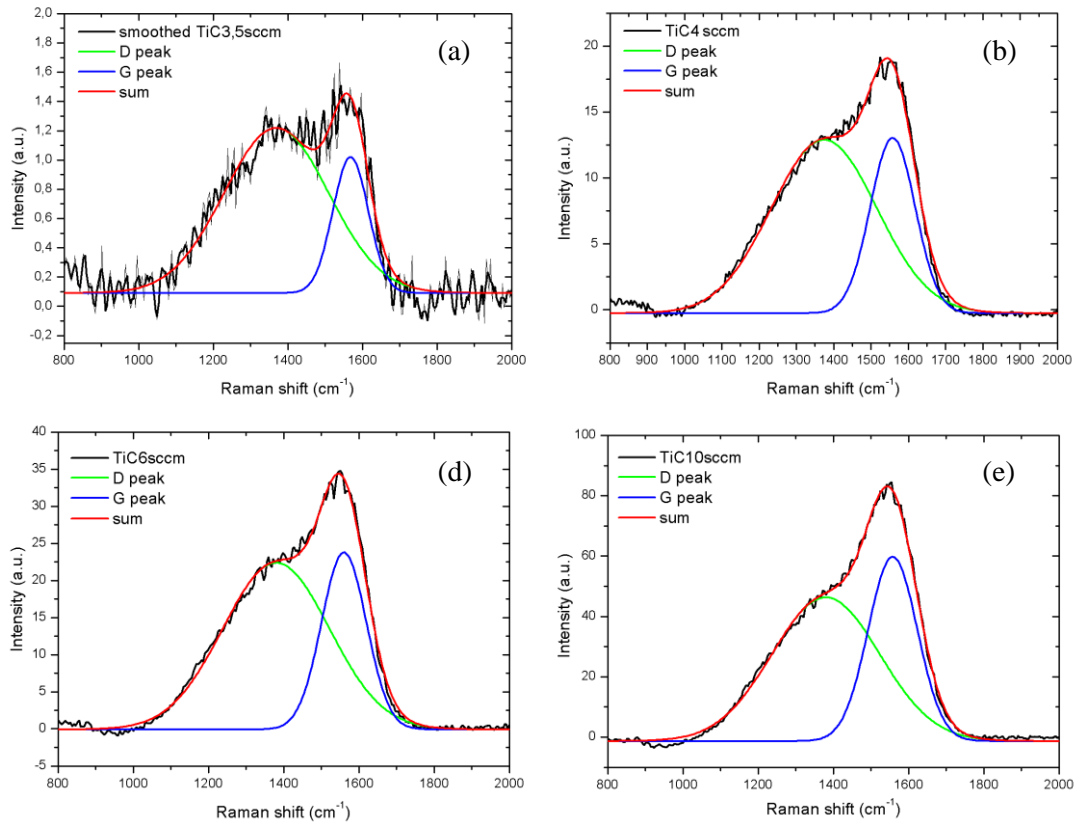

Figure 4.15   Raman spectra of (a) TiC3,5, (b) TiC4, (c) TiC6 and (d) TiC10 coatings in region 800-2000 cm^{-1}. D and G peak are fitted with two Gaussian curves.

Sample	I(D)/I(G)	G position [cm^{-1}]	G FWHM [cm^{-1}]	L$_a$ [Å]
TiC3,5	1,21	1568	95,1	14,8
TiC4	0,99	1558	120,8	13,4
TiC6	0,94	1560	119,3	13,1
TiC10	0,78	1557	130,8	11,9

Table 4-6: Results of fitting procedure of D and G peak with two Gaussian curves and successive elaboration.

81

From (Figure 4.14) a great enhancement of D and G peak intensities is observed with increasing acetylene flux, as a consequence of the progressive amorphization of the coating's structure, which increases the amount of sp^2 structures.

The 200-800 cm^{-1} signal is not imputable nor to TiC characteristic phonon lattice vibrations, because of the great amorphous content and the nanometrical grain size expected, nor to a TiO_2 contribution, coming from the impurity layer formed at the interface with the substrate (as observed by SIMS analysis in paragraph 4.2.2), because Raman peaks are not compatible with the one expected for anatase phase. They are thus probably a background spurious contribution.

As reported in (Table 4-6) and as depicted in (Figure 4.16), G peak position shifts from 1568 to 1557 cm^{-1} and the ratio I(D)/I(G) decreases progressively to lower values with raising the acetylene flux (i.e. the total carbon content). These features are typical of a two stage carbon system, in accordance with the model proposed by Ferrari et al. [59]. This stage corresponds to a microstructural transition from nanocrystalline graphite to sp^2 a-C, with a concentration of disordered sp^3 bonds less than 20%. Nevertheless, the deposition performed with hydrocarbon gas, as is the case for our samples, lead to a great hydrogen incorporation in the coating's structure. As mentioned in paragraph 2.4.2, the three stage model is still valid for hydrogenated samples, and the effect of H incorporation is a general increase in sp^3 content as a consequence of H saturation of C=C bonds as $\equiv CH_x$ groups.

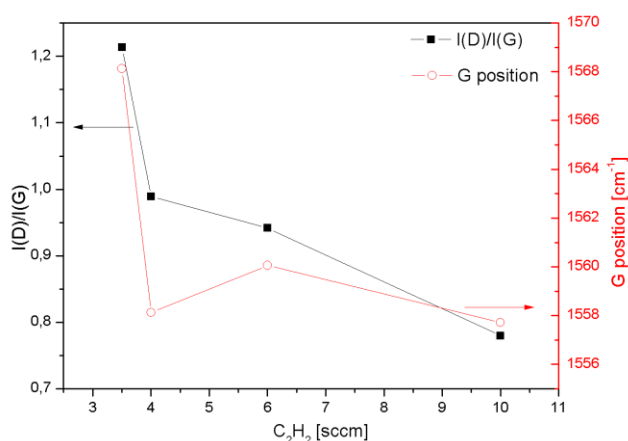*Figure 4.16   Simultaneous representation of intensity peak ratio I(D)/I(G) (black line) and G position displacement (red line) with acetylene flux for TiC samples.*

4.3.2   X-ray diffraction analysis

Crystal microstructure, lattice parameter and grain size of TiCN coatings deposited on Si substrates has been investigated trough X-ray diffraction. Samples have been measured by Philips X'perts PANalytical MRD diffraction instrument at the department of Physics and Astronomy "G.Galilei" in Padova. The instrument works with four goniometers in a Bragg-Brentano configuration represented in (Figure 4.17).
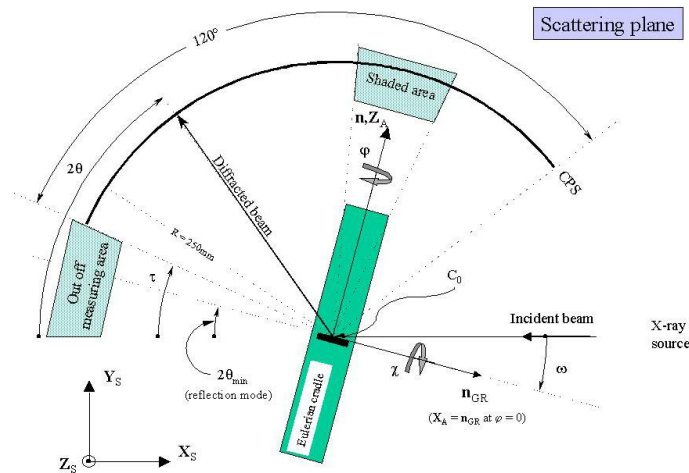
Figure 4.17   Schematic representation of the diffraction instrument in a four circle reflection geometry [56]

Four different rotations can be distinguished (Figure 4.17):

-    ω is the angle of the incident beam with respect to the sample's surface. It represent a rotation around Z_S (sample's reference frame)

-    2θ is the angle between the incident beam direction and the diffracted one.

-    χ describes a rotation around one sample's surface axis , it is called co-latitude or pole-distance.

-    ϕ is the azimuth angle and represent a rotation of the sample around its normal Z_S.

The instrument was equipped with a parabolic mirror, a 1/32° slit to collimate the incident Cu kα X-ray beam on the sample's surface, and a system of soller silts (i.e. parallel plate collimators) in front of the detector to limit the vertical divergence of the diffracted beam. Samples were mounted on a Plexiglas support in order to exclude possible spurious reflections from a metallic sample holder.

Samples were measured in two different configurations: (a) at grazing incidence (GIXRD), with a fixed ω=0,5° incident beam angle and performing a 2θ scanning from 20° to 80°; (b) in a θ-2θ configuration, with a mirrored variation of the incident and the detection angle, for different azimuthal (ϕ) and co-latitude (χ) positions. This last configuration was chosen to obtain spectra for a combined texture analysis, and particular care has been adopted to impose an adequate acquisition time, in order to record spectra with a good statistics and low background.

It is known [56] that a measured diffraction spectra can be mathematically described as a convolution product between the "true" sample profile, $f(2\theta, \chi, \phi)$, and an instrumental function $g(2\theta, \chi, \phi)$. This latter is a peak function characterized by a given width Δ. The smaller the Δ, the better the resolution of the diffractometer. For the purpose of characterizing the instrumental contribution to the line broadening of the diffraction peaks, a polycrystalline Si standard has been measured at the same grazing incidence and also θ-2θ configurations of the TiCN samples.

The instrument resolution function is determined by the simultaneous presence of three major error components:

i.   purely geometrical errors, like beam divergence, collimator slit widths, optics misalignments, the non punctuality of the source, etc.

ii.   aberration contributions, like for example the defocusing effects at large *2θ*, roughness of the surface that may reduce the intensity of low angle peaks, etc.

iii.   physical effects, caused by a non monochromatic beam, problems of high background due to sample dimensions that are smaller than the X-ray beam, etc.

These contributions to line broadening can be described by three Cagliotti parameters *(U,V,W)* that represent the angular variation of the full width at half maximum (Δ) of the peaks according to the relationship:

$$\Delta^2 = FWHM^2 = U \tan^2 \theta + V \tan \theta + W \qquad (4.1)$$

It can be observed that this broadening contribution raise with increasing *2θ* diffraction angles. From the analysis of Si standard it was possible to calculate (*U,V,W*), and to set them as fixed instrumental parameters for all the successive analysis.

Diffraction spectra have been analyzed using MAUD software (http://www.ing.unitn.it/~maud/), in which it is implemented the complete Rietveld method for structure refinement [56]. In addition, it is possible to combine this analysis with a complete texture model (the WIMV method or its extended version, e-WIMV [76]) and to refine simultaneously crystal structure and microstructural parameters accounting for effects of preferential orientation. The mathematical details of this method are given in appendix A.

4.3.3   GIXRD

As a first step, all the samples were characterized by Grazing Incidence X-Ray Diffraction (GIXRD). The advantage of this approach is that it allows for the fast collection of good spectra with excellent signal – to noise ratio. In this way, the phases present in the film can be verified and a first estimation of the microstructural parameters can be obtained. However, the presence of macroscopic stress and texture may hinder these results and must be taken into account, as it will be done in next paragraph.

The results from GIXRD spectra analysis are now presented (Figure 4.18): simple Rietveld method has been adopted for the determination of crystal structure, microstructural effects has been modeled considering isotropic strain and particle size, and no texture contribution was added. The starting phase for the refinement is TiN because, as reported in literature [44], TiCN can be considered primarily a TiN lattice, in which C replaces N sites. Moreover, the structure factor of the two compounds is very similar, due to the small difference in the atomic number of N or C.
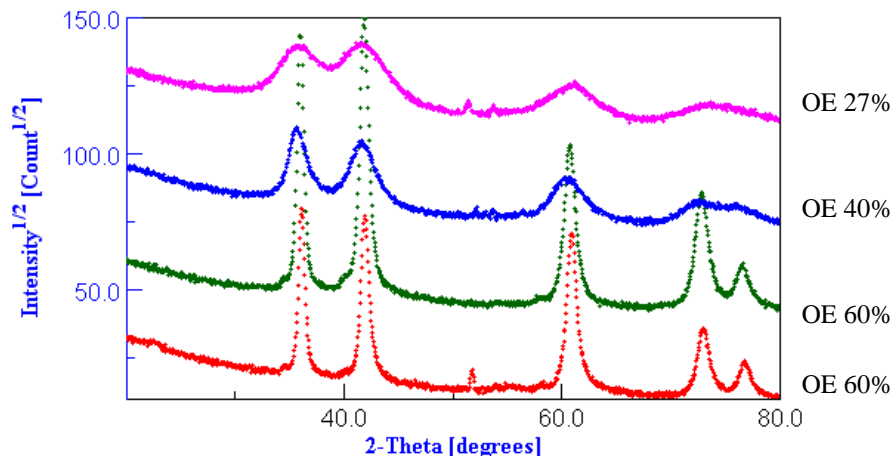

Figure 4.18   Superposition of GIXRD spectra of samples TiCNs (red), TiCNp (green), TiCNq (blue) and TiCNr (purple). Carbon content raise from bottom to top.

As these measures are performed in a grazing angle condition with fixed ω, the experimental intensities have to be divided by a factor J:

$$J = \frac{I_{GI}}{I_{sym}} = \frac{2}{1 + \dfrac{\sin(\omega)}{\sin(2\vartheta - \omega)}},$$
(4.2)

to take into account the variation of the beam intensity due to geometric effects. This procedure enables to analyze the experimental spectra as if they were obtained in a standard θ-2θ scan, and so to compare the experimental data to the software's simulation.

In some cases, additional peaks assigned to Si substrate appeared around 2θ≈50° consequently, the surrounding region has been excluded from spectrum computation.

During the analysis, five parameters were refined:

- Lattice parameter
- Crystal size
- Microstrain
- N site occupancy probability
- Debye-Waller factor, B, which describes the thermal vibrational motions of atoms around their specific lattice position. In general it is dependent on atom's nature and on the chemical bond of the structure, but for simplicity it was considered equal between Ti and N atoms with a good approximation. Its effect is a generalized lowering of diffraction peak intensity, due to the local variation of lattice bond induced by vibration.

Crystallite dimension and microstrain are evaluated simultaneously through Sherrer's equation (2.3) or similar more sophisticated methods implemented in the analysis software. All the obtained parameters are resumed in (Table 4-7). Henceforth, sample analysis will be presented in order of increasing carbon incorporation in the structure, namely with decreasing OE set point (Table 3-7): starting from TiCNs (22,5 at% C), passing to TiCNp (31,4 at% C), TiCNq (42,3 at% C) and finally to TiCNr (60,6 at% C).
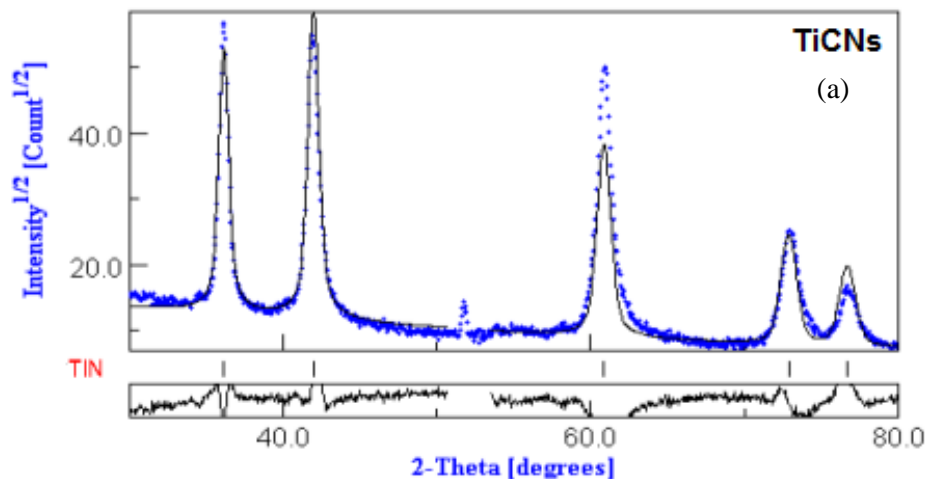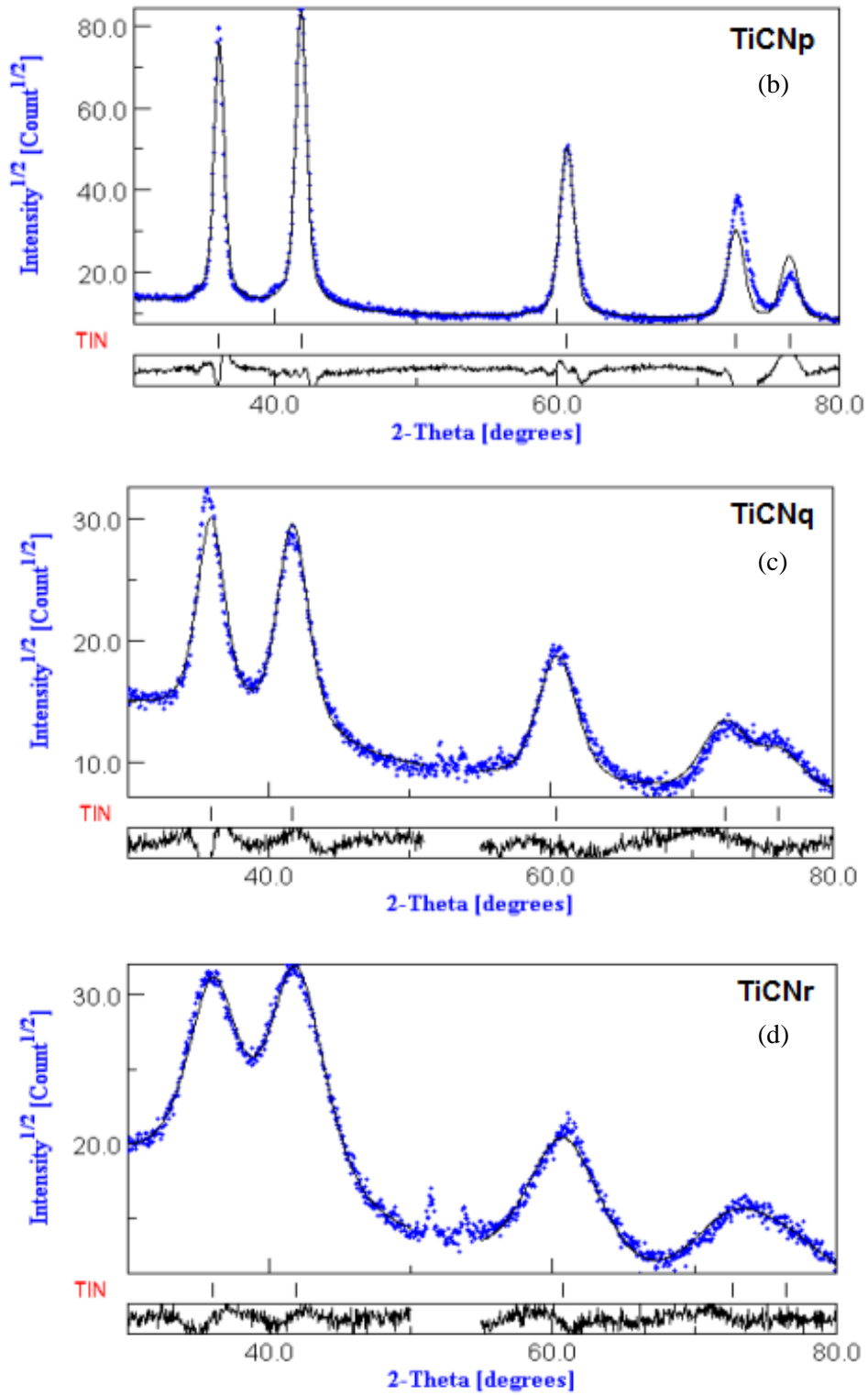
Figure 4.19   Results of software's simulation of GIXRD diffraction spectra of samples (a) TiCNs, (b) TiCNp, (c) TiCNq and (d) TiCNr. Peaks position of the TiN phase are also indicated, as well as a the variance between experimental data and simulation (black line on the bottom of every spectrum).

Sample	Lattice parameter [Å]	Crystal size [nm]	Microstrain	B	N occupancy
TiCNs	4,3003±0,0003	30,4±1,4	0,0036±0,0002	1,0±0,1	0,86±0,02
TiCNp	4,3107±0,0002	34,5±1,2	0,0044±0,0001	1,7±0,1	0,87±0,01
TiCNq	4,3285±0,0007	6,9±0,2	0,0117±0,0004	1,5±0,1	0,71±0,01
TiCNr	4,3114±0,0008	3,5±0,1	0,0212±0,0007	1,3±0,1	0,82±0,01

Table 4-7: Results of Rietveld simulation over TiCN samples.

From a first straightforward observation of experimental spectra (Figure 4.18), it can be noticed a substantial diminution of the diffraction peaks intensity and a parallel broadening of the width of diffraction peaks with the reduction of the Optical Emission set point level. These effects could be ascribed to three main causes: (i) a progressive amorphization process of the coating's structure, for which Bragg's Law (2.2) is no longer valid due to the loss of crystal order; (ii) diminution of grain size with increasing the amount of C incorporation in the structure (Figure 4.20a), that hinder grain growth and produce the formation of the amorphous matrix [41]. (iii) Rising of internal microstrain with increasing the C content (Figure 4.20b), probably due to localized strain gradient caused by both substitutionally bonded carbon atoms in the TiN lattice [44], or excess C assembling at grains boundaries [41]. It must be noticed that in samples TiCNs and TiCNp, which are thought to be perfectly polycrystalline after Raman analysis, carbon is found only in substitutional position in crystal lattice. Its effect is, in any case, to produce more stress in TiN structure due to the larger atomic radius of carbon with respect to nitrogen [44].
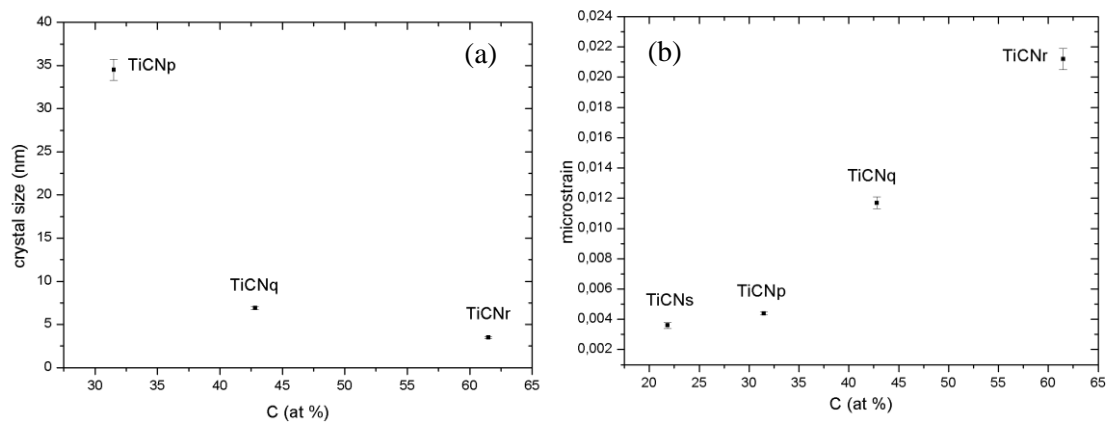

Figure 4.20   Evolution with the total amount of C concentration in the coatings of (a) crystal size and (b) microstrain, as evaluated from computations of GIXRD spectra.
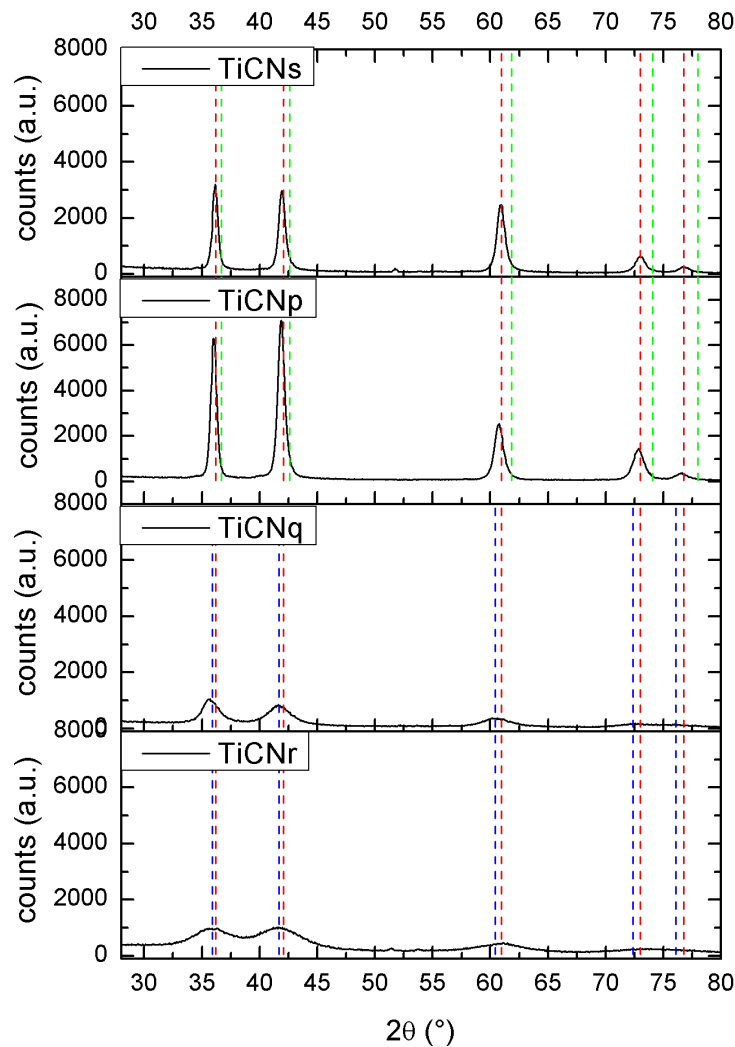
Figure 4.21 Superposition of GIXRD experimental spectra. Vertical lines referred to the diffraction peak positions of TiC (blue line, PDF #00-032-1383), $TiC_{0.7}N_{0.3}$ (red line, PDF #00-042-1489) and TiN (green line, PDF #00-038-1420).

From X-Ray diffraction spectra it is also possible to recognize the stoichiometry of diffracting phase from a matching of experimental and tabulated peak positions. In (Figure 4.21) TiC, TiN and $TiC_{0.7}N_{0.3}$ diffraction lines, as tabulated from PDF standards, are superposed to the measured GIXRD spectra. It can be noticed a progressive shift towards lower Bragg's angles with respect to TiN phase (green line), due to the expected increase in lattice parameter. In general, $TiC_{0.7}N_{0.3}$ (red line) and TiC (blue line) phases accurately match the experimental diffraction peaks.

Furthermore, some important considerations can be drawn observing the results of simulations obtained by Rietveld analysis. In particular, the fitting performed on stoichiometric samples (Figure 4.19a,b) show a strong intensity mismatch of different sign over all diffraction peaks. This effect couldn't be completely described through the free parameters of the simulation (in particular N site occupancy and the Debye-Waller factor) because they couldn't change relative intensities of the diffraction peaks. This indicates that B and N site occupancy obtained from the simulation are not completely reliable.

This change in relative intensity is indeed a clear evidence of preferred orientation. To evaluate this effect, Texture Coefficient (TC) has been calculated in accordance to equation

(2.7), and two different standard references has been adopted, because the real stoichiometric composition is not perfectly known. (Figure 4.22a) represent TC calculated with $TiC_{0.7}N_{0.3}$ standard reference (PDF #00-042-1489), whereas in (Figure 4.22b) standard is $TiC_{0.3}N_{0.7}$ (PDF# 00-042-1488).

A preferred [111] texture is visible in all samples, but it becomes less dominant with increasing carbon content (black squares). On the contrary, [200] and [220] orientations present quite textureless values (i.e TC≈1), except for sample TiCNs, for which a high [220] TC values probably indicates the presence of a more fiber structure. It must be highlight as the general trend doesn't differ with stoichiometry, indicating that this is not a compositional effect, but a fully texture behavior.

One last consideration that can be made observing diffraction peaks at high 2θ values in (Figure 4.19) is a small discrepancy in 2θ position between simulated and experimental peaks. This is probably an effect of internal macrostress that produces local changing in interplanar spacing, but is not directly evaluable from GIXRD measurements.
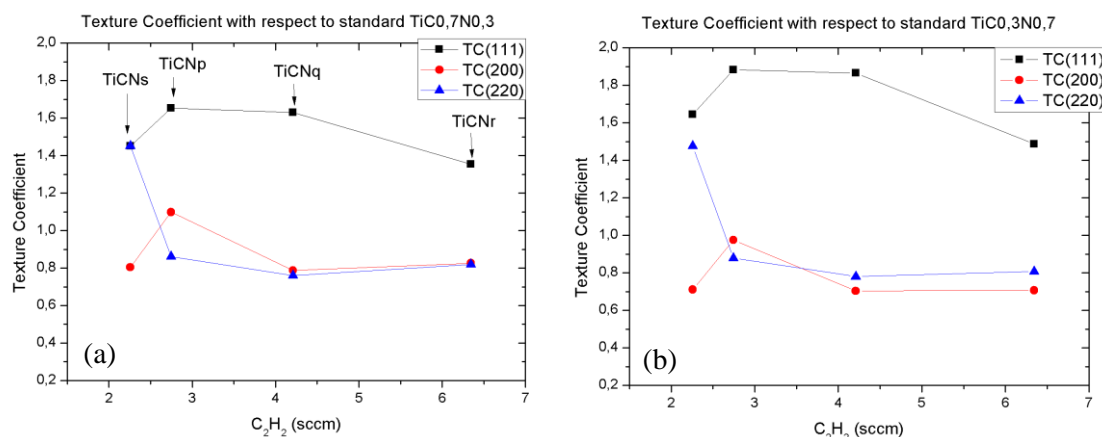

Figure 4.22   Evolution of Texture Coefficient of the first three diffraction peaks (namely [111], [200] and [220]) of TiCN samples, in function of the total acetylene flux. TC has been calculated taking as standard reference (a) $TiC_{0.7}N_{0.3}$ and (b) $TiC_{0.3}N_{0.7}$.

4.3.4   Combined Stress – Texture Analysis

In order to characterize crystal structure taking into account the effects of preferential orientation and internal macrostress, more precise diffraction measurements have been carried out in a θ-2θ configuration investigating multiple angular positions.

In particular, sample cradle has been rotated around its horizontal axis at step of 15° starting from χ=10° to χ=70°. For each co-latitude χ position, 18 different spectra have been recorded, varying the azimuthal angle from ϕ= -180° to ϕ= 180° with 20° steps. A good angular mapping of several diffraction directions is needed to reconstruct sample's Pole Figure (PF), that is a plot of the orientations of a given plane normal (pole) with respect to the sample reference frame. Moreover, it is possible to extract also Inverse Pole Figures, which show how a selected direction in the sample reference frame is distributed in the reference frame of the crystal. [2]

The analysis is carried on simultaneously on all the spectra collected at different (χ,ϕ) positions, as in this way effects related to texture and macrostress can be properly measured. The starting phase has been changed from TiN to TiC, because TiC diffraction lines seem to better reproduce samples' peaks positions, as shown in (Figure 4.21).

---

[2] See appendix for a precise mathematical definition of Pole Figure, and for the construction mechanism of Inverse Pole Figures.

For every sample the data are presented as a 2D multiplot (Figure 4.23a-d) which show the θ-2θ scan for different (χ,φ) combinations. Experimental data are compared with simulated diffraction intensities, and 2D difference plot between the simulated and the real measurements of each diffraction spectrum are also reported (Figure 4.24a-d).
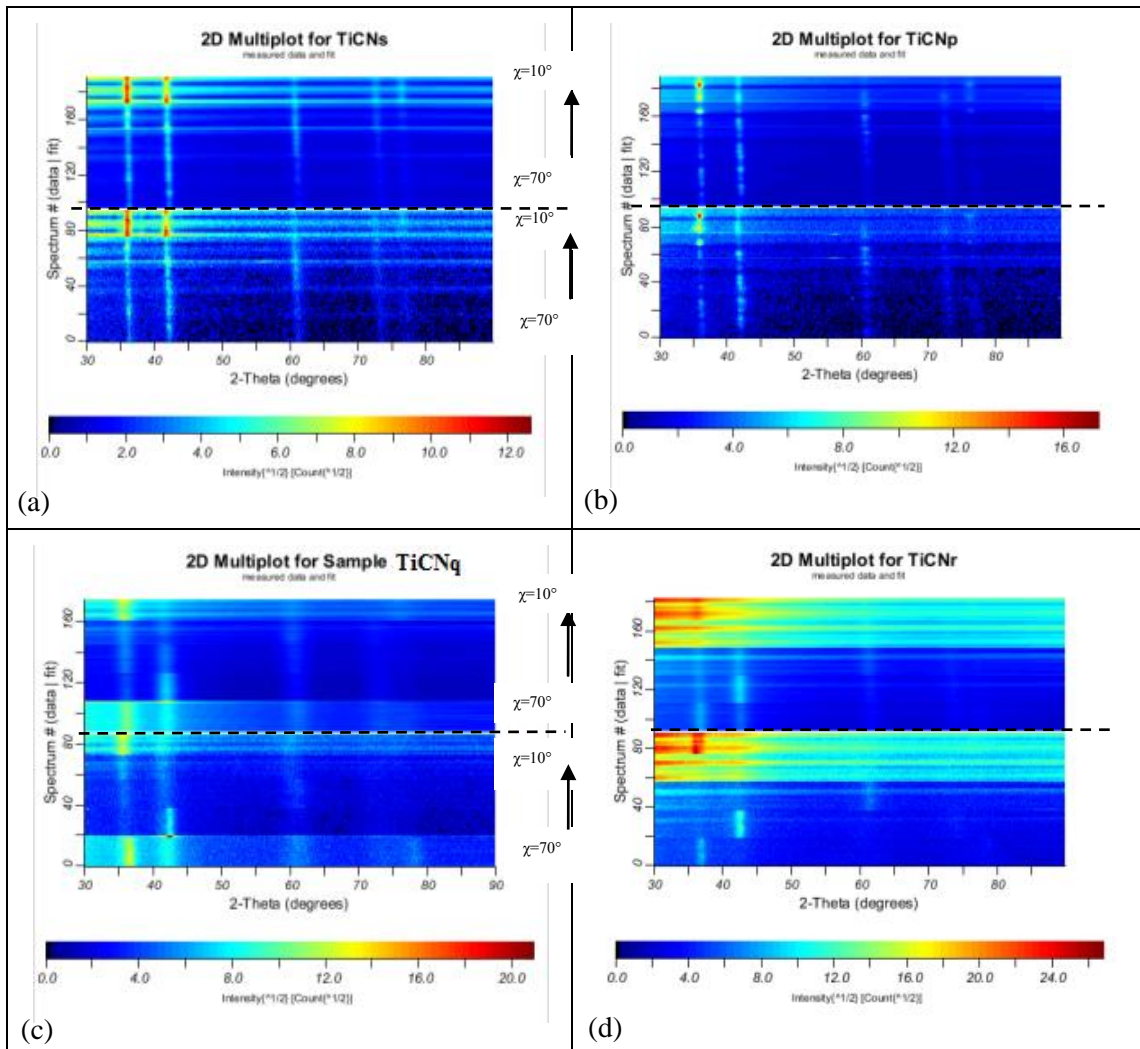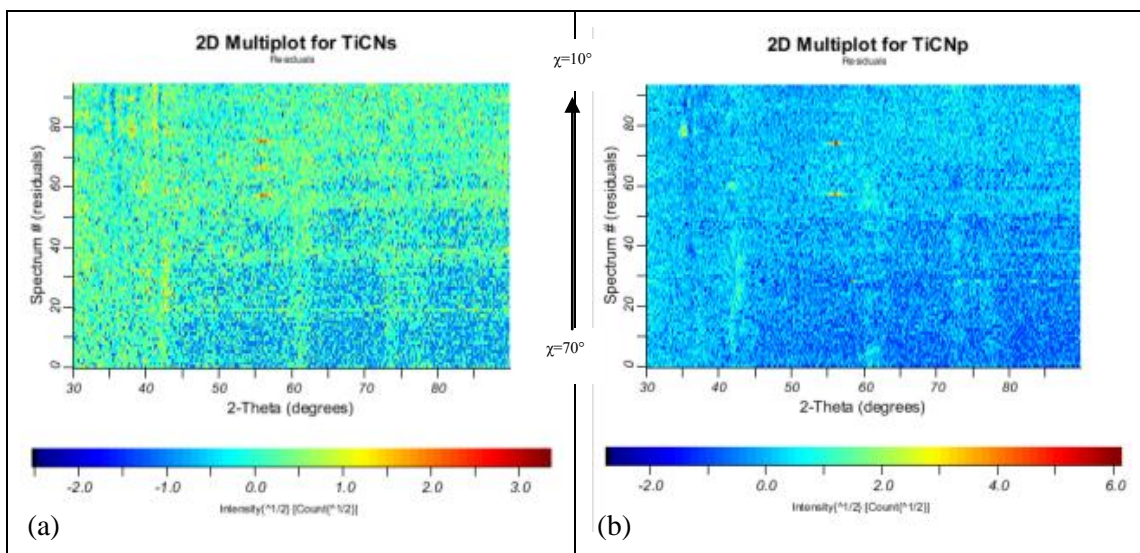

Figure 4.23 2D representation of diffraction intensities at various (χ,φ) positions in function of the 2θ displacement. The lower panel refers to experimental data, the upper are the best fit simulated ones.
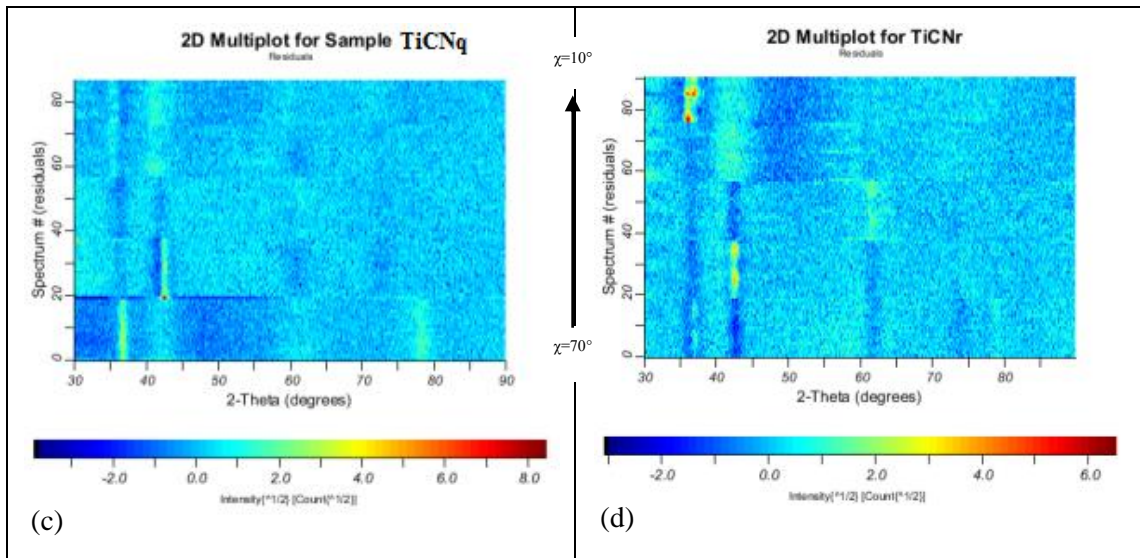
Figure 4.24   2D representation of difference plot between simulated and experimental spectra at various (χ,ϕ) positions in function of the 2θ displacement.

The 2D plots (Figure 4.23) show clearly a change in the relative peak intensity with changing the χ tilting angle. This phenomenon is especially visible between peaks [111] and [200] and is ascribed, as previously stated, to texture effects. Moreover, in the same plots it is clearly distinguishable for all the samples a systematic shift of the diffraction peaks with changing the co-latitude angle χ, whereas this effect is not evident when, fixing χ, sample is rotated at different angles ϕ (not shown). This effect is attributed to the presence of internal macrostress developed during the deposition process. The mathematical algorithm implemented in MAUD software is based on $\sin^2\psi$ relation, equation (2.6), which is presented in paragraph 2.4.2. The model adopted accounts for these effects by assuming the presence of a simple uniaxial stress state: even if simplified, this assumption seems to well reproduce the systematic peaks shift.

For samples TiCNs and TiCNp, the global fitting well reproduce the overall diffraction spectrum, the background contribution and the relative intensity change of diffraction peaks with the variation of co- latitude and azymuthal angle. On the contrary, calculated spectra for samples TiCNq and TiCNr present some important local discrepancies with the experimental measurements, as is visible from the difference plot (Figure 4.24c,d): in particular, a considerable difficulty is found in fitting position and shape of diffraction spectra with varying the χ tilting angle. This can be ascribed to the nanometrical size of crystalline grains, which notably broaden the diffraction spectra and can indeed possess a non-perfectly isotropic size distribution.

On the other hand, using the E-WIMV method, the variations of the peak intensities with the angles (χ,ϕ) are used to reconstruct the pole figures from the orientation distribution function of some crystallographic orientations. 2D plot of experimental and reconstructed Pole Figures, together with the Inverse Pole Figure of three orthonormal directions will be presented separately for each sample, as obtained from software's calculations and refinements (Figure 4.25, Figure 4.26, Figure 4.27 and Figure 4.28 for samples TiCNs, TiCNp, TiCNq and TiCNr respectively).

TiCNs Experimental Pole Figure

Reconstructed Pole Figure

Inverse Pole Figure

Figure 4.25   (a) Experimental Pole Figure and (b) Reconstructed Pole Figure of [111], [200], [220] diffraction peaks of sample TiCNs obtained from E-WIMV refinements.(c) Inverse Pole Figure relative to Normal Direction, Rolling Direction and Transversal Direction.

TiCNp Experimental Pole Figure

Reconstructed Pole Figure

92
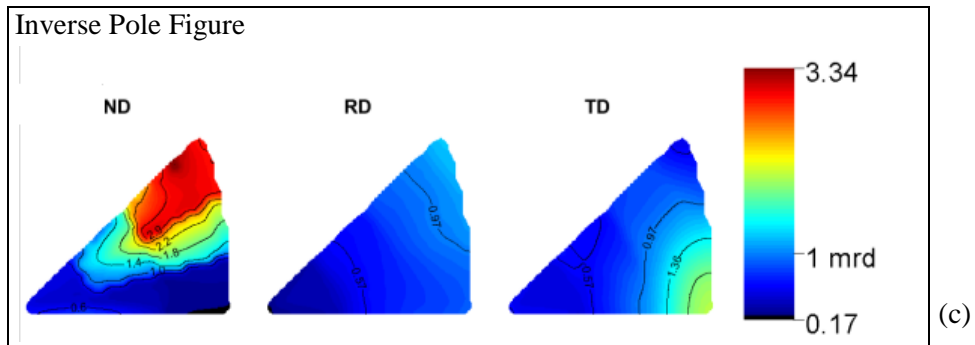
Figure 4.26 (a) Experimental Pole Figure and (b) Reconstructed Pole Figure of [111], [200], [220] diffraction peaks of sample TiCNp obtained from E-WIMV refinements.(c) Inverse Pole Figure relative to Normal Direction, Rolling Direction and Transversal Direction.

Figure 4.27 (a) Experimental Pole Figure and (b) Reconstructed Pole Figure of [111], [200], [220] diffraction peaks of sample TiCNq obtained from E-WIMV refinements.(c) Inverse Pole Figure relative to Normal Direction, Rolling Direction and Transversal Direction.
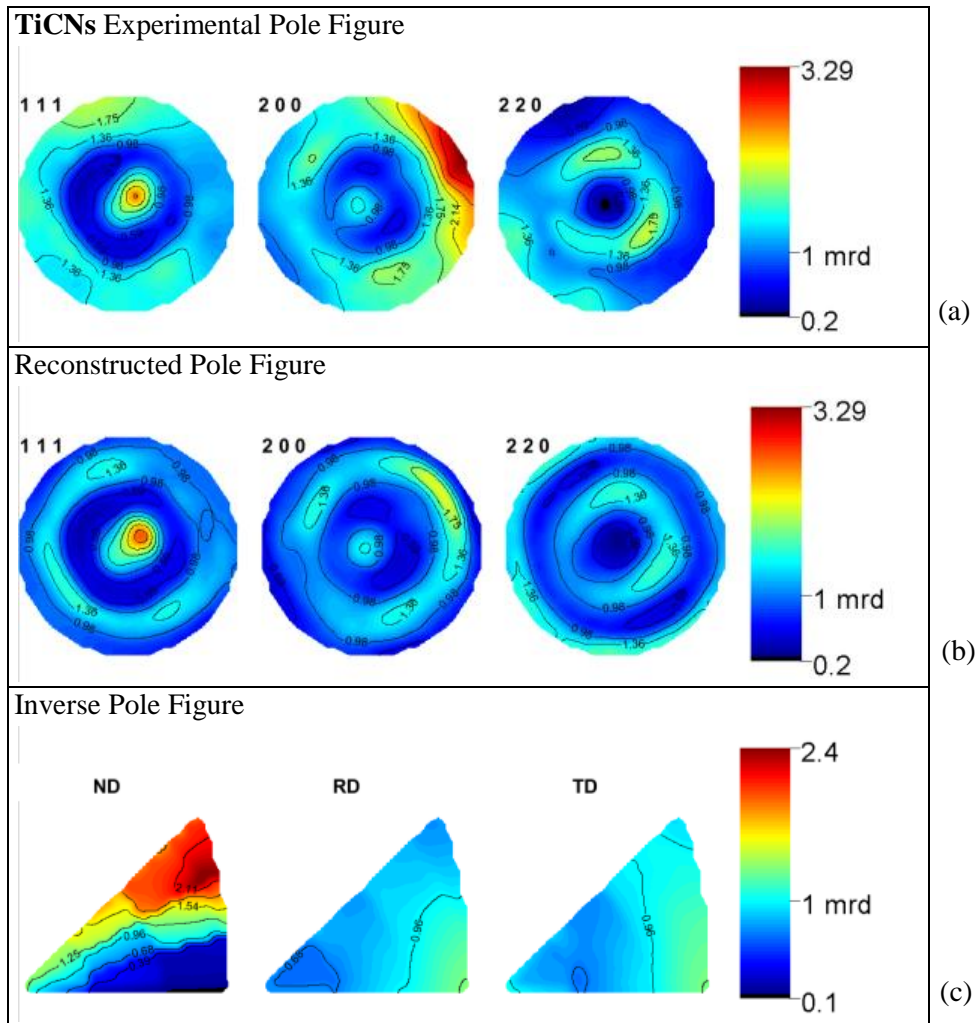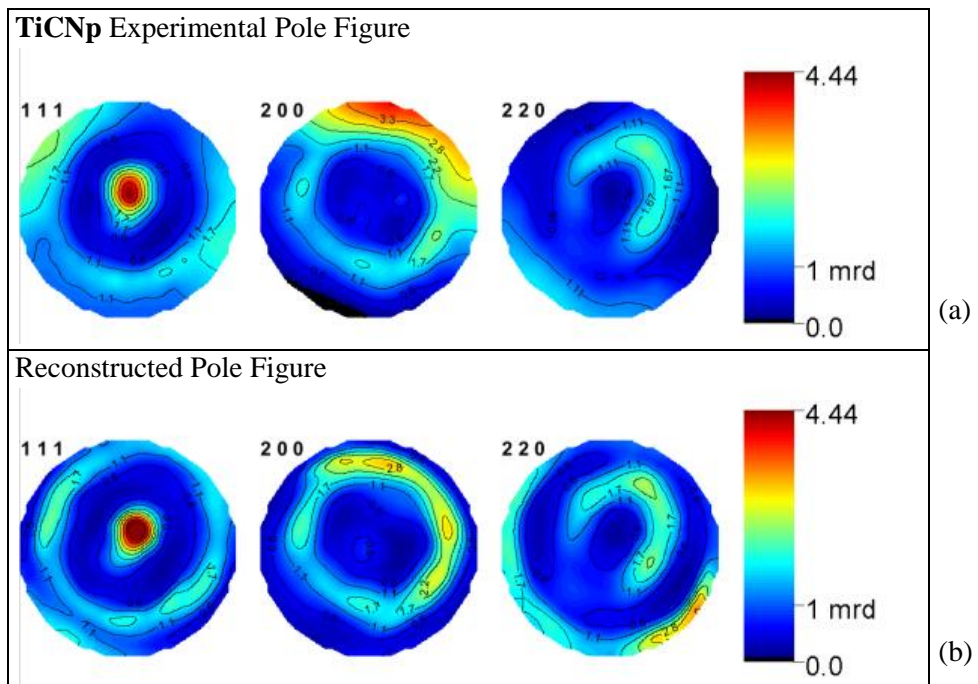
93

Figure 4.28 (a) Experimental Pole Figure and (b) Reconstructed Pole Figure of [111], [200], [220] diffraction peaks of sample TiCNr obtained from E-WIMV refinements.(c) Inverse Pole Figure relative to Normal Direction, Rolling Direction and Transversal Direction.
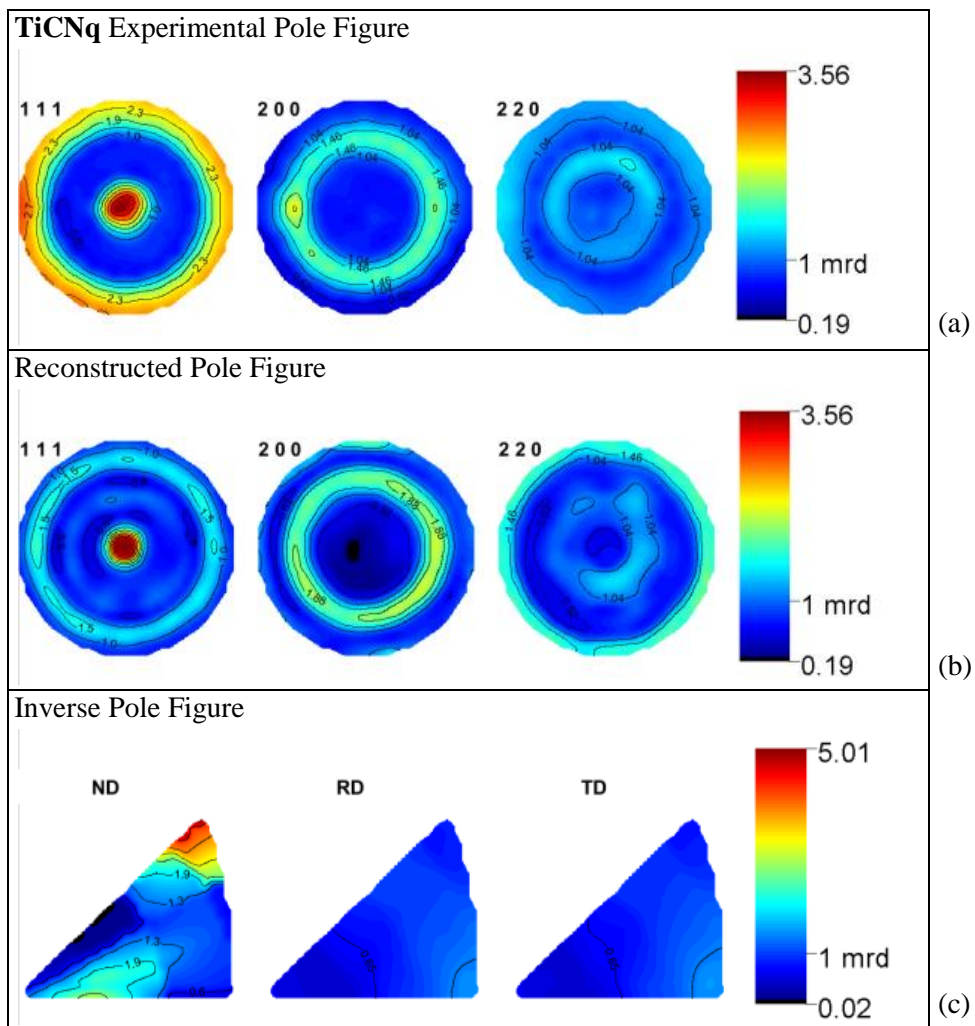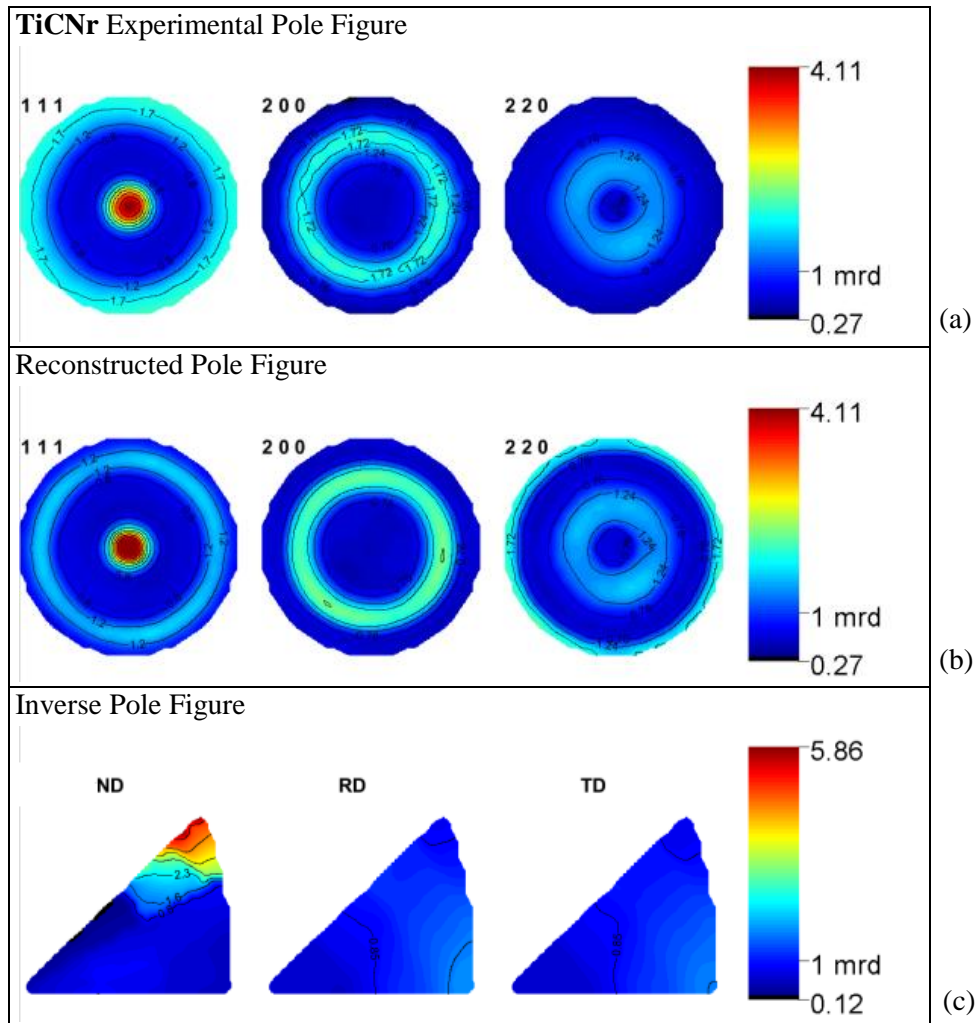
Experimental pole figures show for all the samples the tendency to generate a columnar textured structure with (111) planes parallel to the sample surface. This is in agreement with morphological analysis (Figure 4.1), previous texture evaluation (Figure 4.22) and also with published literature findings [31,35,36,47].

In general, the reconstructed pole figures are in good qualitative agreement with experimental ones, confirming that the solution obtained by the refinement process is reliable. It should however be pointed out that spectra obtained out of the central pole figure region are generally quite different from the experimental ones, probably due to some difficulty in the simulation. The following observations can be made:

(i)   Samples TiCNs and TiCNp clearly present a strong [111] preferential orientation, as expected from previous texture evaluation (Figure 4.22) and from morphological analysis (Figure 4.1). (111) plane lies parallel to the sample surface, as demonstrated by the presence of a pole maximum in the centre of the [111] Pole Figure. The ND inverse PF confirms this finding with the strong maximum that is visible on the corner of the plot which is relative to [111] direction (see diagram in Fig 2 appendix A).

(ii)   Sample TiCNq possess a softer texture, but the reconstructed PF predict a much stronger orientation. In spite of these discrepancies, the overall simulation is considered reliable, thanks to the fair accordance of intensity and difference plot.

94

(iii)   Sample TiCNr, indeed, present serious computational problems: the global diffraction spectrum presents a quite anomalous shape, and the measurement statistic could not be improved further due to the very low diffraction intensity of this sample; diffraction peaks position is found to vary also with changing the ϕ orientation, and this contributes to the strong local discrepancies visible in (Figure 4.24d). Moreover, experimental and reconstructed PF describe a perfect fiber structure, with [111] preferred orientation and randomly distributed [200] and [220] directions, typical of a columnar structure. Nevertheless, this prediction is denied by all the other observations (SEM, Raman, GIXRD), which show an amorphous structure for which very little texture effects are expected. Software simulation is probably in a false minimum and its results have been rejected. In order to obtain reliable structural parameter for this sample, GIXRD spectrum has been refined with an arbitrary texture algorithm, which let the relative peak intensity as a free parameter of the simulation. As a consequence, for this sample it was not possible to evaluate the internal film macrostress, because the implementation of this model in the calculation require multiple spectra at different (χ,ϕ) positions. The value of the lattice parameters obtained in this sample is therefore affected by a larger systematic error if compared with other samples.

4.3.5 Results

Are now reported in (Table 4-8) the structural parameters obtained from combined XRD – texture-stress refinements:

Sample	Lattice parameter [Å]	Crystal size [nm]	Micro-strain	Macro-stress$_{11}$ [GPa]	B factor	C occupancy
TiCNs	4,3006 ± 0,0001	25,5 ± 0,3	0,0031±0,0001	-2,38 ± 0,02	1,0±0,1	1,0
TiCNp	4,3105 ± 0,0001	34,9±0,8	0,0042±0,0001	-2,51 ± 0,02	1,7±0,1	1,0
TiCNq	4,3201 ± 0,0005	7,9±0,1	0,0121±0,0001	-2,53 ± 0,06	1,5±0,1	1,0
TiCNr	4,313 ± 0,001	3,4±0,1	0,021±0,001	//	1,3±0,1	1,0

Table 4-8: Results of combined Rietveld, E-WIMV texture and uniaxial macrostress computation.

Observing that C site occupancy for stoichiometric sample is always equal to unity, we can conclude that, for polycrystalline samples, all atoms are bounded in the TiCN structure and no understoichiometric phase is formed. In a similar way, we suppose that also for TiCNq and TiCNr samples all Ti atoms are bounded with some C or N, and all the excess atoms form the amorphous matrix:

$[C+N]_{tot} = [C+N]_{lattice} + [C+N]_{matrix}$,

$[Ti] = [C+N]_{lattice}$.

Thus, the quantity $([C+N]_{tot} - [Ti])$ [at%] has been considered as an estimation of the quantity of surplus atoms that constitute the a-(C,N) phase. Moreover, lattice parameter evolution has been represented as a function of the quantity $[C]/[C+N]$ (Figure 4.29), rather than the total C content, because we consider that interplanar spacing is influenced only by the amount of carbon that is effectively bound in the crystalline structure, a quantity that is evaluable only with the aid of some characterization techniques that were not available for the present research work, like XPS measurements. We thus considered the quantity $[C]/[C+N]$ as an estimation of the probability of carbon atoms to form bond with Ti and to constitute a crystalline structure. Moreover, for perfect crystalline samples, this quantity represents the stoichiometry of the

compound TiC_xN_{1-x}. In (Table 4-9) are reported the quantities to which crystalline structure parameters will be related. Errors were calculated from propagation on compositional values (Table 4-1): the great indeterminacy of EDS technique is now a strong limitation on structural considerations. Besides, we can infer that stoichiometric samples don't possess any excess atoms in form of interstitials or a-(C,N) phase because the quantity ($[C+N]_{tot} -[Ti]$) is compatible with zero.

Sample	$[C+N]_{tot} -[Ti]$ [at%]	$[C]/[C+N]$
TiCNs	3 $\pm$ 10	0,44 $\pm$ 0,07
TiCNp	-2 $\pm$ 10	0,64 $\pm$ 0,07
TiCNq	18 $\pm$ 11	0,72 $\pm$ 0,06
TiCNr	49 $\pm$ 10	0,82 $\pm$ 0,04

Table 4-9:   *Quantification of excess atoms and bonding probability of C atoms for TiCN coatings.*

Lattice parameter of TiCN structure has been compared with bulk values: in accordance with literature findings [42,44], thin coatings possess in general higher values of crystal lattice with respect to bulk ones; moreover, their progressive increase with carbon incorporation is in good accordance with the observed trend (black dotted line in (Figure 4.29) is a guide to the eye). Sample with the higher amount of C incorporation (namely TiCNr) is compatible with the observed fluctuation of bulk parameters from the general evolution.
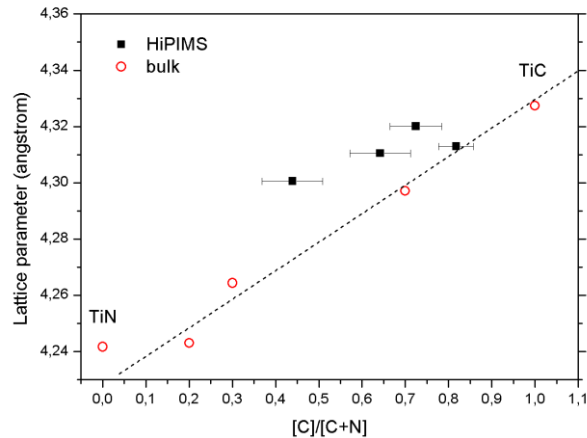
Figure 4.29 Evolution of lattice parameter of HiPIMS deposited TiCN with increasing probability of C incorporation. Red dots refer to bulk standard values and the dotted line is a guide to the eye.

The correlation between lattice parameter and crystal size proposed by Lewin et al [42] for TiC phase has been investigated for TiCN samples (Figure 4.30). Although at first sight no visible trend is appreciable, it must be noticed that the relative spread between the calculated values and a possible evolution trend (black dotted line is a guide to the eye), are compatible with the experimental variation observed also by Lewin et al. for the TiC phase (Figure 2.10). Nevertheless, the relative low number of experimental data prevents any possible conclusion in favor of the predicted charge transfer effect with small grain size.

Figure 4.30   Correlation between lattice parameter and grain size. Black dotted line is a guide to the eye.

Grain size appeared to be dependent upon the amount of excess atoms present in the structure (Figure 4.31a), as expected from the evolution model relative to simple TiC phase [41] presented in (Figure 2.8): the accumulation of s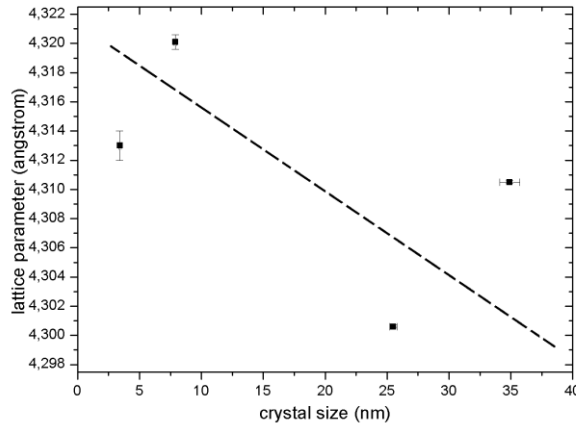urplus atoms at grain boundaries is favored also by the increase in deposition rate encountered at high acetylene flux (Figure 4.31b). In this high reactive gas regime a higher fraction of carbon atoms are effectively available for the deposition, as demonstrated by OES observations (Figure 3.17b); nevertheless, the high rate with which C atoms impinge on the growing film notably lower their mobility on the surface, determining the fast agglomeration in a disordered glass-like structure that hinder crystalline grain growth. The progressive decrease in crystal size visible in (Figure 4.31a) further demonstrate the transition from a prefect polycrystalline phase of stoichiometric samples, to a nanocrystalline compound embedded in an amorphous matrix, for samples with high C incorporation.
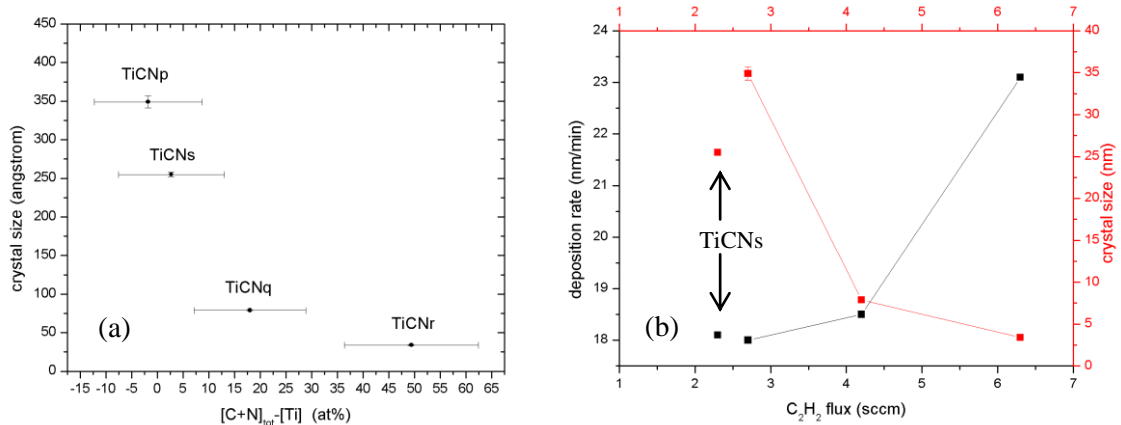
Figure 4.31   (a) Evolution of grain size with the amount of excess atom in the structure and (b) deposition rate and crystal size evolution with acetylene flux in the deposition process.

In accordance with literature findings [58], microstrain is found to be dependent upon both crystal size and the presence of the amorphous phase: as is visible from (Figure 4.32), samples with no amount of a-(C,N) show really low values of microstrain, due to their bigger grains (i.e. less deformable) with a columnar structure; on the contrary, the compact amorphous matrix act as a source of external deformation, which increase crystalline microstrain.
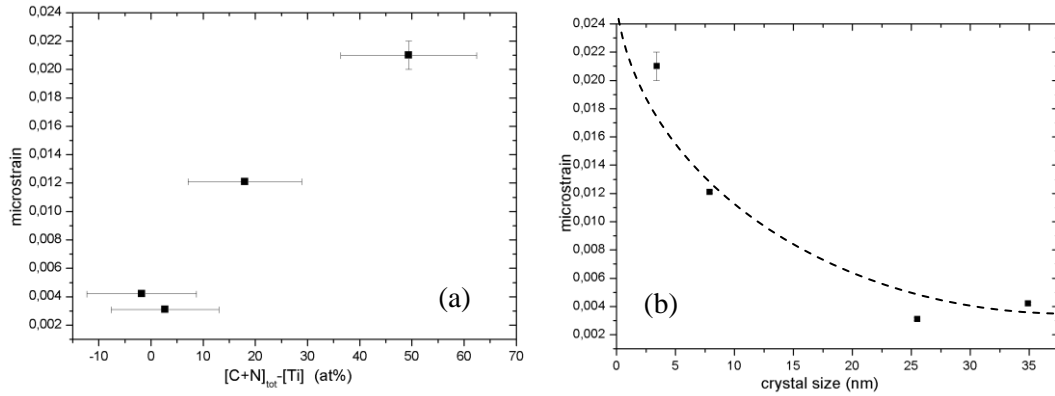
Figure 4.32 Evolution of microstrain in function of (a) the excess of (C+N) atoms that constitute the a-(C,N) phase, and (b) crystal size.

The presence of residual compressive macrostress ($\sigma_{11}<0$) generated in the film during its growth is recorded for all the samples, and is visible, as previously stated, in the progressive shift of the diffraction peaks with increasing the χ tilting angle (Figure 4.23) (i.e. reflecting (*hkl*) planes perpendicular to sample surface possess a smaller lattice parameter with respect to those (*hkl*) planes parallel to it). Samples TiCNs, TiCNp, and TiCNq possess a similar value of internal macrostress, despite this last sample exhibits also an amorphous phase that is expected to favor strain relaxation. The soft phase can indeed modify itself in order to absorb the effect of dislocation motion in the crystalline grains. Nevertheless, if the interspacing between grains is too small to allow intergranular interaction, its compliant action is strongly reduced.

The presence of compressive macrostress has a crucial role in coatings mechanical properties, because it is found to prevent the formation of cracks [66].

Mechanical and tribological characteristics of TiCN coatings will be presented in the next chapter and they will be related to the already found structural properties.

5. *MECHANICAL AND TRIBOLOGICAL CHARACTERIZATION*

When studying a new material for industrial purpose, several aspects must be taken into account. In general, good mechanical properties of a coating are, as briefly described in paragraph 2.5, high hardness, high toughness, low friction coefficient, high adhesion strength on substrate, good load support capability, etc.

When dealing with mechanical properties, it must be considered that all the quantities obtained from measurement are not exclusively referred to the coating, but they deal with the entire film/substrate systems as one unit. In fact, mechanical properties of the substrate play a decisive role for example in formation of cracks or in film adhesion.

Both nanoindentation and microscratch test were performed at Veneto Nanotech Labs using a Micromaterials Ltd equipement (platform 1), at room temperature of 25,5°C and 45% humidity.

5.1 Nanoindentation

A present, nanoindentation is regarded as a good method in hardness determination of thin films and coatings. To remind that different indentation tests produce hardness quantities expressed in different scales, we will refer to nanohardness to express the results obtained for the present measurements.

An understanding of nanoindentation begins with a study of contact mechanism between solid bodies. The indenter used to measure mechanical properties of TiCN, TiC and TiN coatings deposited on Si [001] substrate is a Berkovich diamond tip, that is a pyramidal, triangular based indenter with a blunt aperture angle of $\alpha = 70{,}296°$ [77].

Some mathematical models have been developed to describe a completely elastic contact between the flat specimen and the incident tip, from which it is possible to relate geometrical parameters with the applied load and the reduced Elastic modulus, E^*. Hertzian contact refers to spherical indenter, and is the simplest case first resolved. Pyramidal indenters can be considered, in a good approximation, as conical indenters, for which the applied load, P, and the overall penetration depth, h, are related by Sneddon's equation:

$$P = \frac{2}{\pi} E^* \tan \alpha \, h^2. \qquad (5.1)$$

The calculation methodology adopted by the software to relate the loading-unloading curves in function of the total displacement is Oliver-Pharr method, which will be briefly described below before presenting analysis' results.

5.1.1 Oliver-Pharr method for nanoindentation

In the Oliver-Pharr method, the projected contact area, A, between indenter tip and material is estimated using Sneddon' s equation (5.1). The methodology is based on the analysis of load-displacement curve, and is able to combine the elasto-plastic response of the material with the perfectly elastic mathematical models of axisimmetric indenters (spherical, conical, cylindrical..). The indentation modulus and hardness of the material can thus be calculated without the necessity to analyze the image of the indentation after the experiment: this particular

feature is typical of indentation on nanometrical scale, and enables to express hardness values also of elastic materials, for which no plastic deformation occurs.
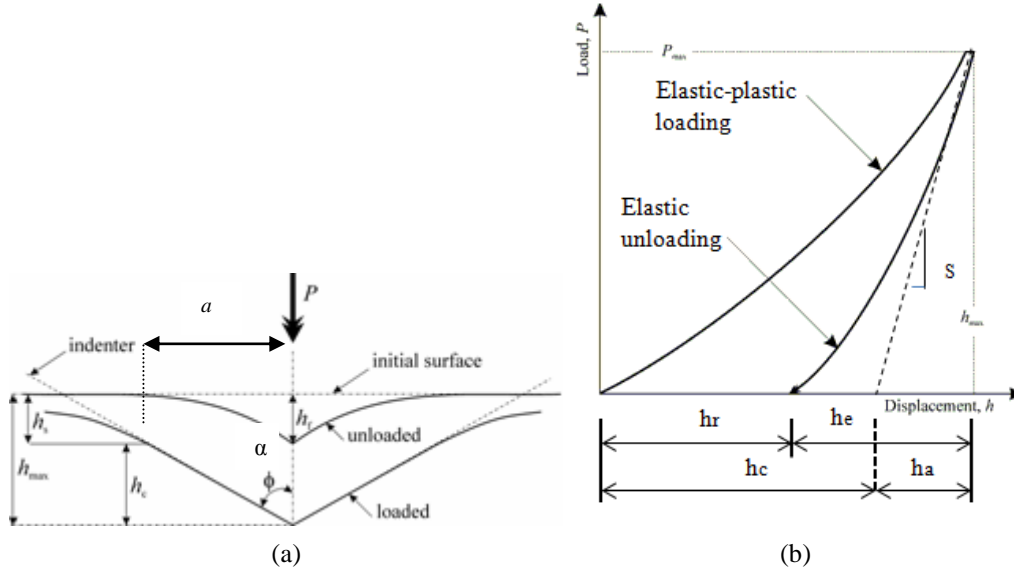

Figure 5.1   Representation of (a) the loading-unloading effect of the indenter tip on the material, and (b) a representation of the load-displacement curve, with all specified quantities for Oliver-Pharr calculation.

A very important quantity involved in this calculation method is the contact stiffness, defined as the derivate of the indentation load with respect to the elastic displacement on unloading (i.e. the slope of the unloading curve in the load-displacement plot (Figure 5.1b)):

$$S = \frac{dP}{dh}. \tag{5.2}$$

To determine projected contact area, A, the contact depth, h_c, i.e. the depth over which the indenter makes contact with the material, is needed. The mathematical expression of A for a Berkovich tip is known from geometrical considerations and is expressed as:

$$A = 3\sqrt{3}h_c^2 \tan^2 \theta = 24{,}5\,h_c^2, \tag{5.3}$$

where θ is a construction constant equal to $\theta=65{,}27°$ for a Berkovich tip.

The contact depth can be estimated as the difference between the maximum indentation displacement (h_{max}) and the elastic deflection of the surface (h_a) (Figure 5.1b), namely:

$$h_c = h_{max} - h_a = h_{max} - \frac{\varepsilon P}{S}, \tag{5.4}$$

after calculation from the elastic contact problem. ε is a constant that depends only upon indenter shape, and is equal to $\varepsilon = 0{,}72$ for a conical tip. The reduced Elastic Modulus, E^*, and the nanohardness, H, are calculated trough:

$$E^* = \frac{S}{2}\sqrt{\frac{\pi}{A}}, \tag{5.5}$$

$$H = \frac{P}{A}. \tag{5.6}$$

For measurements of nanohardness, the objective is to obtain a fully developed plastic zone within the film. To minimize the effect of the substrate on the measurement, the indentation depth is often limited to less than 10% of the film thickness (10% rule) and low loads are applied to prevent also the extension of the elastic zone in the substrate. In fact, for the

100

evaluation on elastic modulus, the substrate influence can't be completely separated from the measurement. In this case, a series of indentation with increasing load are performed, and from the trend of the elastic modulus is identified the maximum indentation depth where the substrate doesn't influence the measurement (i.e. around 150nm).

5.1.2 Indentation results

The mean nanohardness and reduced Elastic modulus have been determined for TiCN, TiC and TiN samples on Si[001] substrate, from a repetition of twelve measurements with indentation load of 7mN that satisfy the 10% rule. Oliver-Pharr method was implemented in the analyzing software, together with all necessaries corrections of instrumental aberrations (thermal drift, instrument compliance, indenter shape corrections,..).

Results obtained from the measurements are listed in (Table 5-1): are also reported the ratios H/E^* and H^3/E^{*2} that will be related to coating's mechanical properties, as explained in paragraph 2.5. Errors on these last quantities have been estimated by propagation.

Sample	E^* [GPa]	H [GPa]	W_e [%]	H/E^*	H^3/E^{*2} [GPa]
TiCNs	248 ± 15	27,3 ± 2,2	55	0,11 ± 0,01	0,33 ± 0,09
TiCNp	253 ± 16	29,0 ± 1,9	59	0,11 ± 0,01	0,38 ± 0,09
TiCNq	192 ± 15	23,0 ± 1,7	57	0,12 ± 0,01	0,33 ± 0,09
TiCNr	131 ± 6	14,5 ± 0,9	47	0,11 ± 0,01	0,18 ± 0,04
TiN	206 ± 12	22,0 ± 1,4	51	0,11 ± 0,01	0,25 ± 0,06
TiC4	108 ± 6	11,9 ± 0,8	45	0,11 ± 0,01	0,14 ± 0,03
TiC6	120 ± 5	11,8 ± 0,5	46	0,10 ± 0,01	0,11 ± 0,02
TiC10	109 ± 3	11,6 ± 0,4	47	0,11 ± 0,01	0,13 ± 0,02

Table 5-1:   Experimental quantities obtained from nanoindentation measurements.
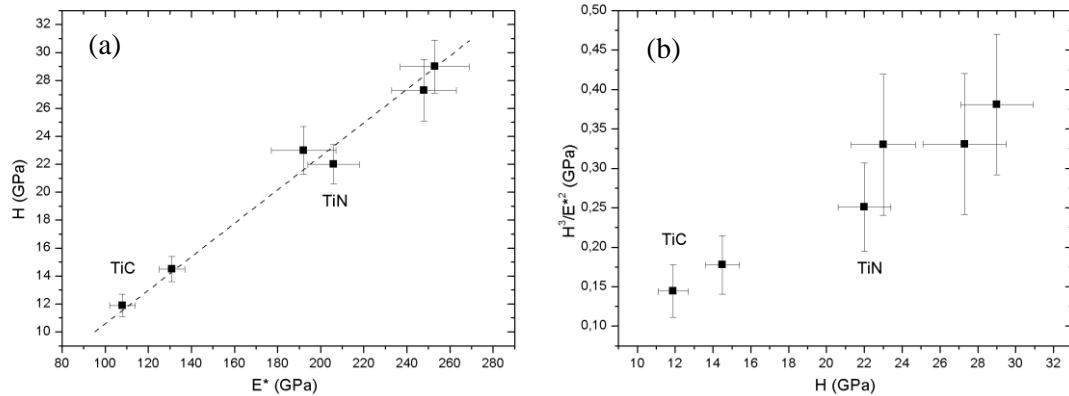
Figure 5.2   Representation of the evolution of (a) nanohardness as a function of reduced young's Modulus (dotted line is a guide to the eye), and (b) the ratio H^3/E^{*2} as a function of H.

The evolution of nanohardness with elastic modulus is in good approximation a linear relationship, with slope $H/E^* \approx 0,11$ (Figure 5.2a). This finding confirm the experimental trend observed for a various range of other different nitrides materials deposited by magnetron sputtering (Figure 2.25a), and indicates that all coatings possess a good resistance to mechanical degradation and failure, being satisfied the relation $H/E^* > 0,1$ [65,66]. Besides, if observing the experimental data, we note that, except for sample TiCNr (H≈14,5 GPa), titanium carbon nitrides show superior properties with respect to TiC (H≈12 GPa) and TiN (H≈22 GPa) coatings, as reported also in literature, confirming their good applicability as hard protective layers in industrial tooling.

TiC coatings present all compatible values of both hardness and elastic modulus. The mediocre performance is attributed primarily to the large amount of amorphous phase in the samples, which sensibly lower hardness values, accordingly to the high visco-plastic deformation occurring in a glass-like structure (Figure 2.23).

The dependence of H^3/E^{*2} vs. H (Figure 5.2b) should be a quadratic evolution from literature findings (Figure 2.25b). The high value of H^3/E^{*2} for TiCN coatings is an indication of their good resistance to plastic deformation and formation of cracking (i.e. $H^3/E^{*2} \approx 0,33 \div 0,38$ GPa).

Experiments in literature indicate that the toughness of the system thin film/substrate is higher the higher is the ratio H^3/E^{*2}. Therefore, this quantity should be maximized in order to increase the resistance to plastic deformation, and thus to improve the film elastic recovery W_e [65,66]. TiCN films possess increase tough character with respect to TiC or TiN coatings, as is visible from the general higher values of elastic recovery parameter (i.e. $W_e \approx 51 \div 59\%$) (Figure 5.3).
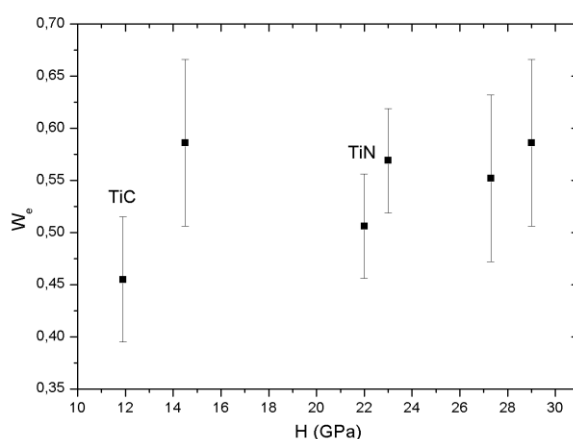

Figure 5.3   Elastic recovery parameters as a function of increasing hardness.

If regarding the property maps for abrasion resistance materials (Figure 2.26), TiCN coatings collocate in the upper right part of the plot, in the region of superior hardness performances with other ceramic materials such as Si_3N_4, AlN and SiC, with the best features obtained by sample TiCNp.

Focusing only on performances of TiCN coatings, we can observe in (Figure 5.4a,b) how nanohardness and reduced Elastic modulus are strongly dependent on the quantity of a-(C,N) phase in the structure. In particular, sample TiCNp possesses the best performances, namely $H \approx 29$ GPa and $E^* \approx 253$ GPa, and this is ascribed to its polycrystalline structure (grain size ≈ 35 nm) and stoichiometry near $TiC_{0.6}N_{0.4}$ as calculated from EDS compositional values. Also sample TiCNs, which possess a greater amount of nitrogen and a prefect nanocrystalline phase, presents a good mechanical properties ($H \approx 27$ GPa and $E^* \approx 248$ GPa): this fact confirms the strong effect of grain boundaries in hindering dislocation movement [63], and the negligible influence on hardness and elastic modulus of nitrogen content, as observed by Restello and co workers (Figure 2.24) [31]. When decreasing the OE set point from the stoichiometric 60% condition (i.e. for samples TiCNq and TiCNr), mechanical features linearly decrease, until reaching the lowest values of $H \approx 14$ GPa and $E^* \approx 131$ GPa in sample deposited at 27% OE set point. As demonstrated by Raman spectroscopy and XRD analysis, this sample possess the higher amount of amorphous phase, and a grain size inferior to 10 nm, which is found to worsen toughness properties because of grain boundary sliding [63].

It must be pointed out that nanohardness values obtained by reactive HiPIMS are lower than other experimental results on TiCN coating deposited by reactive DCMS ($H \approx 30\text{-}45$ GPa)

[31,48], but this is ascribed to the hardening power of substrate RF biasing during deposition, that ensure a higher ion bombardment and the constitution of a denser structure [78].
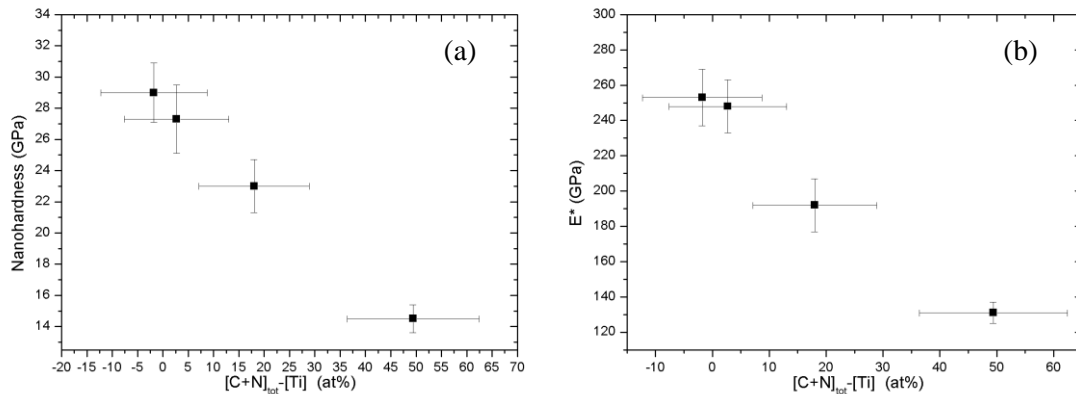

Figure 5.4 Evolution of (a) nanohardness and (b) reduced Elastic modulus for TiCN coatings as a function of the total amount of a-(C,N) phase in the structure.

5.2 **Scratch test**

In order to determine and analyze the adhesion strength of a coating to a substrate, scratch test is widely used by research laboratories as well as the industry.

Although several numbers of intrinsic and extrinsic parameters affect the scratch measure, like surface/coating mechanical properties, film thickness, loading rate, indenter tip radius, etc., some interesting consideration can be drawn by observing the failure mechanism of the film during the test, and results on the critical loads for plastic deformation or fracture can be compared if measurements parameters are kept constant.

The failure modes of hard coatings can be broadly split into four categories:

1. Trough-thickness cracking, including tensile cracking behind the indenter (Figure 5.5d), conformal cracking as the coating is bent into the scratch track (Figure 5.5c) and Hertzian cracking (not shown). These cracks may extend into the substrate if it is sufficiently brittle, but are usually stopped at the interface in a hard coating on a softer substrate.
2. Coating detachment, including compressive spallation ahead of the indenter –wedge spallation- (Figure 5.5a), buckling spallation ahead of the indenter (Figure 5.5b) or elastic recovery-induced spallation behind the indenter (not shown).
3. Chipping within the coating.
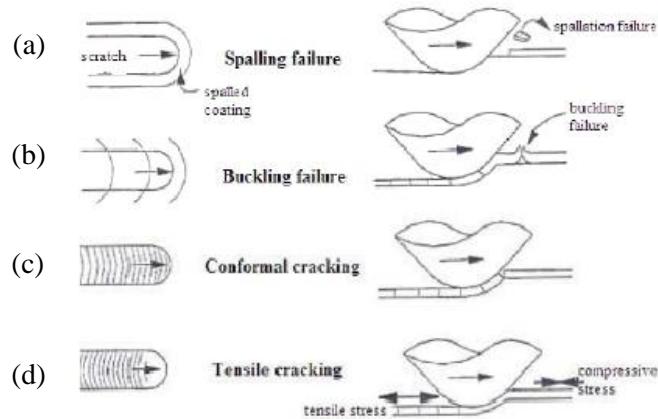4. Chipping within the substrate.

Figure 5.5   Examples of the main fracture morphologies at the interface between the film and the substrate during a microscratch test.

Failure mechanism related to adhesion for hard coatings are the most interesting to study, because they give the major information on coating's characteristics.

Buckling is the failure mode most common for thin coatings that are able to bend in response to applied stress. Failure occurs in response to the compressive stress generated ahead of the moving indenter (Figure 5.6 a-d). Localized regions containing defects start the formation and propagation of buckles, that progressively spread laterally forming interfacial cracks: in these regions, spallation easily occurs in response to the high tensile stress formed within the coating after the tip scratch. In most cases, buckles form in the region of plastic pile-up (ploughing) ahead of the moving indenter. The amount of pile-up depends on the hardness of the substrate and the critical load in the scratch test in inversely proportional to film thickness [69].

Wedge spallation occurs when the coating is stiffer, and compressive shear cracks form throughout the film thickness, some distance ahead of the indenter. Those cracks have sloping sides, and can propagate pushed by the moving tip, causing interfacial cracks and film detachment in large plaques (Figure 5.6e-h).

Recovery spallation is indeed associated with the elastic recovery which occurs behind the stylus: due to plastic deformation in the substrate, the coating can't completely recover elastically, and a tensile recovery stress can be easily converted into shear stress and successive cracking on either side of the scratch track.
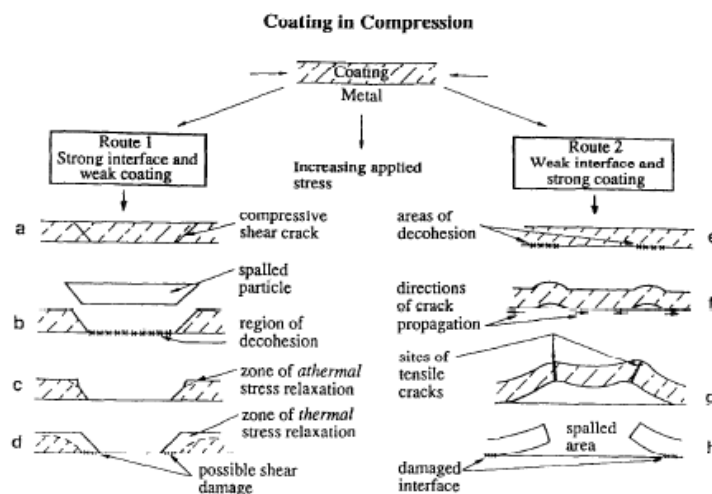

Figure 5.6   Schematic of the main stages in adhesion-related coating failure mechanism, (a)-(d) buckling and (e)-(h) wedge spallation. [68].

104

Scratch tests have been performed on TiCN and TiN samples deposited on steel substrate, using a Rockwell C diamond tip of 25μm radius. The indentation load was progressively raised up to 10N. Stylus has been polished with isopropyl alcohol between each sample scratch test, in order to avoid the interference of a possible lubricant layer formed during contact and deposited on the tip.

During scratch test, also the frictional force has been measured, from which it was possible to calculate the coefficient of friction of the coating (CoF) from equation (2.21).

Micrographs of the scratch traces are now presented for samples TiN and TiCN, with increasing order of carbon incorporation (Figure 5.7a-l).

The coating failure mechanism varies considerably within the samples: the greater performances are attributable to TiN coating (Figure 5.7a,b), for which no significant damage is observed until the near end of the scratch track, where little detachment from the substrate is visible. Other failure effects are pile up of the material at both sides and on the top of the track, together with trough-thickness conformal cracking. These features indicates a great adhesion strength of the coating on the steel substrate, but it must be underlined that TiN samples possesses about half the thickness of TiCN coatings, and this fact intrinsically ameliorate its performances [69].

Sample TiCNs is the best performing sample among titanium carbon nitrides (Figure 5.7c,d), and it is ascribed to the major nitrogen incorporation in the structure, that get close to the nitride coating features. As reported also by other researcher [31], N incorporation improves film resistance to delamination failure, and helps increase also the critical load to fracture.

The failure mode observed is wedge spallation at the top of the scratch indentation, indicating the progressive accumulation of compressive shear with the moving tip that finally entails delamination effects. Moreover, the coating possesses good bending properties, because only buckling and conformal cracking are visible in the scratch trace, confirming the high toughness character of this sample.

TiCN samples deposited with decreasing OE set point, i.e. with increasing carbon content, at constant nitrogen incorporation, show a progressive worsen of adhesion: TiCNp (Figure 5.7e,f) failed principally by wedge spallation and detachment from the substrate in correspondence with the scratch track. Besides, the damaged areas are less pronounced than sample TiCNq (Figure 5.7g,h), indicating a better capability to absorb energy and compressive shear during load. The coating deposited at 40% OE presents poor adhesion properties, since extended areas of complete detachment from the substrate are clearly visible. Moreover, spallated regions are large and diffuse on both sides of the scratch trace, which present features typical of a brittle tensile cracking and chipping at the piled-up edges.

Differently, sample TiCNq (Figure 5.7i,l) is not affected by wedge spallation or delamination, but fails rather by chipping on the through-thickness cracking formed during the indentation movement. This behavior is ascribed to the compliant character of the amorphous matrix, which absorbs the energy of the compressive stress generating a high amount of plastic deformation.
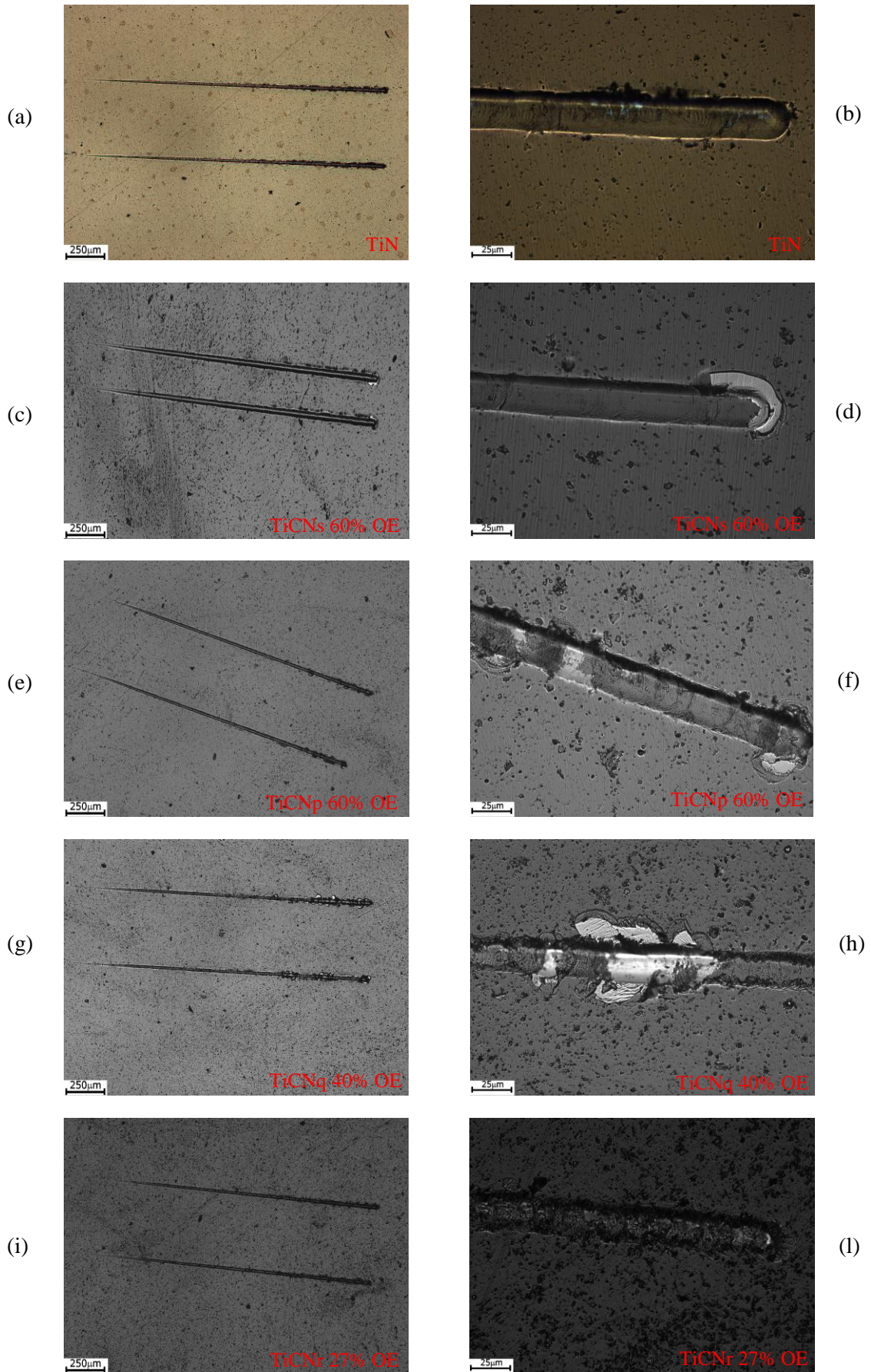
Figure 5.7   Micrograph of scratch test performed on TiN and TiCN samples. On the left images are taken at 50x magnification, on the right at 500x magnification.

We will now present results from the analysis of critical load and friction coefficient. We identified four types of critical loads associated to various failure mechanisms:

i. Yielding load L_y, defined as the load necessary to produce plastic deformation in the coating. It has been evaluated at the point where discrepancy between the topography before and after the scratch test is of the order of average surface roughness.

ii. Critical load for local defect formation during the scratch track, like the appearance of detachment from the substrate and wedge spallation, L_{c1}. It usually occurs in the middle of the scratch track, when the compressive energy stored relaxes, producing the first formation of fractures.

iii. Critical load for complete failure of the coating for wedge spallation, which is located near the end of the scratch track L_{c2}.

iv. Critical load for chipping and buckling, L_{c3}. It is visible only in sample TiCNr, for which a different failure mechanism from all the other samples occurs.

In the following graphics (Figure 5.8a-e) are superposed the topographies before and after scratch tests (black dotted and continuous line respectively; progressive depth is represented in modulus), together with the evolution of the frictional force with the increasing applied load (red line). The evolution of critical loads for failure and of the coefficient of friction has been related to the relative amount of nitrogen over total carbon and nitrogen content [N]/[C+N] (Figure 5.9a,b). It must be underlined as the estimation of the various critical loads is not based on any mathematical calculation, but it is derived only by a visual interpretation of the scratch track. Therefore, errors are not evaluable on those quantities, and only semi-quantitative conclusion can be drawn, even though of a significant importance. The critical load for plastic deformation initiation, L_y, was expected to be maximal for sample TiCNp, as it owns the highest value of H^3/E^{*2}, and minimal for sample TiCNq (Figure 5.2b). Nevertheless, values of L_y are not really different from sample to sample, and they all oscillate around values of $L_y \approx 1$ N, indicating a similar response to plastic deformation. This is ascribed to the effect of substrate material, which is probably soft and thus deforms sensibly during the scratch test.

More significant is the evolution of the critical load for complete failure by wedge spallation, L_{c2}, at the end of the scratch track (blue triangles in (Figure 5.9a)), that can be related to coating toughness: this quantity evolves form $L_{c2} \approx 8,0$ N for sample TiCNq, to $L_{c2} \approx 8,6$ N for sample TiCNs, and eventually become >10 N for TiN sample, which presents no wedge spallation failure at the end of the track (Figure 5.7b). This is a precise sign of the effect of nitrogen incorporation in the coating's structure, indicating that the choice of an appropriate stiochiometry of TiC_xN_{1-x} films helps to increase adherence performances and resistance to failure.

The other critical loads for local detachment or buckling, L_{c1} and L_{c3}, indicate the presence of failure of coating adhesion on the steel substrate during the scratch: except for TiCNs sample, for which no fracture are visible until the end of the track, for all the other samples first signs of failure appear at half of the indentation measurement, i.e. at a distance of $d \approx 1$mm.
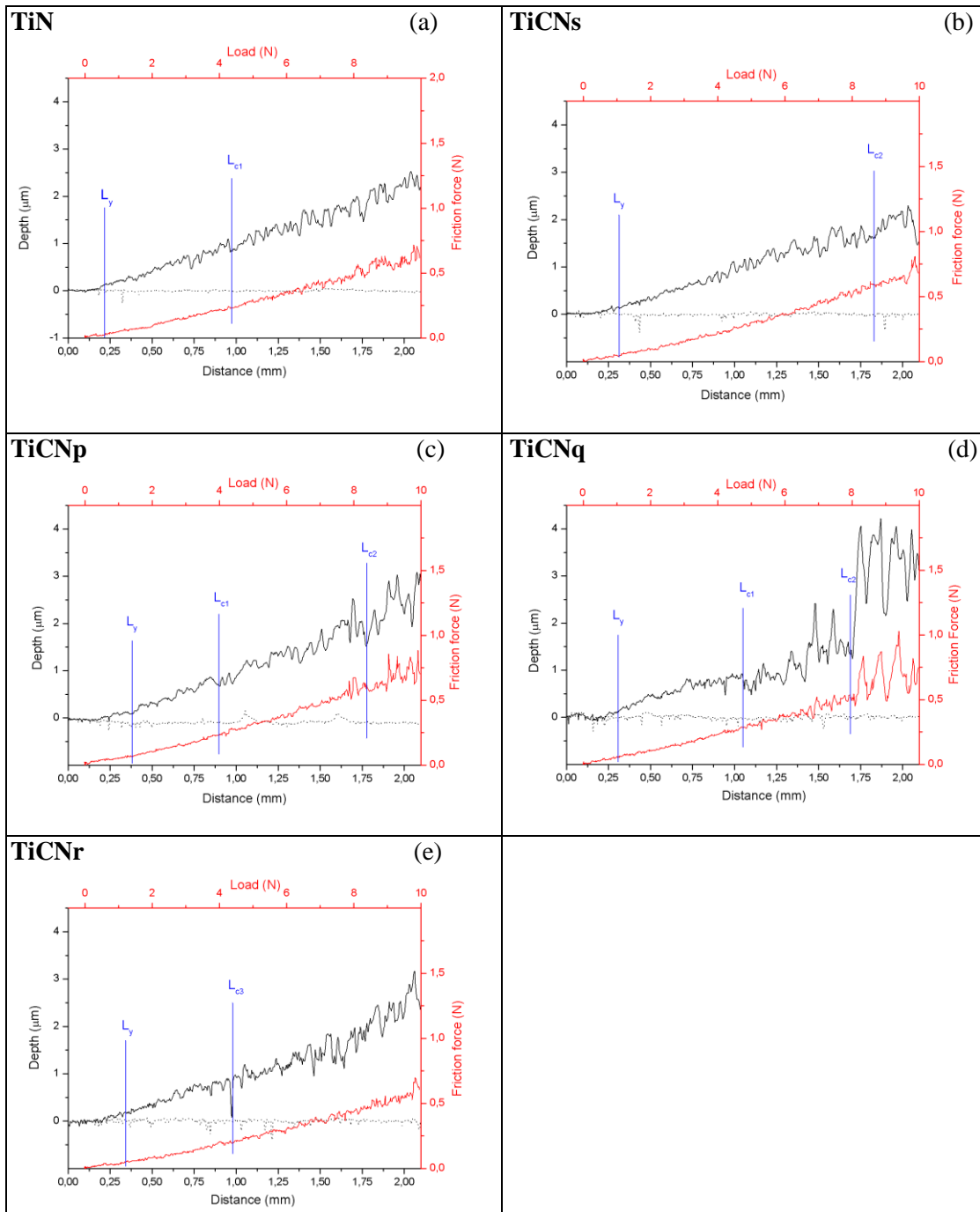
Figure 5.8   Graphical reproduction of surface topologies before and after the scratch test (black dotted and continuous line respectively) superimposed to the friction force developed under progressive load (red line). Critical loads for failure are indicated.
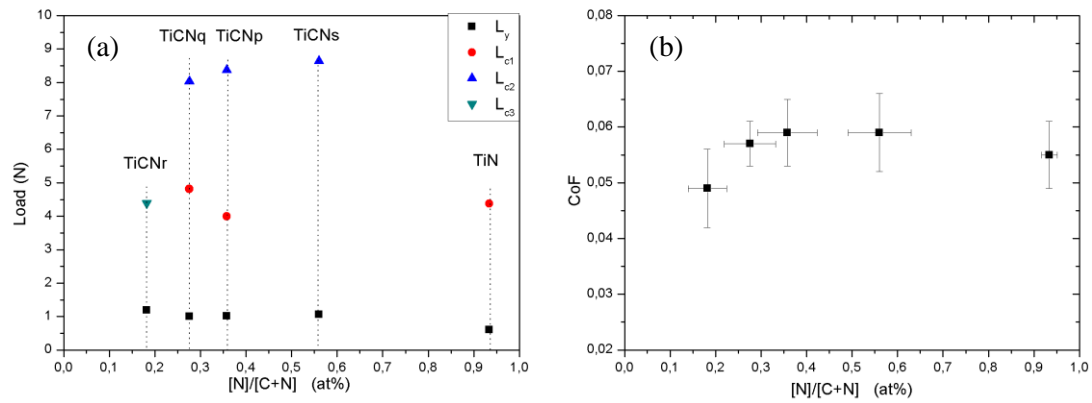
Figure 5.9   Evolution of (a) critical loads for failure and of (b) the coefficient of friction with the total [N]/[C+N] content.

Friction coefficient (CoF) of diamond on TiN and TiCN coating presents very low values, i.e. CoF ≈ 0,06 (Figure 5.9b). To the best of our knowledge, no literature data are available to compare CoF of TiCN against diamond, because mainly tribological test using steel or WC balls have been performed. Besides, several authors report the formation of an a-C transfer layer that reduce friction coefficient and acts as a solid lubricant [35,47-49]. This effect can explain the lower friction coefficient recorded for sample TiCNr, CoF ≈ 0,05, which possesses the highest amount of amorphous carbon-based phase (a-C and a-(C,N) at 27% OE). It was observed that friction is mainly controlled by the kind of C-based phase [49]: the CN_x amorphous phase formed inside the TiCN nanocomposites is found to be a less efficient lubricant in comparison with the amorphous C. Besides, the presence of hydrogen seems to additionally ameliorate tribological performances [70] thanks to its stabilizing action on sp^3- bonded carbon phase, that make the material chemically inert and lower the adhesive force during sliding against other materials.

Looking at the general mechanical and tribological properties of carbonnitrides samples, TiCNs seems to be the best performing coating, thanks to its relatively high nanohardness and elastic modulus (H=27,3±2,2 GPa, E^*=248±15 GPa), and superior adhesion properties after scratch test (L_{c2}≈8,6 N), with poor failure and good toughness.

6. CONCLUSIONS

Titanium carbon nitrides coatings have been deposited for the first time by HiPIMS in a reactive ambient of two gases, nitrogen and acetylene. Differently from TiCN coatings obtained by DCMS, no literature data were available on the influence of HiPIMS deposition parameters on the film structure and properties. The principal aim of this research work was thus to characterize the deposition procedure and to understand how to tailor process parameters in order to obtain a fine control of the coating's characteristics.

The first aspect that we investigated was the competitive action of a system of two reactive gases: trough Optical Emission Spectroscopy we monitored the optical signals of reactive species in front of two different solid targets. We found that the poisoning action during reactive plasma process depends strongly on the elemental target adopted: in our case, Ti target is more easily poisoned by nitrogen after nearly complete dissociation from gas phase; on the contrary, C target present minor reactivity and nitrogen remains in the chamber preferentially as N_2 molecule. This affects N^+ ion energy, as it was proposed that, if coming from the sputtered target, the ionized atom possesses effectively higher energy than if it came from gaseous phase.

When introducing a second reactive gas, the system gets complex: C_2H_2 molecule was found to almost completely dissociate during plasma formation in HiPIMS process, but C atoms can either compete in the poisoning process of the solid target, either deposit on the growing surface from gas phase, and finally react with dissociated N forming CN species, thus altering the transition process from metallic to target's poisoned regime.

To reach a control over this complex plasma system, we adopted a methodology of continuous time monitoring of emission lines of some specific elements, which we related with the compositional nature of the growing film. In particular, as yet demonstrated by Restello et al. [31], Ti (499,1 nm) line is a perfect indicator of the total Ti amount contained in the structure: by varying the OE set point from its purely metallic value, it is possible to obtain stoichiometric coatings (at 60% OE), or either understoichiometric compounds with less Ti content when decreasing the O.E. set point.

Moreover, we pointed out that it is possible to control the total C content by looking at the ratio H (656 nm)/Ti (499,1 nm), which shows a good linear relationship with both C and C/Ti concentration if nitrogen flow rate is maintained constant. This important finding opens promising perspectives for microstructural design trough deposition with HiPIMS, for which it is in general complicate to tailor coating properties in a system of two reactive gases.

TiCN samples have been deposited with a pulse repetition frequency of 500 Hz, pulse on time of 60μs and total power of 2kW. The plasma forming gas was pure Ar, and the OE set point was changed from 60%, to 40% and 27% respectively, keeping its value constant during the deposition in order to obtain a monolayer structure. No bias or intentional heating was applied to the substrate holder. Samples were deposited both on Si [001] and mirrored polished steel substrate and, in order to ameliorate wear properties, a thin Ti+TiN interlayer was included in the structure, after observing that TiC intermediate layer worsen coating adhesion.

We found, as predicted by literature observations, that the total C content strongly influence coating structural properties, determining the transition from a compact fine nanocolumnar structure for polycrystalline stoichiometric coatings (grain size between 25 and 35 nm), to a nanocomposite system of dimension <10 nm embedded in an amorphous a-(C,N) matrix, when raising the total C incorporation.

We related the [C]/[C+N] amount to the variation of lattice parameter, which is found to linearly increase following Vegard's rule, from 4,300(6) Å to 4,320(1) Å in a compositional range from $TiC_{0.4}N_{0.6}$ to $TiC_{0.7}N_{0.3}$. We tried to investigate also the theory of lattice expansion in nc-TiCN/a-C by charge transfer between crystalline and amorphous phase proposed by Lewin et al. [42], but the sampling was too poor to determine if a precise trend is effectively followed. It will be interesting to effectuate a broad-spectrum analysis to verify if this model applies to TiCN nanocomposites: this will give more insight in the comprehension of microstructural evolution during film growth in different conditions, and it may open some new ways of mechanical properties design trough controlling the bonding in the nc-phase.

It was observed by X-ray diffraction measurements that polycrystalline samples show a preferred [100] orientation with plane (111) aligned parallel to sample surface: this characteristic is in accordance with literature findings [37,47,48], and demonstrate that the crystalline structure is growing on the densely packed plane, ameliorating the compactness of the coating.

The quantity of amorphous phase constituted by both excess C and N atoms, which was detected by Raman spectroscopy, was found to hinder crystal size growth and to affect the internal microstrain state, contributing to its enhancement. Furthermore, an evidence of a compressive stress in the film was observed by X-ray diffraction: this feature was attributed to a compressive stress state developed in the coating during the high bombarding energy deposition. The presence of compressive stress is reported in literature to prevent crack formation [65,66], thus ameliorating toughness properties.

Tribo-mechanical tests reveal that TiCN coatings deposited by HiPIMS possess in general good nanohardness and elastic modulus, with best performing values of (H=29,0 ± 1,9 GPa and E^*=253 ± 16 GPa) for a perfect polycrystalline samples deposited at 60% O.E. with fluxes (C_2H_2=2,7 sccm and N_2=0,7 sccm). Those values are superior to simple TiC or TiN deposited by HiPIMS in similar conditions, confirming the best performances of TiCN as a ternary metal-nitride system.

Just as carbon amount strongly influence structural features, so there nitrogen acts on adhesion properties: an appropriate nitrogen content was found to increase both the critical load for fracture formation and for delamination failure. Scratch tests show that wedge spallation and coating detachment present less pronounced detrimental character when moving at stoichiometric conditions towards higher N incorporation, confirming that nitrogen is an important parameter affecting coating toughness.

Besides, the presence of an amorphous phase can change the response to frictional stress: it was found that a sufficient interspacing among nanocrystals can hinder interplanar interaction, making the structure compliant in response to an applied external load. Moreover, the formation of a transfer layer on the sliding tip can act as a solid lubricant, thus lowering friction coefficient. CoF of diamond tip on TiCN coating deposited on steel was found to be CoF ≈ 0,04 ÷ 0,05.

In general, an appropriate balance between good mechanical properties, high wear resistance and low friction coefficient is the best solution for application of TiCN as protective coatings on cutting tools or milling components. The advantage of reactive HiPIMS deposition of TiCN coatings is that, even though not bias nor heating were applied to the substrate, good mechanical and tribological performances were obtained, with hardness values that are little inferior to those obtained in literature by DCMS and RF bias (H≈35 GPa) [31], or with a multilayer graded structure (H≈44 GPa) [48]. The possibility to deposit a hard monolayer coating without the application of bias, make HiPIMS deposition technique well suited to produce TiCN coatings

on substrates that are not polarizable, such as plastics and polymers, which can have great interest in industrial applications.

Future development can concern the variation of deposition parameters in order to investigate how frequency, pulse duration and power supply can affect TiCN coating properties, if stable conditions are reached during HiPIMS plasma discharge. Moreover, additional substrate heating could be applied, that can favor adatom diffusion and rearrangements on the growing surface, thus ameliorating compactness and film morphology.

Different microstructure design can then be adopted, creating a multilayer or graded structure that can be particularly suited for the optimization of the film/substrate interactions, favoring high wear resistance after long sliding contact. Finally, also the hard nanocrystalline phase embedded in a soft matrix has been reported to be a promising configuration [49], thanks to a large volume of grain boundaries that restricts the initial crack size and favors the relaxation of internal stress introducing ductility and preventing fracture under severe loading conditions.

Appendix A

Rietveld method for structure refinement

One possible diffraction spectrum modeling that is really efficient when the crystal structure of the sample is known is supplied by Rietveld method [56]. It is based on the refinement of the whole diffraction profile through a least square fitting. The iteration process includes several variables describing instrumental characteristics, as well as structural, microstructural and geometrical parameters.

The refinement code minimizes the following function:

$$M = \sum_i w_i (I_i^{\exp} - I_i^{calc})^2 \,, \quad w_i = \frac{1}{I_i^{\exp}} \tag{i}$$

where the sum is extended to all the measured points of the spectrum. The calculated intensities I_i^{calc} are derived from an expression that includes the contribution from all the diffracting peaks and also from the background:

$$I_i^{calc} = S_F \sum_{j=1}^{Nphases} \frac{f_j}{V_j^2} \sum_{k=1}^{Npeaks} L_k |F_{k,j}|^2 S_j (2\theta_i - 2\theta_{k,j}) P_{k,j} A_j + bkg_i \tag{ii}$$

The first terms of equation (ii) represent the phase scale factor S_j, calculated considering the contribution of all the possible different phases present in the sample:

$$S_j = S_F \frac{f_j}{V_j^2} \tag{iii}$$

where S_F is the beam intensity (dependent on the measurement), f_j the phase volume fraction and V_j the phase cell volume.

The second part of equation (ii), identified by the summation over k, includes the contribution from all the diffraction peaks and is divided in several other internal components:

i. L_k is the Lorentz-Polarization factor. It is linked to the polarization of the incoming beam and it depends on the exit angle of the monochromator α through the relation:

$$L_p = \frac{1 + P_h \cos^2(2\theta)}{2(1 + P_h)\sin^2\theta\cos\theta} \,, \quad where \quad P_h = \cos^2(2\alpha) .$$

It is thus mainly affected by instrumental characteristics and by sample positioning.

ii. $|F_{k,j}|^2$ is the modulus of structure factor of phase j. It is dependent on the atomic scattering factor f_k and on the multiplicity of the k reflection, m_k through the relation:

$$|F_{k,j}|^2 = m_k \left| \sum_{n=1}^{N} f_n e^{-B_n \frac{\sin^2\theta}{\lambda^2}} (e^{2\pi i(hx_n + ky_n + lz_n)}) \right|^2 ,$$

where the sum is carried over the N atoms of coordinates (x_n, y_n, z_n).

$e^{-B\left(\frac{\sin\theta}{\lambda}\right)^2}$ is the thermal vibrational parameter linked to the Debye-Waller factor B, which may describe either isotropic or anisotropic vibration depending on the nature of the bonding between adjacent atoms.

For X-rays, atomic structure factor decreases with increasing the diffraction angle and is proportional to the number of electrons. A high thermal vibrational parameter accelerates this decrease.

iii. A_j is the absorption factor and represents a correction that must be introduced to compensate the volume absorption variations when rotating the sample by χ, or the incident beam angle by ω. It is obviously dependent on the linear absorption coefficient μ, and may be dependent on 2θ displacement when dealing with thin film samples.

iv. $S_j(2\theta_i\text{-}2\theta_{k,j})$ is the profile shape function of the kth peak of phase j at $2\theta_k$. It includes instrumental and sample broadening contributions trough the Cagliotti parameters and the width of the diffracting peaks. There could be several profile shape functions: the most commonly used is a mixture of a Gaussian and a Lorentzian shape, called Pseudo-Voigt profile. Its mathematical parameterization is:

$$PV(2\theta_i - 2\theta_k) = I_n \left[\eta_k \left(\frac{1}{1+S_{i,k}^2} \right) + (1-\eta_k)e^{-S_{i,k}^2 \ln 2} \right], \quad where\ S_{i,k} = \frac{2\theta_i - 2\theta_k}{\Delta_k}$$

Δ_k is the FWHM calculated trough the Cagliotti parameters (4.1) and η is a gaussianity parameter which varies between 0 and 1.

v. $P_{k,j}$ is a parameter that describes crystallites preferred orientations (texture). This correction is easily modeled for cylindrical texture symmetry, where it is assumed a regular distribution of a preferred crystallographic direction *<hkl>* around a specific texturation axis (for example the normal to the sample surface). March-Dollase formula best describe this behavior in a Bragg-Brentano geometry:

$$P_{k,j} = \frac{1}{m_k} \sum_{n=1}^{m_k} \left(G_1^2 \cos^2 \alpha_n + \frac{sen^2 \alpha_n}{G_1} \right)^{-\frac{3}{2}}$$

where the summation is carried over all the equivalent *hkl* reflections (multiplicity m_k), G_1 is the refinable March-Dollase parameter (G_1=1 for a random orientation), and α is the angle between the preferred orientation axis and the scattering vector.

For more complex systems, with several texture components and a non symmetric distribution, a quantitative texture analysis must be adopted. This approach will be described in detail in the next paragraph.

The final contribution to the calculated intensity I_i^{calc} (ii) comes from the background bkg_i of each ith measurement. It is represented as a polynomial function in 2θ of order M:

$$bkg(2\theta_i) = \sum_{m=0}^{M} a_m (2\theta_i)^m \qquad (iv)$$

where a_m are the polynomial coefficients.

As indicators of the quality of the refinements, some indices can be calculated through a minimization process. These reliability factors allow a statistical comparison between the calculated model and the measured profile. The most common factor is the R-weighted profile:

$$R_{wp} = \sqrt{\frac{\sum_{i=1}^{N}\left[w_i(I_i^{\exp} - I_i^{calc})\right]^2}{\sum_{i=1}^{N}\left[w_i I_i^{\exp}\right]^2}}, \qquad w_i = \frac{1}{\sqrt{I_i^{\exp}}} \qquad (v)$$

where the sum is carried over the number N of points. This reliability factor, through the definition of the weights w_i, includes the contribution of background as a possible source of error.

Quantitative texture analysis and WIMV method

When samples present a strong preferential orientation or an irregular crystallite distribution, the simple March-Dollase approach for texture refinement is no longer efficient. Rietveld algorithm must be implemented with new $P_{k,j}$ parameters that correctly reproduce the intensity changing of *{hkl}* diffracting planes with respect to the different tilting angles *(χ,ϕ)*.

These parameters are called Pole figures, and are generally extracted from the reconstruction of the Orientation Distribution Function (ODF, or *f(g)*) from the experimental spectra measured at different tilting angles.

ODF is a tridimensional representation of the statistical distribution of crystal orientation in a polycrystalline aggregate:

$$\frac{dV(g)}{V} = \frac{1}{8\pi^2} f(g)dg \qquad (vi)$$

where *dg= sinβ dβ dα dγ* is the element of volume in the orientation space defined trough the three Euler angles *{αβγ}*, *V* is the irradiated volume and *dV(g)* is the volume of crystallites with orientation between g and *g+dg*. The *{αβγ}* transformation enables to bring the crystal coordinate system into coincidence with the sample reference frame (Figure 4.17): *α* is called co-latitude (or pole distance) and is the equivalent of *χ* tilt angle from sample surface normal direction; *β* is the azimuth angle equivalent to ϕ rotation around sample surface normal direction, and *γ* is the third orthonormal axis.

f(g) is measured in multiple of a random distribution (m.r.d.) and it is normalized over the whole orientation space through the relation:

$$\int_{\beta=0}^{\beta=2\pi} \int_{\alpha=0}^{\alpha=\pi/2} \int_{\gamma=0}^{\gamma=\pi/2} f(g)dg = 8\pi^2 \,.$$

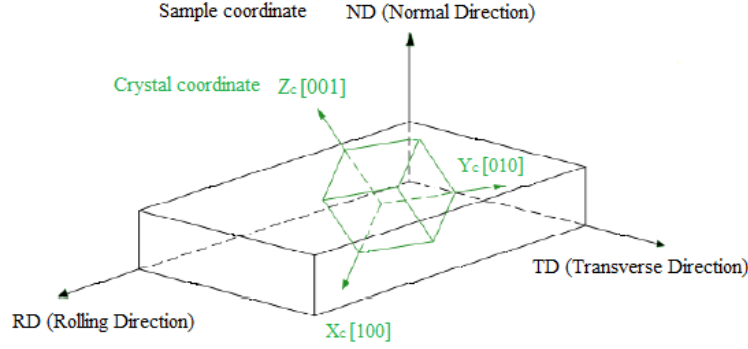*f(g)=1* for a sample without any preferred orientation.

Fig 1   Representation of a cubic crystal reference frame embedded in the sample coordinate system, defined respectively trough the crystalline directions [100], [010], [001],and the Rolling, Transverse and Normal directions (RD,TD,ND).

The experimentally measured quantity is not the tridimensional ODF, but a bidimensional distribution of the normals to the crystallographic planes that are diffracting in a given $\mathbf{y}=(\chi,\phi)$ sample configuration. Besides, the experimental diffracted intensities are strongly dependent on physical sample characteristics in a given direction (porosity, crystalline state..), so they must be rescaled to the so called normalized Pole Figure $P_{hkl}(\mathbf{y})$:

$$\frac{dV(\chi,\varphi)}{V} = \frac{1}{4\pi} P_{hkl}(\chi,\varphi) \,sen\chi\, d\chi\, d\varphi \qquad (vii)$$

where $P_{hkl}(\chi,\phi)$ are now the $P_{k,j}$ factors in the Rietveld formula (ii) with normalization condition:

$$\int_{\varphi=0}^{2\pi} \int_{\chi=0}^{\pi/2} P_{hkl}(\chi,\varphi)\,sen\chi\, d\chi\, d\varphi = 2\pi \qquad (viii)$$

and $P_{hkl}(\chi,\phi)=1$ m.r.d. for every random sample.

The relation between the Orientation Distribution Function $f(g)$ and the normalized Pole Figure is the fundamental equation of texture analysis:

$$P_{hkl}(\vec{y}) = \frac{1}{2\pi} \int_{<hkl>//y} f(g)\,d\xi \qquad (ix)$$

$d\xi$ is a generic projection path, that most commonly is identified with a stereographic projection.

Solving this equation enables to reconstruct the ODF and have a precise description of sample's preferential orientations.

Two different approaches have been developed to reconstruct $f(g)$: the first method was proposed by Bunge [79] and consists in an expansion of $f(g)$ and $P_{hkl}(\mathbf{y})$ in series of generalized spherical harmonics. The major problem of this approach is that, for strong textured samples, negative and unphysical density values could be generated (ghost phenomenon) and a "positivity correction method" must be implemented. Moreover, the harmonic distribution may in some cases differ from the real physical one, causing an imprecise simulation of the ODF.

The second analytical approach is the so called Williams-Imhof-Matthies-Vinel (WIMV) method: it starts with the discretization of $f(g)$ in a finite number of regular cell. For each cell, a precise value of the Orientation Distribution is calculated trough an iterative refinement process that ensures also the possibility of ghost correction:

$$f^{n+1}(g) = N_n \frac{f^n(g) f^0(g)}{\left(\prod_{<hkl>=1}^{I} \prod_{m=1}^{M_{hkl}} P_{hkl}^n(\vec{y}) \right)^{\frac{1}{IM_{hkl}}}} \qquad (x)$$

where N_n is a normalizing factor, $f^n(g)$ and $P^n{}_{hkl}(\mathbf{y})$ are the refined values of ODF and Pole Figure at n^{th} step and $f^0(g)$ is the orientation function as calculated from experimental pole measurements. The product extends over all total I measured Pole Figures, and over all the pole multiplicity M_{hkl}.

The best value of $f(g)$ is obtained maximizing the so called FON, that is the part of the ODF attributed to the randomly oriented crystal volume constituting its background, and texture sharpness.

When implemented in the Rietveld analysis, WIMV method requires also the extraction of Pole figures and their interpolation to the regular grid in which the ODF is divided.

If the sample presents a sharp texture or there is an irregular coverage of the orientation distributions, the utilization of the extended WIMV model, E-WIMV, has been proved to give the best and truthful results [80]: in this case the value of $f(g)$ in each cell is computed trough an entropy iteration algorithm that weighs each reflections taking into account the possibility of peak overlapping and relative intensity variations.

The goodness of $f(g)$ refinement can be estimated trough the minimization of the average reliability factors:

$$\overline{RP}_x = \frac{1}{I} \sum_{i=1}^{I} \sum_{j=1}^{J} \frac{\left| P_{hkl_i}^c(\vec{y}_j) - P_{hkl_i}^o(\vec{y}_j) \right|}{P_{hkl_i}^o(\vec{y}_j)} \qquad (xi)$$

where the sum is carried over the i=(1..I) measured pole figures and the j=(1..J) measured points $\mathbf{y_j}$. The subscripts c and o stand respectively to WIMV-calculated and observed normalized pole figures.

The analysis of diffraction spectra with E-WIMV method enables to extract also Inverse Pole Figures, which show how a selected direction in the sample reference frame is distributed in the reference frame of the crystal. For example, from the Inverse PF along sample normal direction (ND), is possible to understand wich lattice plane normal tends to be parallel to the sample surface normal. Their construction is based on a stereographic projection of diffracting crystal directions, and is depicted in (Fig 2).
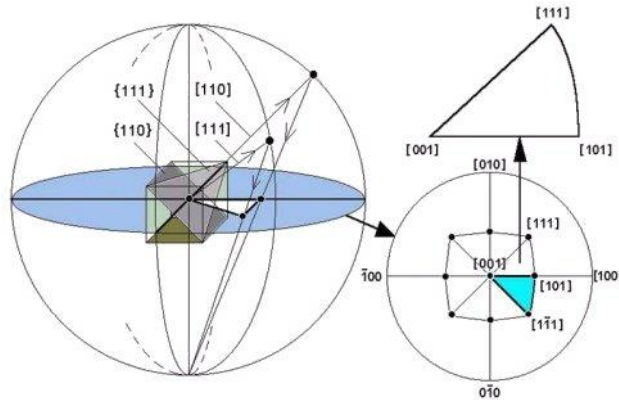

Fig 2 Schematic representation of the construction mechanism of Inverse Pole Figures.

Ringraziamenti

Ci terrei a riconoscere che, se sono giunta alla fine di questo lavoro di tesi e di questo periodo di studi, non è solo merito mio. Tante sono le persone da nominare e da ringraziare, per i tanti piccoli grandi gesti che mi hanno dato forza, coraggio, speranza, fiducia e che mi hanno permesso di giungere fino a questo importante traguardo.

Vorrei cominciare con il ringraziare chi mi ha dato la possibilità di mettermi in gioco per fare questo bel lavoro di tesi: grazie Marco e Alessandro, che mi avete seguito tanto in questi mesi aiutandomi ad elaborare i dati, leggendo e rileggendo la mia tesi, spiegandomi con pazienza ciò che non sapevo, e insegnandomi ad accettare che, quando si fa ricerca, non sempre va tutto secondo i piani e, ogni tanto, basta solo cambiare un po' prospettiva.. grazie a tutto il team di Veneto Nanotech, e in particolare a Marino, che mi ha pazientemente insegnato come usare tutta la strumentazione di laboratorio. Grazie a Roberto, sempre pronto a dispensare buoni consigli, e grazie a Irene, Andrea, Enrico, Veronica, Silvano, Anna, Marina, Martina, Enrico, Agnese ed Emanuele, per avermi accolto nel loro bel gruppo durante tutti questi mesi di lavoro in laboratorio.

Grazie anche a chi mi ha aiutato ad analizzare campioni nelle misure "fuori sede": grazie a Maria Vittoria, a Francesco a Nicola, che hanno speso un po' del loro tempo per me, affiancandomi nelle misure e nell'elaborazione dei dati.

E poi grazie e tutti i miei "compagni di viaggio e di avventure", senza i quali questi anni universitari sarebbero stati molto più pesanti e meno divertenti: grazie Laura, per la bella amicizia che si è formata in questi due anni e per il supporto reciproco in questo intenso periodo di scrittura, grazie Leonardo, per i tanti esami preparati insieme, e infine grazie Marco ed Elisa, per il vostro sostegno e la vostra presenza.

Ed ora arriviamo alla mia famiglia, a cui un solo grazie non è dire abbastanza, e per cui le parole non riuscirebbero ad esprimere loro tutta la mia gratitudine. Vi nomino soltanto, ma sappiate che senza di voi non sarei mai arrivata fino a qui: grazie mamma Anna Maria, papà Giovanni, Elena, Marco, Anna e Tommaso per tutto il vostro sostegno. Un grazie speciale alle mie nonne: Antonietta e Amelia, a cui ho dedicato questo lavoro di tesi: grazie per la vostra infinita fiducia in me e per avermi accompagnato con la preghiera in tutti questi anni.

E infine ultimo, ma non per questo meno importante: grazie Giovanni. Senza di te a sorreggermi, a sopportare tutte le mie ansie, le mie insicurezze e a donarmi tutto l'affetto di cui sei capace, non so come avrei fatto. Sei la persona più importante che ho al mio fianco.

Le parole non sono mai state il mio forte, ad ogni modo un grazie infinito anche a tutti quelli che non ho nominato, ma che saranno presenti in questo momento importante, a che mi sono stati accanto in tutti questi mesi. E come diceva una frase in "Into the wild":

"Happines is true only if shared – la felicità e autentica, solo se condivisa".

Grazie a tutti!

References

[1] Bull, S. ., Bhat, D. . & Staia, M. . Properties and performance of commercial TiCN coatings. Part 2: tribological performance. Surface and Coatings Technology 163-164, 507–514 (2003).

[2] Sarakinos, K., Alami, J. & Konstantinidis, S. High power pulsed magnetron sputtering: A review on scientific and engineering state of the art. Surface and Coatings Technology 204, 1661–1684 (2010).

[3] Chen, F., Introduction to plasma physics and controlled fusion, Plenum Press (1974).

[4] Chapman, B. , Glow discharge processes and plasma etching, John Wiley and Sons, (1980).

[5] Lundin, D. The HiPIMS Process. (2010). at http://www.diva-portal.org/smash/record.jsf?pid=diva2:321841

[6] Samuelsson, M. High power impulse magnetron sputtering under industrial conditions. (2011). at http://liu.diva-portal.org/smash/record.jsf?pid=diva2:410578

[7] Anders, A. Discharge physics of high power impulse magnetron sputtering. Surface and Coatings Technology 205, S1–S9 (2011).

[8] Arnell, R. . & Kelly, P. . Recent advances in magnetron sputtering. Surface and Coatings Technology 112, 170–176 (1999).

[9] Aijaz, A. HiPIMS-based Novel Deposition Processes for Thin Films. (2012). at http://liu.diva-portal.org/smash/record.jsf?pid=diva2:535282

[10] Kouznetsov, V. & Macák, K. A novel pulsed magnetron sputter technique utilizing very high target power densities. Surf. Coat. Technol. 122, 290–293 (1999).

[11] Konstantinidis, S., Dauchot, J. P., Ganciu, M., Ricard, A. & Hecq, M. Influence of pulse duration on the plasma characteristics in high-power pulsed magnetron discharges. Journal of Applied Physics 99, 013307 (2006).

[12] Thornton, J. A. MAGNETRON SPUTTERING: BASIC PHYSICS AND APPLICATION TO CYLINDRICAL MAGNETRONS. J Vac Sci Technol 15, 171–177 (1978).

[13] Rossnagel, S. M. & Kaufman, H. R. Charge transport in magnetrons. J. Vac. Sci. Technol. 5, 2276–2279

[14] Hala, M., Viau, N., Zabeida, O., Klemberg-Sapieha, J. E. & Martinu, L. Dynamics of reactive high-power impulse magnetron sputtering discharge studied by time- and space-resolved optical emission spectroscopy and fast imaging. Journal of Applied Physics 107, 043305 (2010).

[15] Christie, D. J. Target material pathways model for high power pulsed magnetron sputtering. Journal of Vacuum Science & Technology A: Vacuum, Surfaces, and Films 23, 330 (2005).

[16] Vlček, J., Kudláček, P., Burcalová, K. & Musil, J. High-power pulsed sputtering using a magnetron with enhanced plasma confinement. Journal of Vacuum Science & Technology A: Vacuum, Surfaces, and Films 25, 42 (2007).

[17] Berg, S. & Nyberg, T. Fundamental understanding and modeling of reactive sputtering processes. Thin Solid Films 476, 215–230 (2005).

[18] Berg, S. Blom, H-O., Larsson, T., & Nender, C., Modeling of reactive sputtering of compound materials, J. Vac. Sci. Technol. A 5(2), 202-207 (1986).

[19] Berg, S., Blom, O-H., Moradi, M. & Nender, C., Process modeling of reactive sputtering, J, Vac. Sci. Technol. A 7(3), 1225-1229 (1989).

[20] Sproul, W. D., Christie, D. J. & Carter, D. C. Control of reactive sputtering processes. Thin Solid Films 491, 1–17 (2005).

[21] Kubart, T., Kappertz, O., Nyberg, T. & Berg, S. Dynamic behaviour of the reactive sputtering process. Thin Solid Films 515, 421–424 (2006).

[22] Barankova, H., Berg, S., Carlsson, P. & Nender, C. Hysteresis effects in the sputtering process using two reactive gases. Thin Solid Films 260, 181–186 (1995).

[23] Audronis, M. & Bellido-Gonzalez, V. Hysteresis behaviour of reactive high power impulse magnetron sputtering. Thin Solid Films 518, 1962–1965 (2010).

[24]   Audronis, M. et al. Diffusive racetrack oxidation in a Ti sputter target by reactive high power impulse magnetron sputtering. Journal of Physics D: Applied Physics 45, 375203 (2012).

[25]   Audronis, M., Bellido-Gonzalez, V. & Daniel, B. Control of reactive high power impulse magnetron sputtering processes. Surface and Coatings Technology 204, 2159–2164 (2010).

[26]   Barna, P. . & Adamik, M. Fundamental structure forming phenomena of polycrystalline films and the structure zone models. Thin Solid Films 317, 27–33 (1998).

[27]   Anders, A. Discharge physics of high power impulse magnetron sputtering. Surface and Coatings Technology 205, S1–S9 (2011).

[28]   Bull, S. ., Bhat, D. . & Staia, M. . Properties and performance of commercial TiCN coatings. Part 1: coating architecture and hardness modelling. Surface and Coatings Technology 163-164, 499–506 (2003).

[29]   Fang, T.-H., Jian, S.-R. & Chuu, D.-S. Nanomechanical properties of TiC, TiN and TiCN thin films using scanning probe microscopy and nanoindentation. Applied Surface Science 228, 365–372 (2004).

[30]   Lackner JM, Waldhauser W, Ebner R, "Large-area high rate pulsed laser deposition of smooth TiC_xN_{1-x} coatings at room temperature- mechanical and tribological properties", Surf Coat Technol 2004; 188, 519-24

[31]   Restello, S., Boscarino, D. & Rigato, V. A study of Ti–C–N(H) and Ti:CNx(H) coatings grown with a magnetron sputtering/PECVD hybrid deposition process. Surface and Coatings Technology 200, 6230–6234 (2006).

[32] Arrando F, Polo MC, Molera P, Esteve J. Comparative study of high corrosion resistant TiC_xN_{1-x} and TiN hard coatings. Surf Coat Technol 1994; 68/68; 536-40.

[33]   Rie KT, Gebauer A, Wohle J. Plasma assisted CVD for low temperature coatings to improve the wear and corrosion resistance. Surf Coat Technol 1996; 86/87; 498-506.

[34]   Su, Y. . & Kao, W. . Optimum multilayer TiN–TiCN coatings for wear resistance and actual application. Wear 223, 119–130 (1998).

[35]   Zheng, J., Hao, J., Liu, X. & Liu, W. Properties of TiN/TiCN multilayer films by direct current magnetron sputtering. Journal of Physics D: Applied Physics 45, 095303 (2012).

[36] Yang, J. H., Chen, K. H., Wang, S. Q., Xiao, D. H. & Zhu, C. J. Characteristics and performance of Ti(C, N) coatings synthesized by magnetron sputtering technique. Journal of Alloys and Compounds 471, 162–165 (2009).

[37] Chen, R., Tu, J. P., Liu, D. G., Mai, Y. J. & Gu, C. D. Microstructure, mechanical and tribological properties of TiCN nanocomposite films deposited by DC magnetron sputtering. Surface and Coatings Technology 205, 5228–5234 (2011).

[38]   Samuelsson, M. et al. Growth of Ti-C nanocomposite films by reactive high power impulse magnetron sputtering under industrial conditions. Surface and Coatings Technology 206, 2396–2402 (2012).

[39] Zehnder, T. Nanocomposite TiC r a □ C : H hard coatings deposited by reactive PVD. Surface and Coatings Technology , 138–144 (2000).

[40] Gulbiński, W. et al. Evaluation of phase, composition, microstructure and properties in TiC/a-C:H thin films deposited by magnetron sputtering. Applied Surface Science 239, 302–310 (2005).

[41]   Jansson, U. & Lewin, E. Sputter deposition of transition-metal carbide films — A critical review from a chemical perspective. Thin Solid Films 536, 1–24 (2013).

[42]   Lewin, E. et al. Design of the lattice parameter of embedded nanoparticles. Chemical Physics Letters 496, 95–99 (2010).

[43]   Levi, G., Kaplan, W. & Bamberger, M. Structure refinement of titanium carbonitride (TiCN). Materials Letters 344–350 (1998). at <http://www.sciencedirect.com/science/article/pii/S0167577X97002760>

[44]   Schneider, J. & Voevodin, A. X-ray diffraction investigations of magnetron sputtered TiCN coatings. Surface and Coatings … 75, 312–319 (1995).

[45] Li, J., Zhang, S. & Li, M. Influence of the C2H2 flow rate on gradient TiCN films deposited by multi-arc ion plating. Applied Surface Science 283, 134–144 (2013).

[46] Senna, L. F., Achete, C. a., Hirsch, T. & Freire, F. L. Structural, chemical, mechanical and corrosion resistance characterization of TiCN coatings prepared by magnetron sputtering. Surface and Coatings Technology 94-95, 390–397 (1997).

124

[47] Zheng, J., Hao, J., Liu, X., Gong, Q. & Liu, W. A thick TiN/TiCN multilayer film by DC magnetron sputtering. Surface and Coatings Technology 209, 110–116 (2012).

[48] Zhang, G., Li, B., Jiang, B., Chen, D. & Yan, F. Microstructure and Mechanical Properties of Multilayer Ti(C, N) Films by Closed-field Unbalanced Magnetron Sputtering Ion Plating. Journal of Materials Science & Technology 26, 119–124 (2010).

[49] Martínez-Martínez, D., López-Cartes, C., Justo, a., Fernández, a. & Sánchez-López, J. C. Self-lubricating Ti–C–N nanocomposite coatings prepared by double magnetron sputtering. Solid State Sciences 11, 660–670 (2009).

[50] Freire, F. L., Senna, L. F., Achete, C. a. & Hirsch, T. Characterization of TiCN coatings deposited by magnetron sputter-ion plating process: RBS and GDOS complementary analyses. Nuclear Instruments and Methods in Physics Research Section B: Beam Interactions with Materials and Atoms 136-138, 788–792 (1998).

[51] Balázsi, K. et al. Structural, mechanical and biological comparison of TiC and TiCN nanocomposites films. Journal of the European Ceramic Society 33, 2217–2221 (2013).

[52] P. Willich and R. Bethke, "Quantitative depth profiling of Ti-N-C-O coatings materials using MCs+-SIMS", Proceedings, Secondary Ion Mass Spectrometry SIMS XI, John Wiley and Sons,991-994 (1997)

[53] Willich, P. & Steinberg, C. SIMS depth profile analysis of wear resistant coatings on cutting tools and technical components. Applied Surface Science 179, 3–8 (2001).

[54] Wu, F. et al. Elaboration and quantitative investigation of BCN-type films by dynamic SIMS using the MCsx+ mode. Surface and Interface Analysis 43, 669–672 (2011).

[55] A.A.Salem, G. Stingeder, M.Grasserbauer, " SIMS and RBS analysis of leached glass: reliability of RSF method for SIMS quantification", Journal of Material Sciences 7, 373-379 (1996).

[56] D. Chateigner, "Combined Analysis : structure-texture-microstructure-phase-stresses-reflectivity determination by x-ray and neutron scattering.", IUT Mesures Physiques, Université de Caen Basse-Normandie, Caen, France. http://www.ecole.ensicaen.fr/~chateign/texture/combined.pdf

[57] Robertson, J. Diamond-like amorphous carbon. Materials Science and Engineering: R: Reports 37, 129–281 (2002).

[58] Martínez-Martínez, D., López-Cartes, C., Fernández, a. & Sánchez-López, J. C. Influence of the microstructure on the mechanical and tribological behavior of TiC/a-C nanocomposite coatings. Thin Solid Films 517, 1662–1671 (2009).

[59] Ferrari, a. & Robertson, J. Interpretation of Raman spectra of disordered and amorphous carbon. Physical Review B 61, 14095–14107 (2000).

[60] Ferrari, a., Rodil, S. & Robertson, J. Interpretation of infrared and Raman spectra of amorphous carbon nitrides. Physical Review B 67, 155306 (2003).

[61] Carvalho, I. et al. Influence of surface features on the adhesion of Staphyloccocus epidermidis to Ag–TiCN thin films. Science and Technology of Advanced Materials 14, 035009 (2013).

[62] Manninen, N. K. et al. Ag–Ti(C, N)-based coatings for biomedical applications: influence of silver content on the structural properties. Journal of Physics D: Applied Physics 44, 375501 (2011).

[63] Zhang, S., Sun, D., Fu, Y. & Du, H. Recent advances of superhard nanocomposite coatings: a review. Surface and Coatings Technology 167, 113–119 (2003).

[64] J.Rösler, H.Harders, M.Bäker, "Mechanical behavior of engineering matherials. Metals, ceramics, polymers and composites", ed. Springer (2007)

[65] Musil, J. & Vlcek, J. Magnetron sputtering of hard nanocomposite coatings and their properties. 557–566 (2001).

[66] Musil, J. & Jirout, M. Toughness of hard nanostructured ceramic thin films. Surface and Coatings Technology 201, 5148–5152 (2007).

[67] Zok, F. W. & Miserez, a. Property maps for abrasion resistance of materials. Acta materialia 55, 6365–6371 (2007).

[68] Bull, S.J., Failure mode maps in the thin film scratch adhesion test, Tribology International 30, 491-498 (1997).

[69] Bull, S. J. & Berasetegui, E. G. An overview of the potential of quantitative coating adhesion measurement by scratch testing. Tribology International 39, 99–114 (2006).

[70] Pei, Y., Galvan, D. & Dehosson, J. Nanostructure and properties of TiC/a-C:H composite coatings. Acta Materialia 53, 4505–4521 (2005).

[71] Jamroz, P. & Zyrnicki, W. Optical emission spectroscopy study for nitrogen–acetylene–argon and nitrogen–acetylene–helium 100 kHz and dc discharges. Vacuum 84, 940–946 (2010).

[72] Qayyum, a. et al. Optical emission spectroscopy of Ar–N2 mixture plasma. Journal of Quantitative Spectroscopy and Radiative Transfer 107, 361–371 (2007).

[73] Y.Stark, R.Fromter, D.Stickler, H.P.Oepen, "Sputter yields of single- and polycrystalline metals for application in focused ion beam technology", Journal of Applied Physics 105,013542 (2009).

[74] P.Sigmund, "Theory of sputtering. I. Sputtering yield of amorphous and polycrystalline targets", Physical Review 184, 383-416 (1969).

[75] Ferrari, a. C., Rodil, S. E. & Robertson, J. Resonant Raman spectra of amorphous carbon nitrides: the G peak dispersion. Diamond and Related Materials 12, 905–910 (2003).

[76] S.Matthies, G.W.V inel, K. Helming, Standard Distribution in Texture Analysis, Akademie-Verlag, Berlin FRG, (1987)

[77] Handbook of Nanoindentation. (2010). doi:10.1201/b12116

[78] Galvan, D., Pei, Y. T. & De Hosson, J. T. M. Influence of deposition parameters on the structure and mechanical properties of nanocomposite coatings. Surface and Coatings Technology 201, 590–598 (2006).

[79] H.J. Bunge, "Texture Analysis in Materials Science", P.R. Morris Trans., Butterworths, London (1982)

[80] Lutterotti, L., Chateigner, D., Ferrari, S. & Ricote, J. Texture, "residual stress and structural analysis of thin films using a combined X-ray analysis". Thin Solid Films 450, 34–41 (2004).